Astronomy Letters, Vol. 30, No. 10, 2004, pp. 657–662. Translated from Pis'ma v Astronomicheskiĭ Zhurnal, Vol. 30, No. 10, 2004, pp. 723–728.

CMB Recombination Lines of Hydrogen: The Differential Spectrum

V. K. Dubrovich[1,2] and S. I. Grachev[3*]

[1] *Special Astrophysical Observatory, St. Petersburg Branch, Russian Academy of Sciences, St. Petersburg, 196140 Russia*

[2] *Pulkovo Astronomical Observatory, Russian Academy of Sciences, Pulkovskoe shosse 65, St. Petersburg, 196140 Russia*

[3] *Sobolev Astronomical Institute, St. Petersburg State University, Universitetskiĭ pr. 28, St. Petersburg, 198504 Russia*

Received December 23, 2003

Abstract—We have calculated the distortions of the cosmic microwave background (CMB) spectrum in the wavelength range 2–50 cm due to the superposition of the CMB hydrogen recombination radiation in subordinate lines. The level populations were determined by numerically solving the equation of recombination kinetics together with the statistical equilibrium equations for a 60-level model hydrogen atom. The relative distortions are $\approx 10^{-7}$–10^{-6}, with their wavelength dependence having a low-contrast, wavy pattern. However, the contrast increases severalfold and becomes pronounced when passing to the differential distortion spectrum. We study the dependence of the distortions on cosmological parameters.

Key words: *cosmology, cosmic microwave background, early Universe.*

INTRODUCTION

The detection of hydrogen recombination radiation, in particular, radiation in subordinate lines, would be direct evidence for the validity of the model of a hot Universe. This radiation arises at the hydrogen recombination epoch, in the redshift range from $z \approx 800$ to $z \approx 1600$, and must currently be observed at wavelengths $\lambda > 0.05$ cm. These distortions were first estimated by Dubrovich (1975); subsequently, more detailed calculations were performed by Bernshteĭn *et al.* (1977), Beĭgman and Sunyaev (1978), Dubrovich and Stolyarov (1995), and Burgin (2003). Two basic approaches to the problem have been developed:

(1) A simplified approach where the transfer in Lyman lines (and, accordingly, the recombination dynamics) and the release of subordinate photons are calculated separately; and

(2) A full approach where the complete system of nonstationary kinetic equations is written whose exact solution formally yields the recombination dynamics as well as the intensities and profiles of the subordinate lines. The first approach, which was used in the papers mentioned above, quickly yielded plausible results with the then available computational base. In addition, being clear and physical, it allowed one to control the results obtained and to predict new results (Dubrovich and Shakhvorostova 2004). At the same time, dissatisfaction with the substantiation of the approximations used forced us to develop and bring to a result the second approach (Grachev and Dubrovich 1991). Formally, the computational accuracy in this case is higher than that achieved in the first case due to a more accurate allowance for all of the transitions in the transfer of Lyman photons. In fact, even in our previous paper, we obtained all of the necessary equations for calculating the intensities of the subordinate lines. However, in view of the various circumstances, only the first part of the program was implemented: we obtained results on the recombination dynamics, i.e., on the dynamics of the degree of ionization in the standard model. In this paper, we present results of the second part of our calculation. Note, however, that here we have not yet included the effects of momentum level splitting (Dubrovich and Shakhvorostova 2004) and two-photon transitions from high levels (Dubrovich 1987) in the transition matrix.

Here, we performed more detailed calculations by taking into account more detailed recombination dynamics and using the current parameters that describe this dynamics. We used a program that we wrote previously (Grachev and Dubrovich 1991). It simultaneously calculates the time (redshift z) variations in the degree of hydrogen ionization and in the populations of excited neutral hydrogen states

*E-mail: stas@astro.spbu.ru

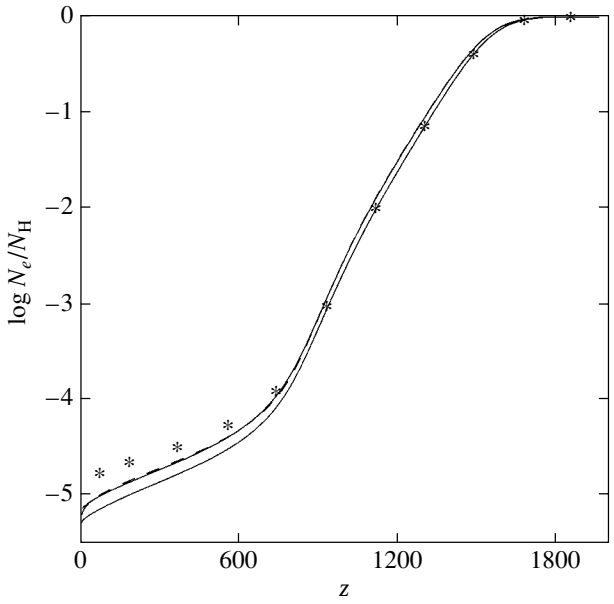

Fig. 1. Profiles of the degree of ionization (N_e/N_H) for $\Omega_{total} = 1$, $T_0 = 2.7$, $H_0 = 97.5$, $\Omega_H = 1$ (lower curve), $\Omega_H = 0.76$ (upper curve); the dashed line represents the computations with the recfast.for code by Seager *et al.* (1999) ($\Omega_H = 0.76$); the asterisks represent the results of Peebles (1968) ($\Omega_H = 1$).

for a 60-level model atom; for the second level, we took into account the splitting into the $2s$ and $2p$ sublevels. Subsequently, we calculated the source functions using the known populations and determined the subordinate line intensities from the formal (with a given source function) solution of the radiative transfer equation. The superposition of these intensities is responsible for the distortions of the cosmic microwave background (CMB) spectrum in the wavelength range 2–50 cm.

Many calculations of the recombination dynamics have been performed to date (see the review by Seager *et al.* (2000) and Grachev and Dubrovich (1991)). In fact, two methods are used in this case: the method of an effective three-level atom and the method of simultaneously solving the equations for the electron density and the level populations. The former method was first proposed by Peebles (1968) and Zel'dovich *et al.* (1968) and subsequently improved by several authors. One of its latest modifications was performed by Seager *et al.* (1999) (the recfast.for code). The latter method is more accurate and allows the hydrogen line profiles to be constructed, but it requires much more computer resources. It was probably first implemented by Grachev and Dubrovich (1991) for a 60-level model hydrogen atom and subsequently (under almost the same assumptions) by Seager *et al.* (1999, 2000) for a 300-level model atom. As might be expected, different methods yield similar results at $z > 800$. The main discrepancies arise at $z < 800$. As an example, Fig 1 compares the results of our calculations (solid lines) with those of Peebles (1968) (asterisks) and with the results of the calculations using the recfast.for code by Seager *et al.* (1999) (dashed line). We see that at $z < 800$, the recombination according to Peebles is slower, because, as was first noted by Grachev and Dubrovich (1991) and subsequently by Seager *et al.* (1999), the total recombination coefficient was underestimated. However, the agreement improves at $z > 800$ (but deteriorates at $z < 800$) when it is considered that the mass fraction in Peebles's paper is $X = 1$, while actually $X \approx 0.76$. The most detailed calculations performed by Seager *et al.* (2000) showed that up to three hundred hydrogen atomic levels should be taken into account, although even the 50-level model atom yields very similar results. Thus, our 60-level model atom must yield results close to exact ones, particularly at $z > 800$, where the hydrogen subordinate lines of interest arise.

BASIC EQUATIONS AND RELATIONS

The nonstationary equation of radiative transfer in a uniform expanding Universe is

$$\frac{1}{c}\frac{\partial I(\nu,t)}{\partial t} - \frac{\nu}{c}H(t)\frac{\partial I(\nu,t)}{\partial \nu} + \frac{3}{c}H(t)I(\nu,t) = -k(\nu,t)[I(\nu,t) - S(\nu,t)],$$

where $I(\nu,t)$ is the radiation intensity; $S(\nu,t) = \varepsilon(\nu,t)/k(\nu,t)$ is the source function; $k(\nu,t)$ and $\varepsilon(\nu,t)$ are the absorption and emission coefficients, respectively; and $H(t)$ is the Hubble factor. To pass from the time scale to the redshift scale, we use the relation

$$\frac{dz}{dt} = -(1+z)H(z).$$

As a result, we obtain the equation

$$H(z)\left[(1+z)\frac{\partial I(\nu,z)}{\partial z} + \nu\frac{\partial I(\nu,z)}{\partial \nu} - 3I(\nu,z)\right] = ck(\nu,z)[I(\nu,z) - S(\nu,z)].$$

It can be easily verified that the solution of this equation at thermodynamic equilibrium is

$$I(\nu,z) = S(\nu,z) = B(\nu,T(z)) = (2h\nu^3/c^2)\left[e^{h\nu/kT_0(1+z)} - 1\right]^{-1}.$$

It is appropriate to pass to dimensionless quantities—the mean occupation numbers

$$s(\nu,z) \equiv (c^2/2h\nu^3)S(\nu,z),$$
$$i(\nu,z) \equiv (c^2/2h\nu^3)I(\nu,z).$$

The basic transfer equation can then be rewritten as

$$H(z)\left[(1+z)\frac{\partial i(\nu,z)}{\partial z}+\nu\frac{\partial i(\nu,z)}{\partial \nu}\right] = ck(\nu,z)[i(\nu,z)-s(\nu,z)].$$

The formal solution of this equation, i.e., the solution for a given source function $s(\nu,z)$ on the right-hand side, is

$$i(\nu,z)=F(\nu/(1+z)) \times \exp\left(-\int_z^{z_0} f(\nu',z')\frac{dz'}{1+z'}\right) + \int_z^{z_0} f(\nu',z')s(\nu',z') \times \exp\left(-\int_z^{z'} f(\nu'',z'')\frac{dz''}{1+z''}\right) dz'/(1+z'), \quad (1)$$

where $f(\nu,z)\equiv ck(\nu,z)/H(z)$,

$$\nu'=\nu(1+z')/(1+z), \quad (2)$$

$$\nu''=\nu(1+z'')/(1+z).$$

Here, the function $F(\nu/(1+z))$ can be determined from the condition that at the initial time (at $z=z_0$) the radiation is Planckian. Thus,

$$F(\nu/(1+z))=b(\nu,T(z))\equiv\left[e^{h\nu/kT(z)}-1\right]^{-1},$$
$$T(z)=T_0(1+z).$$

Let us consider the transfer in a line ($i\rightleftarrows k$ transition). In this case,

$$k(\nu,z)=\frac{h\nu}{4\pi}n_iB_{ik}\varphi(\nu)\left[1-\frac{n_kg_i\psi(\nu)}{n_ig_k\varphi(\nu)}\right], \quad (3)$$

$$s(\nu,z)=\left[\frac{g_kn_i\varphi(\nu)}{g_in_k\psi(\nu)}-1\right]^{-1},$$

where $\varphi(\nu)$ and $\psi(\nu)$ are the profiles of the absorption and emission coefficients, respectively, normalized as follows:

$$\int_0^\infty\varphi(\nu)d\nu=\int_0^\infty\psi(\nu)d\nu=1.$$

Using formula (3), we can write function $f(\nu,z)$ in the formal solution (1) as

$$f(\nu,z)=ck(\nu,z)/H(z)\equiv\nu\varphi(\nu)/\gamma(\nu,z),$$

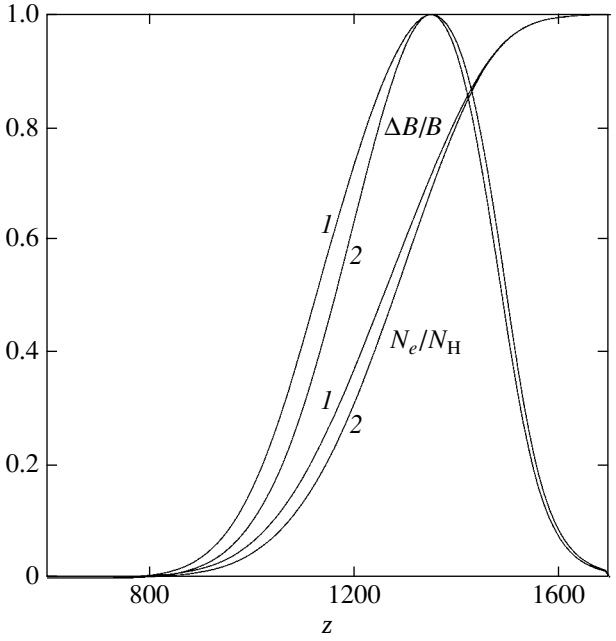

Fig. 2. Profiles of the degree of ionization ($N_e/N_{\rm H}$) and the recombination line ($\Delta B/B$) for $H_0=75$, $\Omega_{\rm B}=0.044$, $\Omega_{\rm total}=1$ and various Ω_Λ: (*1*) $\Omega_\Lambda=0$; (*2*) $\Omega_\Lambda=0.7$, which correspond to $\Omega_{\rm matter}=1$ and $\Omega_{\rm matter}=0.3$, where $\Omega_{\rm matter}=\Omega_{\rm total}-\Omega_\Lambda$.

where the dimensionless gradient in expansion velocity is

$$\gamma(\nu,z)=\frac{4\pi}{hc}\frac{H(z)}{n_iB_{ik}}\left[1-\frac{n_kg_i\psi(\nu)}{n_ig_k\varphi(\nu)}\right]^{-1}.$$

If the level populations and the profiles of the absorption and emission coefficients are known, then the line intensity can be calculated by numerical integration using formula (1) by taking into account the above expressions for the absorption coefficient and the source function. However, under certain simplifying assumptions, the integration can be performed analytically. First, we may assume that the scattering in subordinate lines is accompanied by a complete frequency redistribution, i.e., the profiles of the absorption and emission coefficients coincide: $\varphi(\nu)=\psi(\nu)$. The dimensionless source function and velocity gradient then do not depend on the frequency:

$$s(\nu,z)=s(z)=\left(\frac{g_kn_i}{g_in_k}-1\right)^{-1},$$
$$\gamma(\nu,z)=\gamma(z)=\frac{4\pi}{hc}\frac{H(z)}{n_iB_{ik}}\left(1-\frac{n_kg_i}{n_ig_k}\right)^{-1}\equiv 1/\tau_{ik}(z).$$

Second, we can use the so-called narrow-line approximation, where the profile of the absorption coefficient is substituted with a delta-function, $\varphi(\nu)=$

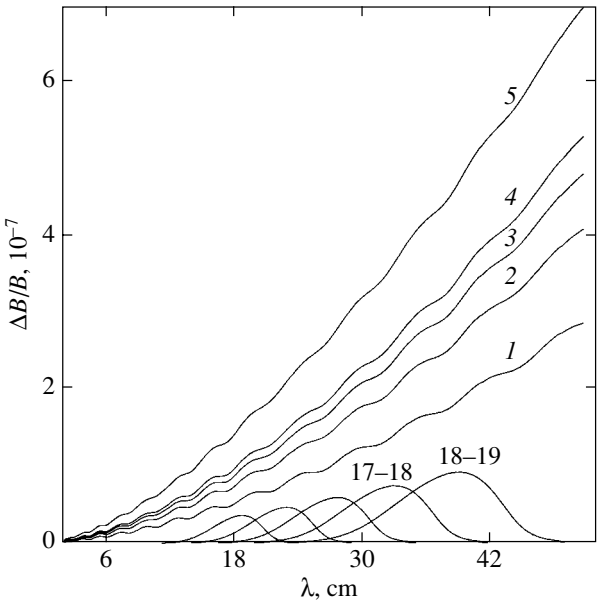

Fig. 3. Relative distortions of the microwave background spectrum caused by individual lines and by the superposition of various lines at $H_0 = 75$, $\Omega_H = 0.04$, and $\Omega_\Lambda = 0$. The (17–18, 18–19) transition level numbers are indicated; (*1*) $\Delta n = 1$; (*2*) $\Delta n = 1, 2$; (*3*) $\Delta n = 1, 2, 3$; (*4*) $\Delta n = 1, 2, 3, 4$; and (*5*) $\Delta n = 1, 2, \ldots, 58$.

$\delta(\nu - \nu_{ik})$, where ν_{ik} is the frequency of the line center. In this case,

$$f(\nu', z') = \nu'\delta(\nu' - \nu_{ik})\tau_{ik}(z'), \qquad (4)$$

and, therefore, we can factor the source function $s(\nu', z')$ outside the integral sign in formula (1) at point $\nu' = \nu_{ik}$, $z' = z_l \equiv (\nu_{ik}/\nu)(1+z) - 1$. The remaining integral is taken exactly, so

$$i(\nu, z) = b(\nu, T(z)) \times \exp\left(-\int_z^{z_0} f(\nu', z')\frac{dz'}{1+z'}\right) + s(z_l)\left[1 - \exp\left(-\int_z^{z_0} f(\nu', z')\frac{dz'}{1+z'}\right)\right].$$

Next, according to (2), we can pass in the exponents under the integral to integration over ν', with $\nu' dz'/(1+z') = d\nu'$. As a result, using formula (4), we obtain

$$i(\nu, z) = b(\nu, T(z))e^{-\tau_{ik}(z_l)} + s(z_l)\left[1 - e^{-\tau_{ik}(z_l)}\right],$$
$$z_l = \frac{\nu_{ik}}{\nu}(1+z) - 1, \quad \frac{1+z}{1+z_0}\nu_{ik} \le \nu \le \nu_{ik}.$$

This formula is actually the solution of the problem of line formation in an expanding medium in the approximation of Sobolev (1947) (see also the paper by Grachev (1994) devoted to the review of generalizations of Sobolev's approximation). For the relative distortion of the microwave background intensity $\Delta B/B \equiv [i(\nu, 0) - b(\nu, T_0)]/b(\nu, T_0)$ at the current epoch ($z = 0$), we obtain for an individual line

$$\Delta B/B = [s(z_l)/b(\nu, T_0) - 1]\left[1 - e^{-\tau_{ik}(z_l)}\right],$$
$$z_l = \nu_{ik}/\nu - 1, \quad \nu_{ik}/(1+z_0) \le \nu \le \nu_{ik}.$$

The total contribution can be determined by the summation over all lines. Since the recombination radiation in subordinate hydrogen lines of interest to us falls within the Rayleigh–Jeans region of the current microwave background spectrum, we may assume that $\Delta B/B = \Delta T/T$.

RESULTS

We calculated the hydrogen atomic level populations as a function of the redshift z (together with the electron density) using our program written previously (Grachev and Dubrovich 1991). The parameters in the problem are the equilibrium microwave background temperature T_0, the Hubble factor H_0, the ratio of the total density to the critical density $\Omega_{\rm total}$, the ratio of the baryon density to the critical density Ω_B, the ratio of the density due to the Λ term to the critical density Ω_Λ, and the hydrogen mass fraction X at the current epoch. We used the following redshift dependences of the equilibrium background radiation temperature T, the number density of the hydrogen atoms and ions N_H, and the Hubble factor H:

$$T = T_0(1+z), \quad N_H = N_0(1+z)^3,$$
$$H = H_0(1+z) \times \sqrt{1 + \Omega_{\rm total}z - \Omega_\Lambda[1 + z - (1+z)^{-2}]},$$

where

$$N_0 = 1.124 \times 10^{-5}\Omega_H h_0^2 \ {\rm cm}^{-3},$$
$$h_0 = H_0/100 \ {\rm km/(s\ Mpc)}, \quad \Omega_H = X\Omega_B;$$

for the Hubble factor H, we used a formula from the paper by Sahni and Starobinsky (1999, page 16, formula (19)).

The calculations were performed for $T_0 = 2.73$ K, $\Omega_{\rm total} = 1$, and $X = 0.76$. The parameters H_0, Ω_H, and Ω_Λ were varied. Figure 2 shows $N_e(z)/N_H(z)$ and the large-scale $\Delta B/B$ profile of the recombination line normalized to unity at maximum. We see that the parameter Ω_Λ weakly affects both the recombination dynamics and the large-scale line profile.

Figure 3 shows the profiles of individual lines and the results of the successive summation of the contributions from the lines arising during transitions between different levels.

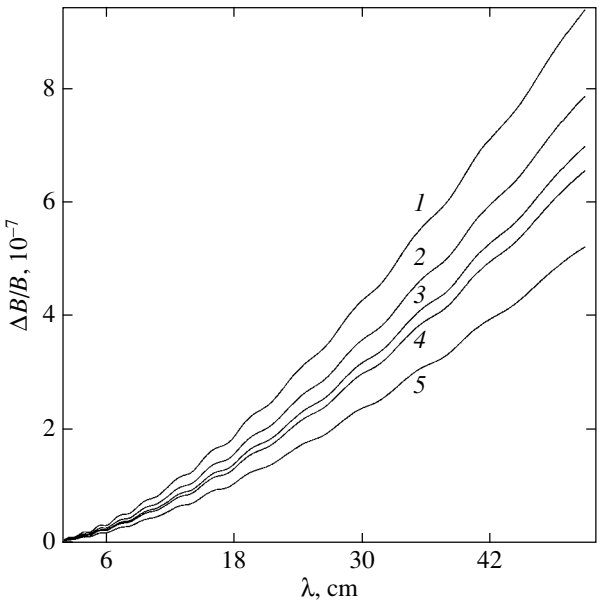

Fig. 4. Spectral distortion for $\Omega_\Lambda = 0$ and various H_0 and Ω_H: (*1*) $H_0 = 55$; $\Omega_H = 0.1$; (*2*) $H_0 = 65$; $\Omega_H = 0.06$; (*3*) $H_0 = 75$; $\Omega_H = 0.04$; (*4*) $H_0 = 65$; $\Omega_H = 0.05$; (*5*) $H_0 = 75$; $\Omega_H = 0.03$.

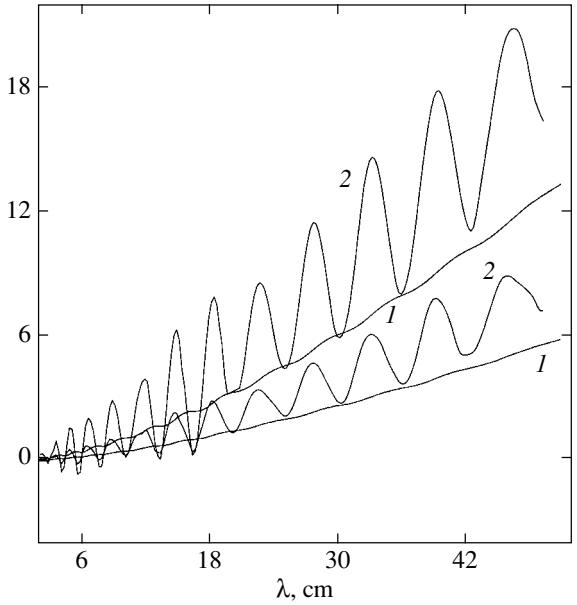

Fig. 5. Differential (*2*) and original (*1*) distortion spectra: (*1*) $10^7 \Delta B/B$; (*2*) $10^7 \lambda d(\Delta B/B)/d\lambda$ for $H_0 = 75$, $\Omega_\Lambda = 0.7$, $\Omega_B = 0.044$ (the two lower curves), $\Omega_B = 0.1$ (the two upper curves).

Figure 4 illustrates the dependence of the spectral distortions on the parameters H_0 and Ω_H for $\Omega_\Lambda = 0$ (here, the contributions from all of the lines under consideration are added). The dependence on Ω_H is most pronounced. Finally, Fig. 5 shows the differential distortion spectrum $\lambda d(\Delta B/B)/d\lambda$ and the original $\Delta B/B$ spectrum. Note the significant enhancement of the contrast in the differential spectrum compared to the original spectrum.

As we see from the above results, the rate of change in the degree of ionization is highly nonuniform. As would be expected, this is attributable to the transition from quasi-equilibrium dynamics at large z to a stage at which the effect of Lyman photon reabsorption is significant. The first part yields a fairly rapid increase in the number of neutral atoms, and at the second stage this increase slows down. However, in absolute intensities, these phases are interchanged: the first corresponds to the onset of recombination and, consequently, contributes only slightly to the total intensity, while the second makes the major contribution to the line intensity.

Using the derivatives of the spectrum has yet another advantage. The point is that we see the superposition of lines in the long-wavelength CMBR wing, causing the contrast to decrease. At the same time, the signs of the derivatives of the profile for each line at the points of their intersections are opposite. As a result, the contrast of the derivative of the spectrum is much higher, and its minima and maxima are shifted significantly from the intensity minima and maxima. This allows us to identify the lines much better and, hence, to determine the parameters of their profiles.

Note that the result obtained, when applied to observations, requires an additional careful methodological development. The observations in such a scheme are not standard ones, and, consequently, the statistics of noise and interference of various origins must be analyzed. However, at a fairly large signal-to-noise ratio in the observations, the advantages of the derivative analysis can manifest themselves in full.

CONCLUSIONS

The calculated distortions of the microwave background radiation spectrum $(\Delta B/B)$ in the range 2–50 cm caused by the superposition of the CMB hydrogen recombination radiation in subordinate lines are comparatively weak (the relative distortions are $\approx 10^{-7}$–10^{-6}), and their wavelength dependence has a low-contrast, wavy pattern. However, the contrast increases severalfold and becomes pronounced when passing to the differential spectrum of the distortions $\lambda d(\Delta B/B)/d\lambda$, which is more sensitive to model parameters than the original $(\Delta B/B)$ spectrum.

ACKNOWLEDGMENTS

This work was supported by the Russian Foundation for Basic Research (project no. 02-02-16535),

a grant from the President of Russia for Support of Leading Scientific Schools (grant NSh-1088.2003.2), and the Federal Astronomy Program.

REFERENCES

1. I. L. Beĭgman and R. A. Sunyaev, Preprint No. 163 (FIAN, Moscow, 1978).
2. I. N. Bernshteĭn, D. N. Bernshteĭn, and V. K. Dubrovich, Astron. Zh. **54**, 727 (1977) [Sov. Astron. **21**, 409 (1977)].
3. M. S. Burgin, Astron. Zh. **80**, 771 (2003) [Astron. Rep. **47**, 709 (2003)].
4. V. K. Dubrovich, Pis'ma Astron. Zh. **1**, 3 (1975) [Sov. Astron. Lett. **1**, 196 (1975)].
5. V. K. Dubrovich, Opt. Spektrosk. **63**, 439 (1987).
6. V. K. Dubrovich and N. N. Shakhvorostova, Pis'ma Astron. Zh. **30**, 563 (2004).
7. V. K. Dubrovich and V. A. Stolyarov, Astron. Astrophys. **302**, 635 (1995).
8. S. I. Grachev, Tr. Astron. Obs. SPbGU **44**, 203 (1994).
9. S. I. Grachev and V. K. Dubrovich, Astrofizika **34**, 249 (1991).
10. P. J. E. Peebles, Astrophys. J. **153**, 1 (1968).
11. V. Sahni and A. Starobinsky, astro-ph/9904398 (1999).
12. S. Seager, D. D. Sasselov, and D. Scott, Astrophys. J. **523**, L1 (1999).
13. S. Seager, D. D. Sasselov, and D. Scott, Astrophys. J., Suppl. Ser. **128**, 407 (2000).
14. V. V. Sobolev, *Moving Stellar Envelopes* (LGU, Leningrad, 1947) [in Russian].
15. Ya. B. Zel'dovich, V. G. Kurt, and R. A. Sunyaev, Zh. Éksp. Teor. Fiz. **55**, 278 (1968) [Sov. Phys. JETP **18**, 146 (1968)].

Translated by G. Rudnitskii

Astronomy Letters, Vol. 30, No. 10, 2004, pp. 663–668. Translated from Pis'ma v Astronomicheskiĭ Zhurnal, Vol. 30, No. 10, 2004, pp. 729–735.

A Semianalytical Method for Calculating the Parameters of the Electromagnetic Halos around Extragalactic Gamma-Ray Sources

S. R. Kel'ner[1], D. V. Khangulyan[2*], and F. A. Aharonian[2]

[1] *Moscow Engineering Physics Institute (State University), Kashirskoe shosse 31, Moscow, 115409 Russia*

[2] *Max Planck Institut für Kernphysik, Saupfercheckweg 1, 69117 Heidelberg, Germany*

Received February 24, 2004

Abstract—The ultrahigh-energy (>20 TeV) gamma rays emitted by active galactic nuclei can be absorbed in intergalactic space through the production of electron–positron pairs during their interaction with extragalactic background photon fields. The electrons and positrons produced by this interaction form an electromagnetic halo. We have studied the halo formation and calculated the halo radiation spectrum. The magnetic field in the halo formation region is assumed to be strong enough for the electron velocities to be isotropized. For such fields, the halo formation process can be described by the method of generations. We calculated the synchrotron and Compton backscattering radiation spectra for the total halo luminosity. We obtained the spatial distribution of the radiation for a point gamma-ray source. © *2004 MAIK "Nauka/Interperiodica".*

Key words: *active galactic nuclei, quasars and radio galaxies, electromagnetic halo, blazars, background radiation.*

INTRODUCTION

Blazars constitute a class of active galactic nuclei characterized by rapidly varying nonthermal radiation over a wide spectral range. The time scales for such systems are several days or even hours, and the observed radiation lies within the range from microwaves to ultrahigh-energy gamma rays, up to 20 TeV. Such systems attract a great deal of attention, because they can be a good test system for studying the particle acceleration mechanisms in relativistic jets. In addition, both observational and theoretical studies of these objects are of considerable interest, because this area of modern physics contains many outstanding problems; even the basic formation mechanisms of the observed objects are often unclear (see, e.g., Aharonian (2001) and references therein).

A serious obstacle to the observation of blazars is that intergalactic space is not absolutely transparent to gamma rays, because there is (cosmic microwave and thermal infrared) background radiation. High-energy gamma-ray photons interact with soft photons, with the initial gamma-ray photon being absorbed through the production of an electron–positron pair. This gives rise to an electromagnetic halo around the source. This phenomenon was first considered by Aharonian *et al.* (1994). At present, the background photon fields have been studied adequately, and there are several reliable measurements of their spectra.

The spectral distribution of the thermal radiation has two maxima, at wavelengths $\lambda \sim 1$–2 μm and $\lambda \sim 100$–200 μm. Many authors have analyzed the background field; recent measurements of the background radiation densely cover the spectrum in the range $\lambda \sim 1$–200 μm (Hauser *et al.* 1998; Lagache *et al.* 1999; Finkbeiner *et al.* 2000; Franceschini *et al.* 2001; Matsumoto 2000; Cambrésy *et al.* 2001; Pozzetti *et al.* 1998; see also the review by Hauser and Dwek 2001).

The gamma-ray radiation emitted by blazars interact with the background radiation, resulting in their absorption. Figure 1 shows the calculated mean free path of gamma rays in intergalactic space with respect to the production of an electron–positron pair during the interaction with the background photon field. Also shown here are the curves corresponding to the electron gyroradius for a magnetic field strength of 10^{-6} G and the electron mean free path for Compton backscattering. We see from our calculations that for radiation sources farther than 100 Mpc, the absorption of gamma rays with energies above several TeV in intergalactic space should be taken into account. In addition, for closer objects, the spectrum will also be severely distorted at ultrahigh energies (several

*E-mail: dmitry.khangulyan@mpi-hd.mpg.de

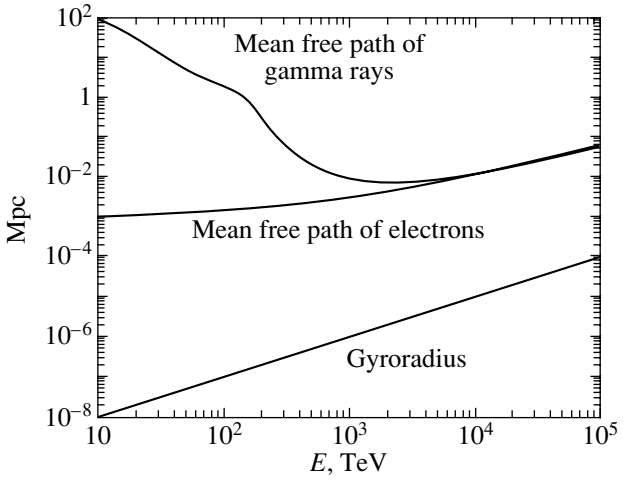

Fig. 1. Mean free paths of gamma rays and electrons and the electron gyroradius in a magnetic field.

tens of TeV) through the interaction with background radiation photons.

Thus, the blazar spectrum recorded on Earth will differ greatly from the spectrum produced by blazars, which is expected to extend to energies 10^5 TeV. Several papers are devoted to the reconstruction of the blazar spectra. Aharonian *et al.* (1999, 2001) presented the spectrum of the blazar Markarian 501 obtained during HEGRA observations in 1997 and the reconstructed spectra for various background radiation models. For sources farther than 100 Mpc, gamma rays with energies above 10 TeV will be heavily absorbed in intergalactic space (see Fig. 1). Note that this spectral range contains a sizeable fraction of the energy emitted by blazars. However, this energy is not lost, but is reradiated in another spectral range. The parameters of this secondary radiation are of interest both theoretically and observationally, since much of the blazer energy losses must be concentrated in it.

The absorption of gamma rays is determined by their interaction with soft background photons, as a result of which electron–positron pairs are produced, with the energy of the initial gamma-ray photon being transferred to these pairs. In turn, the produced electrons will also interact with the cosmic microwave background and thermal photon fields and can emit high-energy gamma rays through Compton backscattering radiation. A cascade process arises in this way, which will transfer the energy emitted by blazars in the form of ultrahigh-energy gamma rays to gamma rays with energies of the order of several TeV. Since the mean free path of such gamma rays is several hundred Mpc, these will reach the Earth and can be detected.

An important factor that increases the interest in this cascade process is the presence of a magnetic field in the region where pairs are produced, i.e., an electromagnetic halo is formed. The magnetic field affects this phenomenon in two ways: first, electron synchrotron radiation emerges and, second, the particle trajectories become curved, causing the radiation to be isotropized. The latter factor is important observationally, because even when the initial gamma-ray flux is well collimated and, hence, cannot be detected, the electromagnetic halo possesses almost isotropic radiation. This fact makes the study of electromagnetic halos of great interest, especially in connection with the observations of blazars, because their radiation is expected to originate in relativistic jets and to be well collimated.

Undeniable progress in theoretically modeling the halos has been made in recent years. Eungwanichayapant (2003) numerically calculated the electromagnetic halo by the Monte Carlo method. The formation of a halo around a point isotropic source of gamma rays with an energy of 100 TeV was considered. In the calculations, the magnetic field strength was assumed to be 10^{-12} G, which matches the expected values for several active galactic nuclei. Eungwanichayapant (2003) disregarded the electron synchrotron losses; this approximation corresponds to a weak magnetic field. However, for blazars, a stronger magnetic field, up to several μG, might be expected in the halo formation region. Such a magnetic field is typical of certain regions in the Universe, for example, clusters of galaxies. Here, we performed calculations for a magnetic field strength of 10^{-6} G. In such fields, the electrons rapidly lose their energy through synchrotron radiation. This determines the fundamental difference between our work and the case considered by Eungwanichayapant (2003). A similar case was analyzed by Timokhin *et al.* (2003), who considered a strong magnetic field. Since the development of a cascade process is completely suppressed under such conditions, only one generation of particles losing their energy through synchrotron radiation is taken into account. In this paper, we consider both the cascade process and the electron energy losses through synchrotron radiation. We use a semianalytical approach that enables us to study the particular features of the formation of electromagnetic halos around ultrahigh-energy gamma-ray sources. Semianalytical calculations of the halo structure can be performed, because the electron energy losses suppress appreciably the cascade process. Therefore, the development of a cascade can be described by the method of generations. It turned out that it would suffice to take into account the first five generations; the energy transferred to the next generations is negligible.

INTEGRATED RADIATION SPECTRA

The process in question is described by a system of Boltzmann kinetic equations. In the steady-state case, these are

$$c\mathbf{k}_\gamma \frac{\partial n_\gamma(\mathbf{r}, E_\gamma, \mathbf{k}_\gamma)}{\partial \mathbf{r}} = \left[\frac{\partial n_\gamma(\mathbf{r}, E_\gamma, \mathbf{k}_\gamma)}{\partial t}\right]_{\rm st}, \quad (1)$$

$$\mathbf{v}\frac{\partial n_e(\mathbf{r}, E_e, \mathbf{k}_e)}{\partial \mathbf{r}} = \left[\frac{\partial n_e(\mathbf{r}, E_e, \mathbf{k}_e)}{\partial t}\right]_{\rm st}.$$

Here, n_γ and n_e are the number densities of the gamma-ray photons and electrons; $\mathbf{k}_\gamma$ and $\mathbf{k}_e$ are the unit vectors directed along the gamma-ray photon wave vector and the electron velocity, respectively; and the collision integrals are defined by

$$\left[\frac{\partial n_\gamma(\mathbf{r}, E_\gamma, \mathbf{k}_\gamma)}{\partial t}\right]_{\rm st} = \frac{c}{4\pi}\int \sigma_{\rm c}(\epsilon, E_e, E_\gamma) n_{\rm ph}(\epsilon) \quad (2)$$

$$\times\, n_e(\mathbf{r}, E_e, \mathbf{k}_e) d\mathbf{o}_{\mathbf{k}_e} d\epsilon dE_e$$

$$-\,\kappa(E_\gamma) n_\gamma + Q(\mathbf{r}, E_\gamma, \mathbf{k}_\gamma),$$

$$\left[\frac{\partial n_e(\mathbf{r}, E_e, \mathbf{k}_e)}{\partial t}\right]_{\rm st} = \frac{c}{2\pi}\int \sigma_{\rm p}(\epsilon, E_e, E_\gamma)\, n_{\rm ph}(\epsilon)$$

$$\times\, n_\gamma(\mathbf{r}, E_\gamma, \mathbf{k}_\gamma) d\mathbf{o}_{\mathbf{k}_\gamma} d\epsilon dE_\gamma - L(E_e) n_e,$$

where $\sigma_{\rm c}$ and $\sigma_{\rm p}$ are the cross sections for Compton scattering and electron-positron pair production, respectively; $n_{\rm ph}$ is the background radiation photon density; Q is the gamma-ray source; and κ and L are the terms responsible for the absorption of gamma rays and the degradation of the electron energy, respectively. The gamma-ray absorption coefficient $\kappa(E_\gamma)$ is defined by

$$\kappa(E_\gamma) = c\int \sigma_{\rm p}(\epsilon, E_e, E_\gamma) n_{\rm ph}(\epsilon) d\epsilon dE_e. \quad (3)$$

We used the approximation of continuous losses to determine the electron energy losses.

As was mentioned above, the magnetic filed strength in the jet region is 10^{-7}–10^{-6} G. For such a field strength, the electrons in the emerging cascade process

$$n_\gamma^{(0)} \longrightarrow n_e^{(1)} \longrightarrow n_\gamma^{(1)} \longrightarrow \ldots$$

will rapidly lose their energy through synchrotron losses. Under these conditions, the electrons of only a few generations will affect significantly the spectrum and spatial distribution of the halo radiation; the energy transferred subsequently will be negligible. These physical conditions allow us to describe the development of a cascade by the method of generations and to calculate the synchrotron and Compton backscattering radiation spectra.

We assume the problem to be stationary and represent the number densities of the gamma-ray photons and electrons as

$$n_\gamma(\mathbf{r}, E_\gamma, \mathbf{k}_\gamma) = n_\gamma^{(0)}(\mathbf{r}, E_\gamma, \mathbf{k}_\gamma) \quad (4)$$

$$+\, n_\gamma^{(1)}(\mathbf{r}, E_\gamma, \mathbf{k}_\gamma) + n_\gamma^{(2)}(\mathbf{r}, E_\gamma, \mathbf{k}_\gamma) + \ldots,$$

$$n_e(\mathbf{r}, E_e, \mathbf{k}_e) = n_e^{(1)}(\mathbf{r}, E_e, \mathbf{k}_e)$$

$$+\, n_e^{(2)}(\mathbf{r}, E_e, \mathbf{k}_e) + n_e^{(3)}(\mathbf{r}, E_e, \mathbf{k}_e) + \ldots,$$

where the superscripts denote the particle generations. The zeroth-generation gamma-ray photons are described by the equation

$$c\mathbf{k}_\gamma \frac{\partial n_\gamma^{(0)}(\mathbf{r}, E_\gamma, \mathbf{k}_\gamma)}{\partial \mathbf{r}} \quad (5)$$

$$= Q(\mathbf{r}, E_\gamma, \mathbf{k}_\gamma) - \kappa(E_\gamma) n_\gamma^{(0)}(\mathbf{r}, E_\gamma, \mathbf{k}_\gamma);$$

for the particles of the next generations, we obtain

$$\mathbf{v}\frac{\partial n_e^{(i+1)}(\mathbf{r}, E_e, \mathbf{k}_e)}{\partial \mathbf{r}} \quad (6)$$

$$= \frac{c}{2\pi}\int \sigma_{\rm p}(\epsilon, E_e, E_\gamma)\, n_{\rm ph}(\epsilon) n_\gamma^{(i)}$$

$$\times\, (\mathbf{r}, E_\gamma) d\mathbf{o}_{\mathbf{k}_\gamma} d\epsilon dE_\gamma - L(E_e) n_e^{(i+1)},$$

$$c\mathbf{k}_\gamma \frac{\partial n_\gamma^{(i)}(\mathbf{r}, E_\gamma, \mathbf{k}_\gamma)}{\partial \mathbf{r}} = \frac{c}{4\pi}\int \sigma_{\rm c}(\epsilon, E_e, E_\gamma)\, n_{\rm ph}(\epsilon)$$

$$\times\, n_e^{(i)}(\mathbf{r}, E_e, \mathbf{k}_e) d\mathbf{o}_{\mathbf{k}_e} d\epsilon dE_e - \kappa(E_\gamma) n_\gamma^{(i)}.$$

This system of equations describes the formation of an electromagnetic halo around an ultrahigh-energy gamma-ray source.

Of interest is to consider the total halo radiation, which requires introducing the integrated particle densities

$$N_\gamma^{(i)}(E_\gamma) = \int n_\gamma^{(i)}(\mathbf{r}, E_\gamma, \mathbf{k}_\gamma) dV d\mathbf{o}_{\mathbf{k}_\gamma}, \quad (7)$$

$$N_e^{(i)}(E_e) = \int n_e^{(i)}(\mathbf{r}, E_e, \mathbf{k}_e) dV d\mathbf{o}_{\mathbf{k}_e}.$$

For these quantities, we obtain the following closed system of equations from (5) and (6):

$$Q(E_\gamma) - \kappa(E_\gamma) N_\gamma^{(0)} = 0, \quad (8)$$

$$2c\int \sigma_{\rm p}(\epsilon, E_e, E_\gamma)\, n_{\rm ph}(\epsilon)$$

$$\times\, N_\gamma^{(i)}(E_\gamma) d\epsilon dE_\gamma - L(E_e) N_e^{(i+1)} = 0,$$

$$c\int \sigma_{\rm c}(\epsilon, E_e, E_\gamma)\, n_{\rm ph}(\epsilon)$$

$$\times\, N_e^{(i)}(E_e) d\epsilon dE_e - \kappa(E_\gamma) N_\gamma^{(i)} = 0.$$

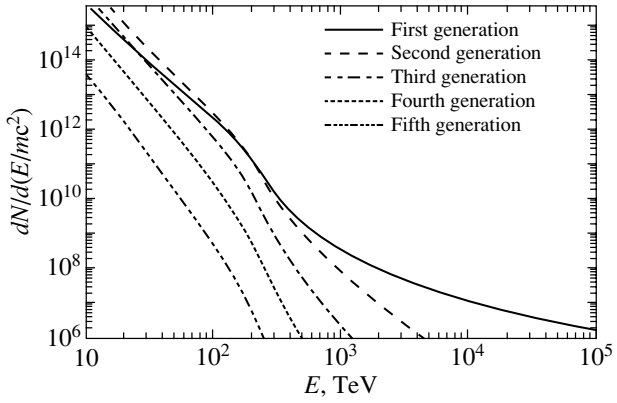

Fig. 2. Generations of gamma-ray photons.

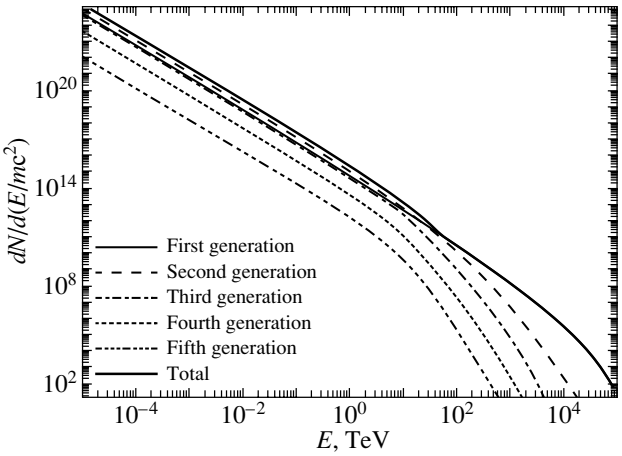

Fig. 3. Generations of electrons.

Here,

$$Q(E_\gamma) = \int Q(\mathbf{r}, E_\gamma, \mathbf{k}_\gamma) dV d\mathbf{o}_{\mathbf{k}_\gamma}.$$

To describe the degradation of the electron energy, let us consider the integrated electron spectrum

$$\tilde{N}(E,t) = \int_E^\infty N_e(E',t)dE'. \qquad (9)$$

If the electrons lose their energy continuously, then

$$\tilde{N}(E - \frac{dE}{dt}, t+dt) = \tilde{N}(E,t). \qquad (10)$$

This yields the following relation:

$$\frac{\partial \tilde{N}}{\partial E}\frac{dE}{dt} = \frac{\partial \tilde{N}}{\partial t}, \qquad (11)$$

which enables us to express the electron energy degradation as

$$L(E)N_e = \frac{\partial N_e}{\partial t} = \frac{\partial}{\partial E}\left\{N_e \frac{dE}{dt}\right\}. \qquad (12)$$

Here, the quantity dE/dt is determined by the electron losses through synchrotron radiation and Compton backscattering.

With the above assumptions, the integrated densities are described by equations of the form

$$Q(E_\gamma) - \kappa(E_\gamma)N_\gamma^{(0)} = 0,$$

$$N_e^{(i+1)}(E_e) = \frac{2c}{|dE/dt|}\int_{E_e}^\infty dE'_e \qquad (13)$$

$$\times \int \sigma_{\rm p}\left(\epsilon, E'_e, E_\gamma\right) n_{\rm ph}(\epsilon) N_\gamma^{(i)}(E_\gamma) d\epsilon dE_\gamma,$$

$$c\int \sigma_{\rm c}\left(\epsilon, E_e, E_\gamma\right) n_{\rm ph}(\epsilon)$$

$$\times N_e^{(i)}(E_e) d\epsilon dE_e - \kappa(E_\gamma)N_\gamma^{(i)} = 0.$$

The system of Eqs. (13) was solved numerically. We calculated the generations of gamma-ray photons and electrons as well as the synchrotron and Compton backscattering radiation spectra. For the spectrum of the source of primary gamma-ray photons in the form

$$Q(E_\gamma) = \frac{Q_0}{E_\gamma{}^{1.5}}, \qquad (14)$$

the results of our calculations are presented in Figs. 2–5.

THE SPATIAL STRUCTURE OF THE HALO

The spatial distribution of the halo radiation can be calculated using the approximation of stationary electrons. This approximation may be used, because, as we see from Fig. 1, the mean free path of gamma-ray photons is much larger than the typical displacement of electrons determined by the electron gyroradius in a magnetic field R_g. In addition, the relation $\Lambda_{\rm c} \gg R_g$ (where $\Lambda_{\rm c}$ is the electron mean free path in intergalactic space) always holds. This means that an electron makes several complete turns in a magnetic field before it emits a gamma-ray photon through Compton backscattering radiation. Thus, the spatial structure of the halo is determined by the mean free path of gamma-ray photons, while electrons gyrating in the magnetic field displace only slightly. In this case, we may assume that the electron velocities are isotropic, and, as a result, secondary gamma-ray photons are also emitted isotropically.

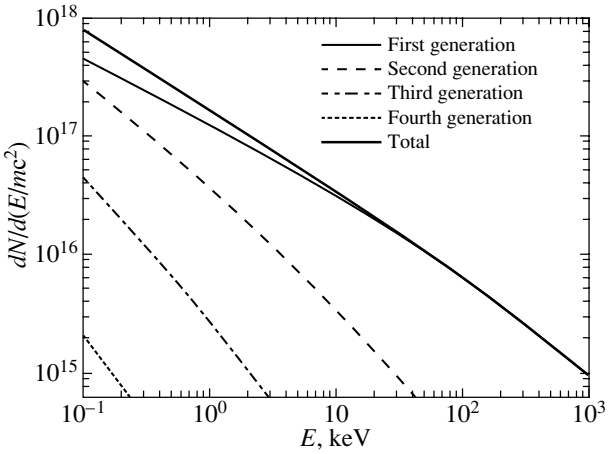

Fig. 4. Synchrotron radiation of the halo.

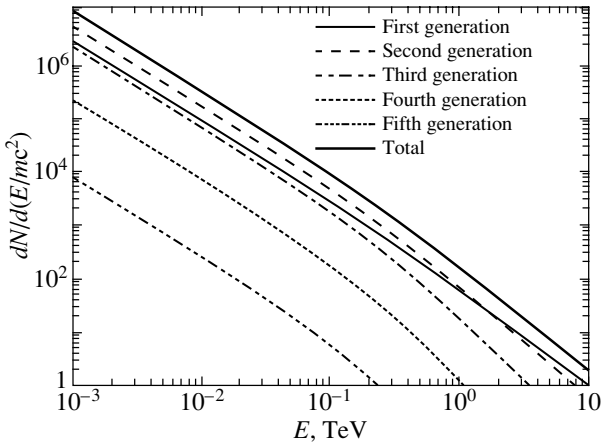

Fig. 5. Halo radiation through Compton backscattering.

In these approximations, the system of Boltzmann kinetic equations describing the process under consideration can be written as

$$c\mathbf{k}_\gamma \frac{\partial n_\gamma^{(0)}(\mathbf{r}, E_\gamma, \mathbf{k}_\gamma)}{\partial \mathbf{r}} = Q(\mathbf{r}, E_\gamma, \mathbf{k}_\gamma) - \kappa(E_\gamma) n_\gamma^{(0)}(\mathbf{r}, E_\gamma, \mathbf{k}_\gamma), \tag{15}$$

$$n_e^{(i+1)}(\mathbf{r}, E_e) = \frac{c}{2\pi \left|\frac{dE}{dt}\right|} \int\limits_{E_e}^{\infty} dE'_e \times \int \sigma_{\rm p}\left(\epsilon, E'_e, E_\gamma\right) n_{\rm ph}(\epsilon) n_\gamma^{(i)}(\mathbf{r}, E_\gamma, \mathbf{k}_\gamma) d\mathbf{o}_{\mathbf{k}_\gamma} d\epsilon dE_\gamma, \tag{16}$$

$$c\mathbf{k}_\gamma \frac{\partial n_\gamma^{(i)}(\mathbf{r}, E_\gamma, \mathbf{k}_\gamma)}{\partial \mathbf{r}} = c \int \sigma_{\rm c}\left(\epsilon, E_e, E_\gamma\right) n_{\rm ph}(\epsilon) \times n_e^{(i)}(\mathbf{r}, E_e) d\epsilon dE_e - \kappa(E_\gamma) n_\gamma^{(i)}(\mathbf{r}, E_\gamma, \mathbf{k}_\gamma). \tag{17}$$

The system of equations (15)–(17) can be solved semianalytically. To obtain the solution, we must specify the form of the sources. We performed our calculations for a source of the form

$$Q(\mathbf{r}, E_\gamma, \mathbf{k}_\gamma) = \delta(\mathbf{r}) q(E_\gamma), \tag{18}$$

which corresponds to a point gamma-ray source that is located at the coordinate origin and that emits gamma rays isotropically. In this case, the solution of Eq. (15) is

$$n_\gamma^{(0)}(\mathbf{r}, E_\gamma, \mathbf{k}_\gamma) = \frac{q(E_\gamma)}{4\pi r^2 c} e^{-\frac{\kappa(E_\gamma) r}{c}}. \tag{19}$$

In the approximation of an isotropic velocity distribution, we obtain for the first-generation electrons

$$n_e^{(1)}(\mathbf{r}, E_e) = \frac{1}{4\pi r^2 c} \int\limits_0^{\infty} dE_\gamma \Xi(E_e, E_\gamma) q(E_\gamma) e^{-\frac{\kappa(E_\gamma) r}{c}}, \tag{20}$$

where the quantity $\Xi(E_e, E_\gamma)$ defines the probability of an electron with energy E_e being produced by a gamma-ray photon with energy E_γ during the interaction with the microwave and infrared background radiation. This quantity is given by

$$\Xi(E_e, E_\gamma) = \frac{2c}{|dE/dt|} \times \int\limits_{E_e}^{\infty} \int \sigma_{\rm p}\left(\epsilon, E'_e, E_\gamma\right) n_{\rm ph}(\epsilon) d\epsilon dE'_e. \tag{21}$$

Electrons will represent an isotropic gamma-ray source; for such a source, the distribution of gamma-ray photons has the form (19).The solution of Eq. (17) can then be represented as

$$n_\gamma^{(i)}(\mathbf{r}, E_\gamma) = \int dV' \frac{e^{-\frac{\kappa(E_\gamma)|\mathbf{r}-\mathbf{r}'|}{c}}}{4\pi|\mathbf{r}-\mathbf{r}'|^2 c} \times \int dE_e G(E_\gamma, E_e) n_e^{(i)}(\mathbf{r}', E_e), \tag{22}$$

where

$$G(E_\gamma, E_e) = c \int \sigma_{\rm c}\left(\epsilon, E_e, E_\gamma\right) n_{\rm ph}(\epsilon) d\epsilon. \tag{23}$$

We numerically solved this system using the above approximations for a point source of gamma-ray photons with the energy distribution (14). We obtained the synchrotron and Compton backscattering radiation spectra at various points in space. The results of our calculations are presented in Figs. 6 and 7.

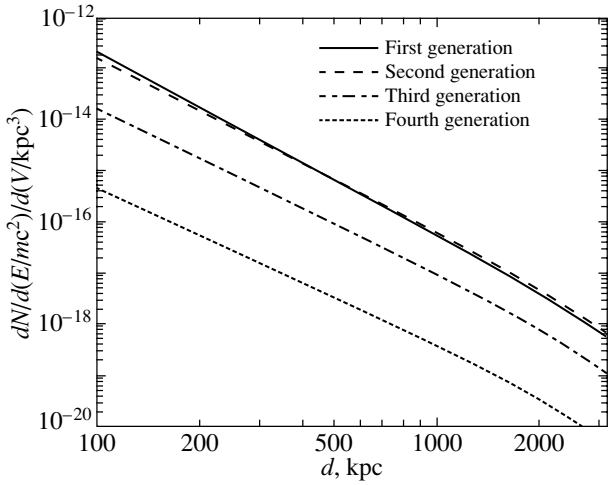

Fig. 6. Spatial distribution of the synchrotron radiation from the halo for an energy of 1 keV.

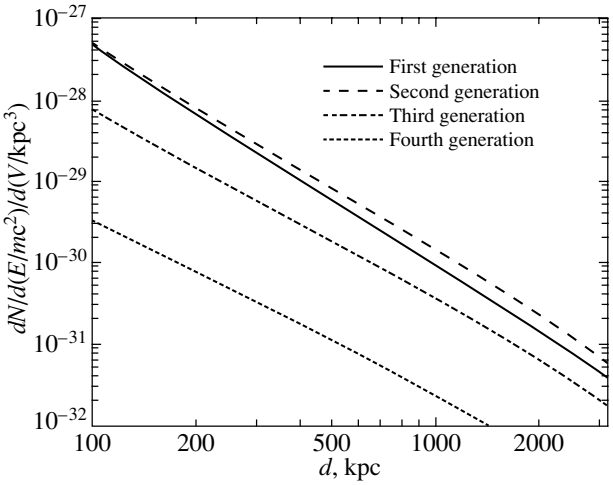

Fig. 7. Spatial distribution of the halo radiation through Compton backscattering for an energy of 500 GeV.

CONCLUSIONS

The spatial distribution of the halo radiation intensity and its energy spectrum depend significantly on the primary photon spectrum, the infrared photon spectrum, and the magnetic field strength. Therefore, the detection of halos will provide additional information about the physical conditions in the vicinity of galactic nuclei and about the time evolution of the infrared photon field.

It should be noted that searching for electromagnetic halos around active galactic nuclei is a fairly complex task and requires not only sensitive gamma-ray telescopes, but also accurate theoretical calculations of the spectra and angular distribution of the halo radiation. In this paper, we have considered the formation of an electromagnetic halo around blazers and calculated the spectra of the total halo radiation and the spatial distribution of the radiation intensity around a point source of gamma-ray photons with energies of the order of several TeV. Note that the method used can be applied to various magnetic field strengths.

The results of our analysis are primarily aimed at observationally searching for electromagnetic halos with next-generation gamma-ray telescopes, for example, the Hess telescope. The detection of halos will extend considerably the observational data on blazars and blazarlike objects. In particular, it will allow us to search for blazars in which the jet direction does not coincide with the line of sight. This will make it possible not only to extend the class of objects belonging to blazars, but also to observe these objects at various angles. We plan to present a detailed analysis of this in the near future.

ACKNOWLEDGMENTS

This work was supported by the Russian Foundation for Basic Research (project no. 03-02-17098).

REFERENCES

1. F. A. Aharonian, *Rapporteur and Highlight Papers of ICRC 2001,* Ed. by K.-H. Kampert, G. Hainzelmann, and C. Spiering (Copernicus Gesellschaft, Hamburg, 2001), p. 250.
2. F. A. Aharonian, A. G. Akhperjanian, J. A. Barrio, *et al.* (HEGRA Collab.), Astron. Astrophys. **349**, 29 (1999).
3. F. A. Aharonian, A. G. Akhperjanian, J. A. Barrio, *et al.* (HEGRA Collab.), Astron. Astrophys. **366**, 746 (2001).
4. F. A. Aharonian, P. S. Coppi, and H. Völk, Astrophys. J. **423**, L5 (1994).
5. L. Cambresy, W. T. Reach, C. A. Beichman, *et al.*, Astrophys. J. **555**, 563 (2001).
6. A. Eungwanichayapant, Preprint No. 053 (Max-Planck-Institut für Kernphysik, Heidelberg, 2003); http://www.mpi-hd.mpg.de/biblio/preprints/2003-053.pdf.
7. D. P. Finkbainer, M. Devis, and D. J. Schlegel, Astrophys. J. **544**, 81 (2000).
8. A. Franceschini, H. Aussel, C. J. Cesarsky, *et al.*, Astron. Astrophys. **378**, 1 (2001).
9. M. G. Hauser, R. G. Arendt, T. Kelsall, *et al.*, Astrophys. J. **508**, 25 (1998).
10. M. G. Hauser and E. Dwek, Annu. Rev. Astron. Astrophys. **39**, 249 (2001).
11. G. Lagache, A. Abergel, F. Boulanger, *et al.*, Astron. Astrophys. **344**, 322 (1999).
12. T. Matsumoto, ISAS Sci. Rep. SP, No. 14 (2000).
13. L. Pozzetti, P. Madau, G. Zamorani, *et al.*, Mon. Not. R. Astron. Soc. **298**, 1133 (1998).
14. A. N. Timokhin, F. A. Aharonian, and A. Yu. Neronov, astro-ph/0305149 (2003).

Translated by G. Rudnitskii

Astronomy Letters, Vol. 30, No. 10, 2004, pp. 669–674. Translated from Pis'ma v Astronomicheskiĭ Zhurnal, Vol. 30, No. 10, 2004, pp. 736–742.

Broadband X-ray Spectrum of XTE J1550–564 during the Outburst of 2003

V. A. Aref'ev[1*], M. G. Revnivtsev[1,2], A. A. Lutovinov[1], and R. A. Sunyaev[1,2]

[1] *Space Research Institute, Russian Academy of Sciences, Profsoyuznaya ul. 84/32, Moscow, 117810 Russia*

[2] *Max Planck Institut für Astrophysik, Karl Schwarzschild Str. 1, 85740 Garching bei München, Germany*

Received March 25, 2004

Abstract—We present the INTEGRAL and RXTE X-ray observations of XTE J1550–564, a Galactic microquasar and a black hole candidate, during its outburst in the spring of 2003. The source during the outburst was in a canonical hard state, and its spectrum remained constant in both the rise and decay phases. © *2004 MAIK "Nauka/Interperiodica".*

Key words: *X-ray sources, black holes, transients.*

INTRODUCTION

The X-ray transient XTE J1550–564 was discovered by the All-Sky Monitor (ASM) on board the RXTE satellite on September 7, 1998 (Smith 1998). Shortly after its discovery, it was detected in the optical (Orosz 1998) and radio (Campbell-Wilson *et al.* 1998) wavelength ranges, which allowed its position to be determined with a high accuracy. During the 1998–1999 outburst, XTE J1550–564 passed through all the canonical spectral states of X-ray transients containing black holes candidate: high/soft, low/hard, and intermediate. The spectral and temporal behavior of the radiation from the source proved to be unusually complex (Homan *et al.* 2001). Two weeks after its discovery, a very intense X-ray outburst was detected on September 20–21, 1998, during which the flux from the source reached 6.8 Crab (Remillard *et al.* 1998). This corresponds to a luminosity of 9.4×10^{38} erg s^{-1} in the energy range 2–100 keV for an assumed distance of 5.3 kpc to the source (Orosz *et al.* 2002), which roughly corresponds to the Eddington luminosity for this object. Recent Chandra observations have revealed X-ray radiation from the relativistic jets that, judging by their distance from the source and their velocity, emerged at the time of this Eddington outburst (Tomsik *et al.* 2003). The X-ray jets, which were also observed as superluminar jets in the radio wavelength range (Hannikainen *et al.* 2001), allowed XTE J1550–564 to be classified as a Galactic microquasar. Optical observations showed that the orbital period of the system is $1^{\rm d}.54$, and the mass of the compact object is about $10M_\odot$ (Orosz *et al.* 2002), which is well above the upper limit for the neutron-star mass.

XTE J1550–564 has exhibited several more strong outbursts: in 2000 (Tomsik *et al.* 2001a; Rodriguez *et al.* 2003), 2001 (Tomsik *et al.* 2001b), 2002 (Belloni *et al.* 2002), and 2003 (Dubath *et al.* 2003). However, none of these events compared to the first event in complexity of the light-curve behavior and in intensity (Fig. 1). The light curves of all the subsequent outbursts exhibited more standard shapes with fast rise and slow decay and virtually no spectral variability. Of great interest is the short time interval between the neighboring outbursts of activity observed over the last six years, because the source had not been detected for at least 25 years before its appearance in the X-ray sky in 1998.

In this paper, we present the observations of XTE J1550–564 by the INTEGRAL (data of the Core program) and RXTE (publicly available data during observatory slew) during the last outburst (the spring of 2003).

DATA ANALYSIS AND RESULTS

The INTEGRAL international gamma-ray observatory was launched into a high-apogee orbit from the Baikonur Cosmodrome by a Russian Proton rocket carrier on October 17, 2002 (Eismont *et al.* 2003). The instrumentation of the observatory includes four instruments that allow simultaneous X-ray, gamma-ray, and optical observations of a source to be performed (Winkler *et al.* 2003a). As part of the Core program, the observatory is systematically scanning the Galactic plane to search for X-ray transients

*E-mail: gita@hea.iki.rssi.ru

1063-7737/04/3010-0669$26.00

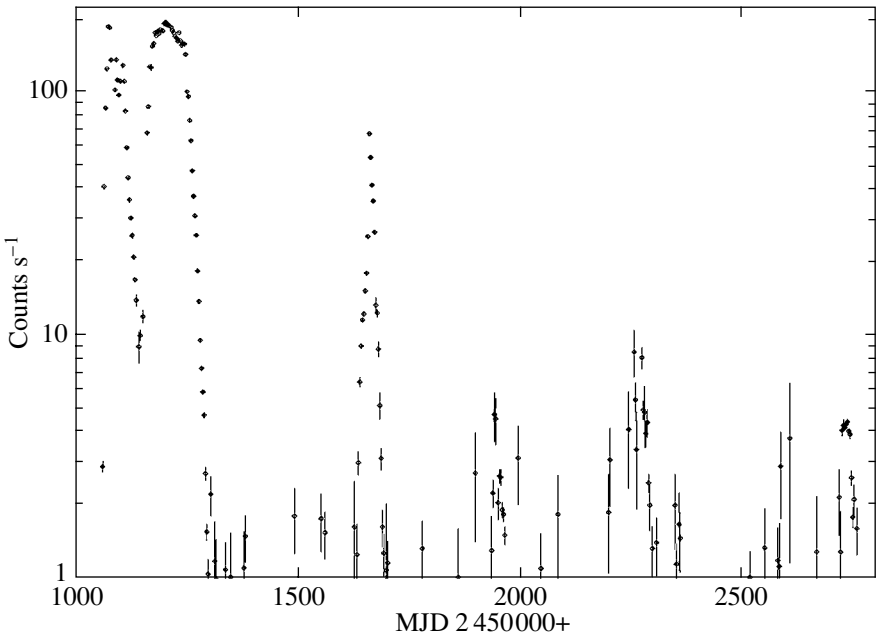

Fig. 1. Long-term ASM/RXTE 2–12 keV light curve for XTE J1550–564 since its discovery in 1998.

and to study the variability of known X-ray sources (Winkler *et al.* 2003b). During such observations in the spring of 2003, another outburst of activity in XTE J1550–564 was discovered (Dubath *et al.* 2003).

During these observations, the source was far from the optical axis of the INTEGRAL telescopes for most of the time (except TOO (target of opportunity observations) when the satellite was specially oriented toward the source and which are not consider here). Therefore, in this paper, we analyze only data from the IBIS telescope (the ISGRI detector; Lebrun *et al.* 2003) and the SPI spectrometer (Vedrenne *et al.* 2003), which have large fields of view (29° × 29° and 35° × 35°, respectively).

We processed the data from the ISGRI detector of the IBIS telescope using a method described by Revnivtsev *et al.* (2004). The SPI data were analyzed using the OSA 3.0 software package.[1] To construct the spectrum of the source from the IBIS/ISGRI data, we used the ratio of its fluxes measured in different energy ranges to the fluxes recorded from the Crab Nebula by IBIS/ISGRI in the same energy ranges using the standard form of the spectrum for the Crab Nebula, $dN(E) = 10E^{-2.1}dE$ photons cm^{-2} s^{-1} keV^{-1}. To verify the validity of the processing algorithms used and to estimate the amplitudes of the systematic uncertainties in the spectra obtained, we applied the method mentioned above to a series of observations of the Crab Nebula. Our analysis of the IBIS/ISGRI data revealed systematic uncertainties at a level of 2–5% and ∼ 10% for the spectral analysis and the absolute flux normalization, respectively. An analysis of the SPI data showed that the standard software package (OSA 3.0) systematically overestimates the flux from the source, while the shape of the spectrum is reproduced correctly. Therefore, below, we renormalize the SPI values to the IBIS/ISGRI values.

Since the source was outside the field of view of the JEM-X monitor onboard the INTEGRAL observatory, to supplement the hard X-ray data with the observational data in the standard X-ray energy range, we used publicly available data from the RXTE observatory—the ASM and PCA observations obtained during the slew when XTE J1550–564 was observed from March 27 through April 21, 2003. We analyzed the RXTE/PCA data using version 5.3 of the standard FTOOLS/LHEASOFT package. To reduce the systematic uncertainties in the spectra obtained, we used only the upper layer of the anodes of the PCA detector and excluded from our analysis the data of the PCU0 detector, because it had no propane veto layer since 2000, which greatly reduced the effect of the background on the results obtained.

The Light Curve

INTEGRAL observed the source XTE J1550–564 several times in the spring of 2003 during its scanning of the Galactic plane and deep survey of

[1] http://isdc.unige.ch/index.cgi?Soft+soft

the central radian of the Galaxy. The effective time of the IBIS/INTEGRAL observations of the source was about 300 ks from early March 2003 until the outburst onset (March 24, 2003). The upper limit on the 18–60 keV X-ray flux from XTE J1550–564 obtained by averaging all of the measurements before the outburst (IBIS/ISGRI measurements) was ~1 mCrab.

The outburst recorded by the IBIS telescope started on March 24.2, 2003 (Dubath *et al.* 2003). Subsequently, the source fell several times within the INTEGRAL field of view at the initial rise phase and at the peak of activity (March 24–25 and April 8, 2003). Figure 2 shows its light curve constructed from RXTE and INTEGRAL data. We see from this figure that the total duration of the outburst in the standard X-ray energy range (RXTE data) was about 50 days, and the shape of its light curve proved to be asymmetric with a ~10-days rise in intensity to the peak value followed by a ~35–40-day smooth decay. Because of the limited amount of INTEGRAL data, we cannot accurately determine the duration of the outburst in the hard X-ray and gamma-ray energy ranges. Note only that the peak soft X-ray intensity of the source (~70 mCrab) is much lower than the hard X-ray intensity (~200 mCrab), suggesting that the source has a hard radiation spectrum.

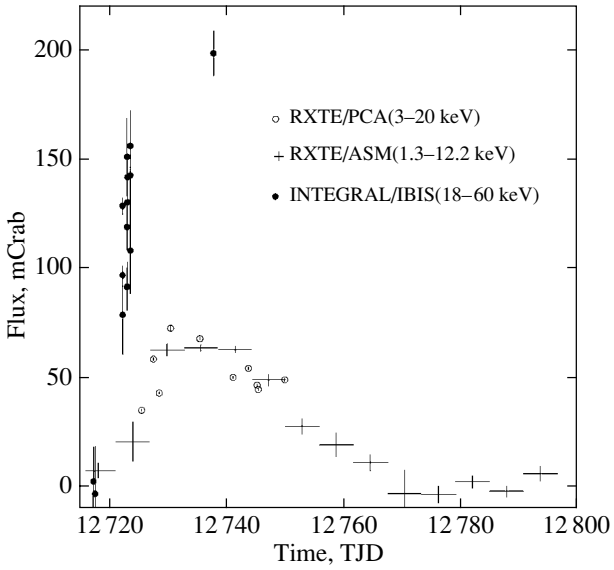

Fig. 2. Light curve of XTE J1550–564 during the outburst of 2003 obtained by the INTEGRAL and RXTE observatories.

The Spectrum

A preliminary analysis of the spectrum for XTE J1550–564 showed that its shape changed only slightly during the outburst, which allowed us to analyze the object's spectrum averaged over all the available data.

Figure 3 shows the broadband spectra of XTE J1550–564 obtained by the methods described above from RXTE and INTEGRAL data during the outburst of 2003. Also shown for comparison are the spectra of the source averaged over the hard phases of the 2000 (see, e.g., Rodriguez *et al.* 2003) and 2001 outbursts. We see that the 2001 and 2003 outbursts had much harder spectra than that the 2000 outburst.

The standard model of an accretion flow in binary systems with black holes in a low spectral state assumes that, in this state, an optically thick accretion disk ends (Poutaten *et al.* 1997), e.g., evaporates (Meyer *et al.* 2000), at a distance of ~ 10–$100R_{\rm g}$ from the black hole, and the main energy release takes place in an optically thin hot cloud of plasma at radii $R < 10$–$100R_{\rm g}$ (see Fig. 4). In this case, the X-ray spectrum is formed through photon Comptonization in a hot, optically thin region (Sunyaev and Titarchuk 1980). The component that arises from the reflection of this hard radiation from an optically thick cold accretion disk is added to this spectrum (Basko *et al.* 1974; George and Fabian 1991). To describe the spectrum, we used the Comptonization model by Poutanen and Svensson (1996), which also includes the spectral component that describes the reflection of hot radiation from a cold neutral medium (the compps model in the XSPEC spectral package). This model describes the high-energy spectral cutoff more accurately than does the simple analytical model with an exponential cutoff of the form ($F \propto E^{-\Gamma}\exp(-E/kT)$). The temperature of the soft photons that were subsequently Comptonized in the hot cloud was fixed at 0.1 keV. The model parameters inferred from spectral fitting are listed in the table. Note that fitting the spectrum by the compps model yields a large optical depth of the cloud, $\tau \approx 2$–4, which is rather atypical of accreting black holes in the hard spectral state. On the other hand, such a large optical depth raises the question of whether the chosen model, which was developed for an optically thin case (Poutanen and Svensson 1996), is applicable. To verify its applicability, we performed intensive Monte Carlo simulations in the approximation of spherical geometry for the standard optical depth $\tau = 1$ and for $\tau = 5$ at the coronal electron temperatures listed in the table. The parameters of the spectrum obtained from our Monte Carlo simulations closely matched those inferred from the Comptonization model to within better than 5% in both cases.

When fitting the data, we assumed that there were systematic uncertainties of 1% and 5% in the flux measurements in each of the RXTE/PCA and INTEGRAL/IBIS channels, respectively. The equiv-

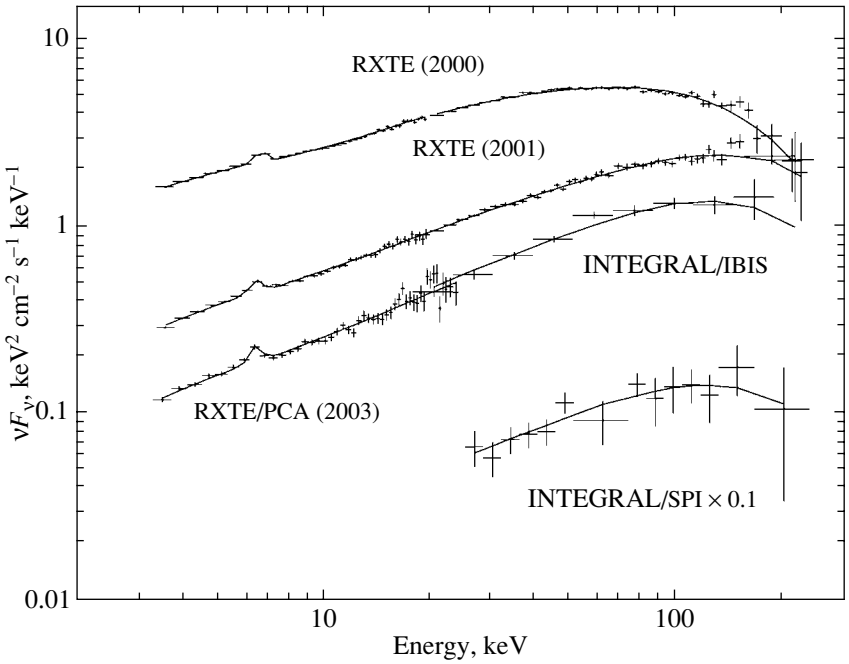

Fig. 3. Broadband spectrum of XTE J1550–564 taken by the INTEGRAL and RXTE observatories during the outburst of 2003. The spectra obtained by averaging all of the RXTE observations during the hard phase of the outburst of XTE J1550–564 in 2000 and during the outburst in 2001 are shown for comparison.

alent hydrogen column density was fixed at $N_{\rm H}$ at 10^{22} cm^{-2} (Kaaret *et al.* 2003).

Note that the available uncertainties in the mutual calibration of the RXTE/PCA and INTEGRAL/IBIS + SPI instruments strongly affect the parameter of the reflected spectral component ($R = \Omega/2\pi$). Therefore, although this component was formally detected in the spectrum of XTE J1550–564 at a statistically significant level, caution should be exercised in interpreting it. It is also worth noting that the absolute width of the fluorescence iron line at ~6.4 keV was recorded at 0.1 keV (i.e., an infinitely small width unrecordable by the RXTE/PCA spectrometer with a resolution of ~1.1 keV in this energy range) in all observations (except the 2000 outburst). The line width was found to be ~0.6–0.7 keV only in the spectrum taken during the outburst of 2000.

DISCUSSION

The X-ray transient XTE J1550–564 is located in the Galactic plane at about 4° from the known bright source Cir X-1 in a region that has been repeatedly observed with various detectors. After at least 25 years of the off state, as indicated by the nondetection of the object by X-ray observatories prior to 1998, XTE J1550–564 entered a new phase in which it generates outbursts about once a year. This behavior differs strikingly from the ordinary behavior of X-ray transients containing black holes (McClintock and Remillard 2003).

The first two outbursts (in 1998–1999 and 2000) demonstrated complex light curves and numerous spectral transitions (this was particularly true of the first outburst). During the first outburst (Fig. 1, MJD 51 036–51 299), the source was observed in the ultrahigh and high/soft spectral states and exhibited an M-shaped light curve not only in the standard X-ray range, but also in the broadband (2–200 keV) X-ray range (Sobczak *et al.* 2000; Aleksandrovich and Aref'ev 2002). Sobczak *et al.* (2000) described its spectrum as the sum of two components: a multicolor, optically thick accretion disk (Shakura and Sunyaev 1973) and a power-law component. The first phase of the outburst (until ~MJD 51 150) was dominated by the power-law component, which probably originates in the hot corona, while the disk radiation made a much larger contribution at the second phase.

The second (2000) outburst was less intense, with the ASM/RXTE flux reaching ~ 1 Crab at the maximum, and its light curve was much simpler: the source was in the hard spectral state at the initial and final phases of the outburst, when the flux from XTE J1550–564 in the standard X-ray energy range was low (Rodriguez *et al.* 2003). At the maximum of the outburst, the source passed to an intermediate state in which an appreciable contribution of the radiation from the accretion disk was observed.

Table

Outburst	kT[a], keV	τ[b]	$R, \Omega/2\pi$[c]	$EW_{\rm line}$[d], eV	Flux[e], erg s^{-1} cm^{-2}	χ^2/d.o.f.
2003	50 ± 10	3.4 ± 0.9	0.25 ± 0.13	120 ± 30	3.8×10^{-9}[f]	1.20
2001	63 ± 6	2.5 ± 0.4	0.27 ± 0.08	96 ± 25	5.5×10^{-9}	1.16
2000	42 ± 1	2.8 ± 0.2	0.7 ± 0.1	99 ± 20	2.0×10^{-8}	1.6

Notes: The inclination of the system was fixed at $i = 73°$ (Orosz *et al.* 2002).

[a] Coronal electron temperature.

[b] Optical depth.

[c] Geometric factor indicating the fraction of the reflected component in the spectrum.

[d] Equivalent width of the fluorescence iron line.

[e] Flux in the energy range 3–200 keV.

[f] Flux calculated by recalculating the RXTE/PCA spectrum to the INTEGRAL/IBIS flux.

Rodriguez *et al.* (2003) found that the transitions between the hard and intermediate states and back during the 2000 outburst showed a hysteresis effect. The first transition occurred at a 2–200 keV flux of $\sim 2.3 \times 10^{-8}$ erg cm^{-2} s^{-1}, whereas the reverse transition occurred at a flux of $\sim 1.1 \times 10^{-8}$ erg cm^{-2} s^{-1}. Evidence of such a hysteresis can also be found in the first outburst. As was found by Sobczak *et al.* (2000), the photon index of the power-law spectrum was less than 2 during the first days of the 1998–1999 outburst as long as the source's flux was lower than several units times 10^{-8} erg cm^{-2} s^{-1}. At the same time, the X-ray flux from the disk component was insignificant ($\sim$5% of the total flux). A comparison of the PCA/RXTE and BATSE/CGRO data (Aleksandrovich and Aref'ev 2002) corroborates the conclusion that the source was in the low/hard state in the period MJD 51 063–51 066. XTE J1550–564 did not return to the hard state after its transition to the high/soft state until the end of the observations (and the outburst) down to fluxes of several units times 10^{-10} erg cm^{-2} s^{-1}. Recently, Maccarone (2003) analyzed a large number of soft X-ray sources that exhibited a transition from the soft/high state to the hard/low state. He concluded that this transition occurs, with a high accuracy, at a level of 1–4% of the Eddington luminosity and suggested that the flux at the transition could be an independent indicator of the distance to the source. Observational data for XTE J1550–564 show that the flux at the transition from the high/soft to low/hard state may change greatly for the same source. The flux at the transition differed by about two orders of magnitude for the 1998–1999 and 2000 outbursts.

In none of the subsequent outbursts in 2001–2003 did the source reach a flux at which a transition to the high/soft spectral state was expected (see the table and Belloni *et al.* (2002)). The 2003 outburst of XTE J1550–564 was observed by RXTE and INTEGRAL over a wide energy range since the first days of the event. The source remained in the canonical low/hard state throughout the outburst, exhibiting large variability on short time scales (Miller and Homan 2003).

To describe the spectrum of XTE J1550–564 in the hard spectral state, we used the Comptonization model by Poutanen and Svensson (1996), whose best-fit parameters are listed in the table. For the convenience of comparison, we also list the parameters of the source's spectrum during the hard state of 2000 and during the 2001 outburst. We see from Fig. 3 that the spectrum of the 2003 outburst is much harder that the 2000 spectrum and is similar to the spectrum of the 2001 outburst. The large optical depth may reflect the fact that the source has a rather large inclination, and we look at the central source through the entire thickness of the central cloud (see Fig. 4.). In such a geometry, the optical depth perpendicular to the accretion disk may be expected to be smaller than the optical depth parallel to the disk. We performed Monte Carlo simulations in the approximation of a unit-height cylinder where the ratio of the hot-zone sizes is $H/R = 0.3$, the source of soft photons, a flat disk of size $r = H$, is located in the central part of the hot zone, and the optical depth is given in units of length. We found that for the optical depths $\tau \approx 1$–3 concerned, the spectrum emerging in a direction parallel to the disk is much harder (in the standard X-ray energy range 3–20 keV; i.e., the slope of the power-law part of the spectrum is much smaller) than the spectrum emerging in a direction perpendicular to the disk.

In conclusion, let us note an interesting fact: each succeeding outburst recorded from the source XTE J1550–564 proves to be less intense than the preceding one (see Fig. 1); at the same time, the

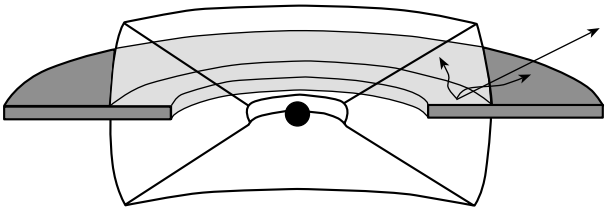

Fig. 4. Schematic view of the central zone around the black hole in XTE J1550–564. The shaded and transparent regions show the optically thick accretion disk and the optically thin hot plasma zone, respectively. The arrow indicates the direction toward the observer.

source's spectrum is becoming harder. It may be assumed that this results from the different physical conditions in the accretion disk near the black hole: at the onset of its activity in 1998, the source was being fed by a massive accretion disk, which remained filled for a long period. However, the disk surface density decreases with each new outburst, the rate of accretion onto the black hole becomes lower, and the outbursts become weaker and harder. This argument leads us to suggest that the next outburst will be even weaker and will occur with a longer delay.

ACKNOWLEDGMENTS

We wish to thank E.M. Churazov, who developed the algorithms for analyzing IBIS data and provided the software and M.R. Gilfanov, who provided the software. This work was supported by the Ministry of Industry and Science (grant no. NSh-2083.2003.2 from the President of Russia) and the Russian Academy of Sciences (the Nonstationary Phenomena in Astronomy program). We are grateful to the INTEGRAL Science Data Centre (Versoix, Switzerland) and the Russian INTEGRAL Science Data Center (Moscow, Russia). The results of this work are based on the observations of the INTEGRAL observatory, a ESA mission with the participation of Denmark, France, Germany, Italy, Spain, Switzerland, the Czech Republic, Poland, Russia, and the United States. We also used data from the High Energy Astrophysics Science Archive Research Center (HEASARC) of the Goddard Space Flight Center.

REFERENCES

1. N. L. Aleksandrovich and V. A. Arefev, Pis'ma Astron. Zh. **28**, 698 (2002) [Astron. Lett. **28**, 660 (2002)].
2. M. Basko, R. Sunyaev, and L. Titarchuk, Astron. Astrophys. **31**, 249 (1974).
3. T. Belloni, A. Colombo, J. Homan, *et al.*, Astron. Astrophys. **390**, 199 (2002).
4. D. Campbell-Wilson, V. McIntyre, R. Hunstead, and A. Green, IAU Circ. **7010** (1998).
5. P. Dubath, M. Revnivtsev, P. Goldoni, *et al.*, IAU Circ. **8100** (2003).
6. N. A. Eismont, A. V. Ditrikh, G. Janin, *et al.*, Astron. Astrophys. **411**, L37 (2003).
7. I. M. George and A. C. Fabian, Mon. Not. R. Astron. Soc. **249**, 352 (1991).
8. D. Hannikainen, D. Campbell-Wilson, R. Hunstead, *et al.*, Astrophys. Space Sci. Suppl. **276**, 45 (2001).
9. J. Homan, R. Wijnands, M. van der Klis, *et al.*, Astrophys. J., Suppl. Ser. **132**, 377 (2001).
10. P. Kaaret, S. Corbel, J. Tomsick, *et al.*, Astrophys. J. **582**, 945 (2003).
11. F. Lebrun, J. Leray, P. Lavocat, *et al.*, Astron. Astrophys. **411**, L141 (2003).
12. T. Maccarone, Astron. Astrophys. **409**, 697 (2003).
13. J. McClintock and R. Remillard, astro-ph/0306213 (2003).
14. F. Meyer, B. F. Liu, and E. Meyer-Hofmeister, Astron. Astrophys. **361**, 175 (2000).
15. J. Miller and J. Homan, Astron. Telegram **135** (2003).
16. J. Orosz, IAU Circ. **7009** (1998).
17. J. Orosz, P. Grott, M. van der Kliss, *et al.*, Astrophys. J. **568**, 845 (2002).
18. Ju. Poutanen, J. Krolik, and F. Ryde, Mon. Not. R. Astron. Soc. **292**, L21 (1997).
19. Ju. Poutanen and R. Svensson, Astrophys. J. **470**, 249 (1996).
20. R. Remillard, E. Morgan, J. McClintock, and G. Sobczak, IAU Circ. **7019** (1998).
21. M. G. Revnivtsev, R. A. Syunyaev, D. A. Varshalovich, *et al.,* Pis'ma Astron. Zh. **30**, 430 (2004) [Astron. Lett. **30**, 382 (2004)].
22. J. Rodriguez, S. Corbel, and J. Tomsick, Astrophys. J. **595**, 1032 (2003).
23. N. I. Shakura and R. A. Sunyaev, Astron. Astrophys. **24**, 337 (1973).
24. D. A. Smith, IAU Circ. **7008** (1998).
25. G. Sobczak, J. McClintock, R. Remillard, *et al.*, Astrophys. J. **544**, 993 (2000).
26. R. Sunyaev and L. Titarchuk, Astron. Astrophys. **86**, 121 (1980).
27. J. Tomsik, S. Corbel, R. Fender, *et al.*, Astrophys. J. **582**, 933 (2003).
28. J. Tomsik, S. Corbel, and P. Kaaret, Astrophys. J. **563**, 229 (2001a).
29. J. Tomsick, E. Smith, J. Swank, *et al.*, IAU Circ. **7575** (2001b).
30. G. Vedrenne, J.-P. Roques, V. Schonfelder, *et al.*, Astron. Astrophys. **411**, L63 (2003).
31. C. Winkler, T. J.-L. Courvoisier, G. Di Cocco, *et al.*, Astron. Astrophys. **411**, L1 (2003a).
32. C. Winkler, N. Gehrels, V. Schonfelder, *et al.*, Astron. Astrophys. **411**, L349 (2003b).

Translated by A. Dambis

Astronomy Letters, Vol. 30, No. 10, 2004, pp. 675–684. Translated from Pis'ma v Astronomicheskiĭ Zhurnal, Vol. 30, No. 10, 2004, pp. 743–753.

A White Dwarf in the State of an Ejector

N. R. Ikhsanov[1,2*], V. V. Neustroev[3], and N. G. Beskrovnaya[1]

[1] *Pulkovo Astronomical Observatory, Russian Academy of Sciences, Pulkovskoe shosse 65, St. Petersburg, 196140 Russia*

[2] *National Astronomical Observatory of Korea, Taejon, South Korea*

[3] *Laboratory of Computational Astrophysics, National University of Ireland, Halvey, Newcastle*

Received March 26, 2004

Abstract—We analyze the possibility of observational identification of white dwarfs in the state of an ejector. Among the distinctive features of this class of objects are a high rate of rotational energy loss comparable to or higher than the observed luminosity of the object and nonthermal gamma-ray and/or radio spectra. The manifestations of the white dwarf in the close binary system AE Aquarii closely match these criteria. We show that most of the peculiar manifestations of this object in the hard spectral range and the observed pattern of mass transfer in the system can be explained in terms of a model in which the state of the white dwarf is classified as an ejector. © *2004 MAIK "Nauka/Interperiodica".*

Key words: *stars—structure and evolution, close binary systems, white dwarfs.*

INTRODUCTION

A compact star with a strong magnetic field can be in one of the following three states: an ejector, a propeller, and an accretor. This classification reflects the different evolutionary stages of compact stars in accordance with the dominant energy release mechanism responsible for their emission (see, Lipunov 1987).

For neutron stars, all three states listed above have a fairly reliable observational confirmation. Ejectors and accretors have been identified with radio (rotation-powered) and accretion-powered pulsars, respectively. Analysis of the X-ray spectra for several Be/X-ray transients allows the state of the neutron star to be identified during the quiescent phase of the source in the state of a propeller (Campana *et al.* 2002; Menou and McClintock 2001).

For white dwarfs, the progress in the observational confirmation of the above classification is more modest. Only the identification of several white dwarfs with accretors, which most of the degenerate components in low-mass close binaries known as cataclysmic variables are (Warner 1995), has been universally accepted.

The manifestations of a white dwarf in the state of an ejector were studied in detail by Usov (1988, 1993) and Paczyński (1990) for the anomalous X-ray pulsar 1E 2259 + 586. In particular, it was pointed out that the model of particle acceleration in the vacuum gap near a stellar surface (Arons and Scharlemann 1979) is fully applicable to white dwarfs whose surface temperature does not exceed 10^6 K (Usov 1988). It should be noted that most of the alternative models that describe the spin-down of rotation-powered pulsars can also be used to model the manifestations of a white dwarf in the state of an ejector. In particular, the models of particle acceleration in the outer gap (Cheng *et al.* 1986) and the model of current dissipation in the magnetosphere (Beskin *et al.* 1993) developed for neutron stars encounter no significant restrictions when applied to white dwarfs. Perhaps the only exception is the model by Muslimov and Tsygan (1992) that associates the origin of the electric potential near the neutron-star surface with general relativity effects, which are negligible for white dwarfs.

The necessary conditions for modeling a white dwarf in the state of an ejector are a strong surface magnetic field and a short spin period. At present, the existence of white dwarfs with strong magnetic fields (up to 10^9 G) is an observationally established fact (Wickramasinghe and Ferrario 2000). On the other hand, several white dwarfs that are members of cataclysmic variables show spin periods of ~30 s (Sion 1999). Thus, the expected rate of rotational energy loss by a hypothetical white dwarf with a dipole magnetic moment of $\mu = 10^{35}\mu_{35}$ G cm^3 and a rotation period of $P = 30P_{30}$ s estimated using the formula for the magnetodipole losses is

$$L_{\rm md} \simeq 5 \times 10^{35}\mu_{35}^2 P_{30}^{-4} \text{ erg s}^{-1}. \quad (1)$$

*E-mail: ikhsanov@kao.re.kr

1063-7737/04/3010-0675$26.00

This value is comparable to the rate of rotational energy loss by neutron stars in the stage of an ejector. In this case, the pressure of the relativistic wind ejected by the white dwarf at the distance of its accretion radius, $p_{\rm rw}(r_{\rm a}) = L_{\rm md}/4\pi c r_{\rm a}^2$, exceeds the ambient gas pressure, $p_{\rm g} = (1/2)\rho_\infty V_{\rm rel}^2$, provided that $\rho_\infty(r \gtrsim r_{\rm a}) < 60 V_7^{-2}$ cm^{-3}. Here, $r_{\rm a} = 2GM_{\rm wd}/V_{\rm rel}^2$ is the accretion radius of the white dwarf with mass $M_{\rm wd}$, $V_{\rm rel}$ is the velocity of the white dwarf relative to the ambient gas ($V_7 = V_{\rm rel}/10^7$ cm s^{-1}), and ρ_∞ is the density of the matter beyond the accretion radius of the compact object. For typical parameters of our problem, this condition is satisfied with a large margin, which allows the state of the white dwarf under consideration to be classified as an ejector.

The ratio of the observed luminosity of an object to the rate of its rotational energy loss should be singled out among the parameters that allow stars in the state of an ejector to be identified. Radio pulsars still remain the only class of astronomical objects for which this ratio is much less than unity (Michel and Li 1999). The rotational energy of these objects transforms into the energy of a relativistic wind and magnetodipole radiation, which manifest themselves outside the detectable part of the electromagnetic spectrum. Therefore, one might expect the corresponding ratio for a white dwarf in the state of an ejector to also be much less than unity.

As Usov (1993) showed, a white dwarf in the state of an ejector can show up as an intense gamma-ray source. The energy of the gamma rays emitted by such a source lies above the energies that correspond to the proton rest mass (1 GeV) and can reach several tens of TeV. Accordingly, the short-wavelength spectrum of such a source will be essentially nonthermal in nature.

Finally, one may expect the X-ray spectrum of a white dwarf in the state of an ejector to differ from the spectra of white dwarfs in the state of an accretor. By analogy with neutron stars (Becker and Trümper 1997), the spectrum of a white dwarf in the state of an ejector may be expected to be softer than the spectra of white dwarfs accreting matter onto their surfaces.

Among the white dwarfs studied to date, only one object corresponds to the listed parameters: the white dwarf in the close binary system AE Aquarii. Analysis of its observational manifestations is the subject of this paper.

OBSERVATIONAL MANIFESTATIONS OF AE AQUARII

The peculiar novalike star AE Aquarii is a noneclipsing close binary system whose components are a red dwarf on or near the main sequence and a white dwarf rotating with a period of $\simeq$33 s. Basic parameters of the binary are given in the table.

The emission from the binary is observed over almost all ranges of the electromagnetic spectrum. In the radio (Bastian *et al.* 1988) and high-energy ($\sim 10^{12}$ eV) gamma-ray (Meintjes *et al.* 1994) ranges, it shows up as a nonthermal variable source. In the remaining parts of the spectrum, the emission from the binary is predominantly thermal and is well fitted by a superposition of three spatially separated sources. The red dwarf makes a major contribution to the binary's emission (90–95%) in the visual spectral range (Bruch 1991). The contribution of the white dwarf shows up most clearly in the optical (Patterson 1979), ultraviolet (UV) (Eracleous *et al.* 1994), and X-ray (Choi *et al.* 1999) ranges as a component modulated with its spin period. The third source is extended and highly variable. It manifests itself as a blue/UV continuum, broad emission lines with single-peaked profiles, and a persistent X-ray component. This source is associated with the matter that is lost by the red dwarf and that interacts with the magnetic field of its degenerate, rapidly rotating companion (Eracleous and Horne 1996). It is probably responsible for the unique flaring activity of the binary: on a time scale of several hours, the UV luminosity of the binary changes by an order of magnitude (Beskrovnaya *et al.* 1996). The corresponding flares show good correlation in the optical, UV, and X-ray ranges (Osborne *et al.* 1995) and do not correlate with radio flares that have a similar time scale (Abada-Simon *et al.* 1995).

AE Aquarii is traditionally classified as a cataclysmic variable and is attributed to the subclass of intermediate polars. The standard approach to the interpretation of this class of objects is based on the model of disk accretion onto a magnetized white dwarf whose spin period is much shorter than the orbital period of the binary (Patterson 1994). The recurrent pulsations and flaring activity of these objects are described in terms of unsteady accretion onto the magnetic poles of the white dwarf.

At present, however, it has been established that the manifestations of AE Aquarii cannot be interpreted in terms of the above model. Analysis of the binary's observations with the Hubble Space Telescope shows that the amplitude of the intensity variations in the emission modulated with the spin period of the white dwarf is relatively low, and the corresponding variations do not correlate with the object's flaring

Parameters of AE Aquarii

Binary parameters	Values	References
Distance	100 ± 30 pc	Welsh *et al.* (1995), Friedjung (1997)
Orbital period	9.88 h	Chincarini and Walker (1981)
Inclination	$50° < i < 70°$	Welsh *et al.* (1995); Reinsch and Beuermann (1994)
Eccentricity	0.02	Chincarini and Walker (1981)
Mass ratio	0.6–0.8	Welsh *et al.* (1995); Reinsch and Beuermann (1994)
Component parameters	Normal	Compact
Type of object	K3V–K5V	White dwarf
Mass, $M_\odot$	$0.41 \sin^{-3} i$	$0.54 \sin^{-3} i$
Spin period	~ 9.88 h	33.08 s
Spin-down rate, s s^{-1}	–	5.64×10^{-14}
Inclination of magnetic axis to rotation axis	–	74°–76°

activity (Eracleous *et al.* 1994). The confirmation of this result by X-ray observations (Clayton and Osborne 1995; Choi *et al.* 1999) suggests that the flaring activity is unrelated to the accretion on the surface of the white dwarf. Moreover, the X-ray spectrum of AE Aquarii is much softer than the typical spectra of intermediate polars, which calls into question its accretion nature.

The Doppler Hα tomogram of AE Aquarii presented by Wynn *et al.* (1997) provides evidence for the absence of an accretion disk in this binary. It should be noted that several other characteristic manifestations of an accretion disk, in particular, a double-peaked emission line profile, is not observed in the binary either.

Finally, analysis of a long (14.5 yr) series of observations led de Jager *et al.* (1994) to conclude that the spin period of the white dwarf increases steadily at a rate of $\dot{P}_0 = 5.64 \times 10^{-14}$ s s^{-1}. A detailed analysis of these data performed by Welsh (1999) indicates that this spin-down in the entire time interval is extremely stable and corresponds to the spin-down of a star whose moment of inertia is comparable in order of magnitude to that of the white dwarf. This allows the rate of rotational energy loss by the white dwarf to be estimated as

$$L_{\rm sd} = 6 \times 10^{33} I_{50} P_{33}^{-3} (\dot{P}/\dot{P}_0)\ {\rm erg\ s^{-1}}, \qquad (2)$$

where I_{50} is the moment of inertia of the white dwarf in units of 10^{50} g cm^2.

The derived value of $L_{\rm sd}$ exceeds the UV and X-ray luminosity of the system by a factor of 120–300 (depending on the flaring/quiescent state of the object). Moreover, it is at least a factor of 5 higher than the bolometric luminosity of the binary. Together with the aforesaid, this suggests that the white dwarf in AE Aquarii is in the state of an ejector.

The Magnetic Field

As was shown previously (Ikhsanov 1998), the observed spin-down of the white dwarf can be interpreted in terms of the canonical ejector model, provided that its dipole magnetic moment is

$$\mu \simeq 1.4 \times 10^{34} P_{33}^2 \left(\frac{L_{\rm sd}}{6 \times 10^{33}\ {\rm erg\ s^{-1}}} \right)^{1/2} {\rm G\ cm^3}. \qquad (3)$$

This corresponds to a surface magnetic field strength on the white dwarf $B(r_{\rm wd}) \approx 50$ MG.

In light of the current views of the magnetic field strengths on white dwarfs, this estimate appears quite realistic (see the Introduction). At the same time, it is more than an order of magnitude larger than the magnetic field strength estimated by Bastian *et al.* (1988) and Stockman *et al.* (1992) using the circular polarization measurements of the optical emission from AE Aquarii and the traditional classification of the object as an intermediate polar. The causes of this discrepancy were considered in detail previously (Ikhsanov *et al.* 2002). In particular, it was pointed out that these magnetic field estimates for AE Aquarii were obtained using the accretion model of this object. However, the contribution of the white dwarf in this model is almost two orders of magnitude larger than the actually observed value (Eracleous *et al.* 1994; Choi *et al.* 1999). Therefore, the magnetic field estimates by Bastian *et al.* (1988) and Stockman *et al.* (1992) prove to be ineffective and, hence, cannot be considered as an argument in the discussion

on the magnetic field strength of the white dwarf in AE Aquarii.

The attempts to estimate the magnetic field of the white dwarf from the traditional classification of AE Aquarii (Stockman *et al.* 1992) are also groundless. The only property of AE Aquarii that it shares with intermediate polars is the nature of the components in these systems: a Roche-lobe-filling red dwarf and a magnetized, rapidly rotating white dwarf. However, the spectroscopic and photometric manifestations of AE Aquarii differ radically from the typical manifestations of intermediate polars, suggesting that the energy release mechanisms responsible for the emission of these objects are different in nature.

The most difficult question in validating estimate (3) is the origin of the rapidly rotating white dwarf with a strong magnetic field. The scenarios suggested to date—(1) the merger of the white dwarf with another white dwarf, a brown dwarf, or a massive planet (Paczyński 1990) and (2) the magnetic field enhancement in a differentially rotating white dwarf (Ikhsanov 1999), are more likely phenomenological and require a more detailed quantitative study. At the same time, the estimates given in these papers show that, during their evolution, white dwarfs can pass through an ejector stage under certain conditions during which their spin periods are close to the minimum possible period ($P_{\min}(M = M_\odot) \sim 9$ s), while the magnetic field strength reaches several tens or hundreds of MG.

To summarize, we may say that there is currently no direct observational or theoretical evidence that the magnetic field of the white dwarf in AE Aquarii is much weaker than 50 MG. Thus, we take the magnetic field estimate (3) as the basis for a further analysis of the properties of the source.

Ejection

Spectroscopic and photometric studies of the 33-s oscillations in the optical and UV wavelength ranges (Eracleous *et al.* 1994) make it possible to estimate the mean surface temperature of the white dwarf, $T_{\rm int} \sim (1{-}1.6) \times 10^4$ K, and to identify two local ($A_{\rm mp} \sim (7{-}40) \times 10^{15}$ cm^2) regions of elevated temperature ($T_{\rm mp} \sim (2{-}5) \times 10^4$ K). The diametrically opposite locations of these regions allow them to be associated with the magnetic poles. As was noted above, there is no evidence of accretion onto the surface of the white dwarf. Thus, the surface temperature of the white dwarf is much lower than the critical value (10^6 K) given by Usov (1988), implying that the model of particle acceleration in the vacuum gap near its magnetic poles is applicable.

Following Arons and Scharlemann (1979), the potential difference in the vacuum gap near the surface of the white dwarf can be estimated as

$$\varphi(r) = \int_{R_{\rm wd}}^{\rm r} E_\parallel ds \simeq 2\sqrt{2} E_\parallel^{\rm AS} R_{\rm wd} \left[\left(\frac{r}{R_{\rm wd}} \right)^{1/2} - 1 \right], \quad (4)$$

where s is the distance measured along the radius from the surface of the white dwarf, $r = R_{\rm wd} + s$, and

$$E_\parallel^{\rm AS} \simeq \frac{1}{8\sqrt{3}} \left(\frac{\omega_{\rm s} R_{\rm wd}}{c} \right)^{5/2} B(R_{\rm wd}). \quad (5)$$

Therefore, the maximum energy of the particles ejected by the white dwarf in the model of AE Aquarii under consideration is

$$E_{\rm p}^{\max} \simeq 2 \times 10^{12} \mu_{34.2} R_{8.8}^{1/2} \left[\left(\frac{r}{R_{\rm wd}} \right)^{1/2} - 1 \right] \text{ eV}. \quad (6)$$

Assuming the linear size of the acceleration region to be of the order of the radius of the white dwarf, we conclude that the maximum energy of the particles ejected by it corresponds to the energies of the high-energy gamma rays detected from AE Aquarii, i.e., on the order of TeV (see Meintjes *et al.* 1994).

An invariable attribute of the models of particle ejection from the region of the magnetic poles of neutron stars (Arons 1981; Beskin *et al.* 1993; Michel 1991) is the reverse current that flows along magnetic field lines toward the stellar surface and closes the electric circuit near the magnetic poles of the ejector. Dissipation of the reverse current near the stellar surface gives rise to regions of elevated temperature localized in the vicinity of its magnetic poles. Adaptation of this approach to the white dwarf under consideration (Ikhsanov 1998) leads us to conclude that the area of the regions of elevated temperature on its surface can be estimated as

$$A_{\rm mp} \sim \frac{1.6\pi R_{\rm wd}^3}{R_{\rm lc}} \simeq 9 \times 10^{15} R_{8.8}^3 P_{33}^{-1} \text{ cm}^2, \quad (7)$$

where $R_{\rm lc} = c/\omega$ is the radius of the light cylinder, and ω is the angular velocity of the white dwarf. This estimate is in good agreement with the observational data (Eracleous *et al.* 1994).

In the approach under consideration, the pulsing X-ray component probably also owes its origin to the nonthermal emission of relativistic particles accelerated in the magnetosphere of the white dwarf. A similar pattern of the X-ray spectrum for the pulsing component and the corresponding spectra for several rotation-powered pulsars that are neutron stars forms the basis for this assertion. In particular, in both cases, the spectrum is much softer than the

typical spectrum of accreting stars (Choi *et al.* 1999), and the ratio of the luminosity of the pulsing X-ray component to the spin-down power of the star is $L_X/L_{sd} \sim 10^{-3}$ (see, Becker and Trümper 1997).

The X-ray emission from the binary will be analyzed in more detail in a subsequent paper. Here, we would like only to note that the origin of the pulsing X-ray component of AE Aquarii in the ejector model does not require the invoking of the theoretically and observationally doubtful assumption of mass accretion onto the surface of the white dwarf (Ikhsanov 2001).

Finally, the observed parameters of the radio emission from the binary strongly suggest that it is of a synchrotron nature (Bastian *et al.* 1988). This interpretation requires the presence of two basic components in the binary: a fairly strong magnetic field and relativistic particles. Both these components are integral attributes of a compact star in the state of an ejector. The absence of a component pulsing with the spin period of the white dwarf in the radio emission from the binary does not come into conflict with the approach under consideration. Here, it should be noted that the typical ratio of the luminosity of the pulsing radio component to the rate of rotational energy loss for neutron stars lies within the range 10^{-7}–10^{-9} (Michel 1991). If this ratio for the white dwarf is of the same order of magnitude, then the expected intensity of its pulsing radio component is within 10^{24}–10^{26} erg s^{-1}. At the same time, the luminosity of the observed (persistent) component is $\sim 10^{29}$ erg s^{-1} (Bastian *et al.* 1988). As a result, it proves to be virtually impossible to separate the pulsing component of the radio emission from AE Aquarii using currently available detectors.

Mass Transfer

One of the key aspects of interpreting AE Aquarii is to analyze the interaction of the white dwarf with the matter lost by the normal component. As we noted above, the result of this interaction is the presence of an extended source in the system whose contribution to the binary's emission dominates in the UV and X-ray spectral ranges and clearly shows up in the optical and UV ranges as emission lines.

The radial velocities of emission lines undergo oscillations with the orbital period of the binary that are out of phase with the corresponding oscillations of absorption lines in the normal component (Reinsch and Beuermann 1994). This allows the emission source to be localized within the Roche lobe of the white dwarf. Analysis of the widths of the observed emission line profiles makes it possible to limit the mean velocity of the emitting matter as $V_{em} \lesssim 500$ km s^{-1} (Welsh *et al.* 1998). Approximating the velocity of the matter within the Roche lobe of the white dwarf (far enough from the Lagrangian point $L1$) by the Keplerian velocity, we conclude that the bulk of the matter responsible for the observed emission is located near the white dwarf at a distance $r_0 \gtrsim GM_{wd}/V_{em}^2 \simeq 4 \times 10^{10}$ cm. Finally, using the luminosity of the emission source $L_{em} \simeq 10^{31}$ erg s^{-1} estimated by Eracleous and Horne (1996) and setting this parameter equal to the rate of gravitational energy release at distance r_0, we obtain a lower limit for the mass transfer rate in the binary: $\dot{M} > 4 \times 10^{15} L_{31} R_{10.6} M_{0.8}^{-1}$ g s^{-1}.

This estimate is an absolute lower limit, and, as we show below, it is an order of magnitude lower than the actual transfer rate in the binary. At the same time, this result plays an important role in identifying the mass transfer mechanism. Indeed, the derived lower limit is more than three orders of magnitude higher than the maximum possible rate of mass capture by the white dwarf from the wind of its normal companion (Ikhsanov 1997). This implies that the normal component in AE Aquarii fills its Roche lobe and loses matter in the form of a stream that flows into the Roche lobe of the white dwarf through the inner Lagrangian point $L1$.

However, the fate of the matter in the Roche lobe of the white dwarf appears more than atypical for the mass transfer in close binary systems. On the one hand, this matter is not accreted by the white dwarf (as suggested by the observed luminosity and X-ray spectrum of the binary). On the other hand, it is not accumulated around the magnetosphere of the white dwarf in the form of a disk (as evidenced by the observed emission line profiles and the structure of the Doppler Hα tomogram). It remains only to assume that the rate of increase in the angular momentum of the stream during its interaction with the magnetic field of the white dwarf is high enough for the entire inflowing matter to leave the system without the formation of an accretion disk.

To check whether this assumption is realistic, we numerically simulated the trajectories of the matter in the Roche lobe of the white dwarf. In our simulations, we used an approach proposed by Wynn and King (1995) according to which the interaction between the magnetic field and the diamagnetic stream moving through it is attributable to magnetic friction. The validity condition for this approach is stream inhomogeneity, i.e., the possibility of its simulation as a set of diamagnetic blobs. The blob radius l_b and density ρ_b are assumed to be close to the radius of the cross section and the density of a homogeneous stream, respectively. In this case, the force of friction

between the field and a blob leads to the acceleration of the latter, which can be estimated as follows:

$$g_{\rm mag} = -k[V_{\rm b} - V_{\rm f}]_{\perp}, \qquad (8)$$

where $V_{\rm b}$ and $V_{\rm f}$ are the velocities of the blob and the magnetic field, respectively; the subscript $\perp$ denotes the velocity component perpendicular to the magnetic field lines at the point of interaction; $k \sim B^2/c_{\rm A}\rho_{\rm b}l_{\rm b}$ is the coefficient of friction between the blobs and the magnetic field; and $c_{\rm A}$ is the Alfvén speed calculated in the space between the blobs. (In our case, it is of the order of the speed of light.)

As was shown by Wynn and King (1995), the coefficient of friction can be represented as $k \sim k_0(r/r_0)^{-n}$, where k_0 and n are constants, and r_0 is the radius of the closest approach of the stream and the white dwarf. In the model under consideration, this radius is limited by the Alfvén radius of the white dwarf:

$$r_0 \gtrsim R_{\rm A} \simeq 3 \times 10^{10}\eta_{0.37}\mu_{34.2}^{4/7}\dot{M}_{17}^{-2/7}M_{0.9}^{-1/7}\ {\rm cm}, \qquad (9)$$

where $\eta_{0.37} = \eta/0.37$ is a parameter that allows for the geometry of the accretion flow normalized as prescribed by Hameury *et al.* (1986). Note that the satisfaction of condition (9) naturally excludes the possibility of an accretion disk being formed in AE Aquarii, because r_0 exceeds the circularization radius (for the parameters of AE Aquarii, $R_{\rm circ} \simeq 2.5 \times 10^{10}$ cm).

Thus, in our computations, we simulated the following pattern of mass transfer. A plasma stream flows into the Roche lobe through the inner Lagrangian point with a thermal velocity (initial condition). Subsequently, its motion to the point of disintegration into blobs is described by a ballistic trajectory. After the point of disintegration, the blob trajectories deviate from the ballistic trajectory due to magnetic friction.

We considered two alternative locations of the point of disintegration. In the first case (I), we assumed, following Wynn and King (1995), that the point of disintegration lies near the Lagrangian point $L1$. In the second case (II), we assumed that the point of disintegration lies near the Alfvén radius of the white dwarf. In this case, the trajectory of the stream up to the point of disintegration was assumed to be ballistic, and magnetic friction switched on only in a region where the pressure of the inflowing gas and the magnetic pressure of the white dwarf became equal in order of magnitude.

In our view, the second approach is more realistic, because it allows the causes of the stream disintegration into blobs to be considered in terms of its interaction with the magnetic field of the white dwarf. In the first case, this scenario is inapplicable, because the magnetic energy density of the white dwarf near point $L1$ is negligible compared to the plasma energy density in the stream. At the same time, we turned to the simulations of both cases in order to understand how strong the dependence of the accretion pattern on the position of the point of stream disintegration is.

In our calculations, we used the following basic parameters of the binary: the component mass ratio $q = 0.64$, the binary's orbital period $P_{\rm orb} = 9.9$ h, the orbital inclination $i = 55^\circ$, and the mass, dipole magnetic moment, and spin period of the white dwarf $M_{\rm wd} = 0.9M_\odot$, $\mu = 1.4 \times 10^{34}$ G cm^3, and $P_{\rm s} = 33$ s, respectively. Following Wynn and King (1995), we assumed that $n = 2$ and normalized the basic parameters of the blobs as $\rho_{\rm b}(r_0) = 10^{-11}\rho_{-11}$ g cm^{-3} and $l_{\rm b}(r_0) = 10^9 l_9$ cm. This allows the parameter k_0 to be expressed as

$$k_0 \simeq 3.3 \times 10^{-9}B^2(r_0)\,\rho_{-11}^{-1}l_9^{-1}{\rm s}^{-1}. \qquad (10)$$

The computed trajectories for the above parameters are shown in Figs. 1 (case I) and 2 (case II). The Roche lobes of the white dwarf and its normal companion are shown. The calculations were performed for three different mass transfer rates in the binary: 10^{16}, 5×10^{16}, and 10^{17} g s^{-1}. The trajectories of blobs with different masses are shown in each of these three cases (the trajectories of the heaviest and lightest blobs are represented by lines *1* and *3*, respectively). The region where the trajectories of the blobs with different masses that leave the binary intersect is hatched.

Figures 1d and 2d show the pattern of mass transfer averaged over the binary's orbital period with a uniform distribution of the mass transfer rate between 10^{16} and 10^{17} g s^{-1}, which, to a first approximation, may be considered to be a superposition of the computational results presented in Figs. 1a–1c and 2a–2c with an equal weight. This result allow us to reach conclusions regarding the structure of the expected Doppler Hα tomogram for AE Aquarii.

To determine the structure of the expected tomogram, we used the results presented in Fig. 2d. We assumed that the Hα emission source was: (1) the matter that is located in the Roche lobe of the white dwarf and that actively interacts with its magnetic field, (2) the region where the trajectories of the blobs with different masses intersect, and (3) the matter that was ejected from the binary and that interacts with the relativistic wind from the white dwarf. With regard to item (3), it should be noted that the matter leaving the binary in the form of a stream produces a disklike envelope that surrounds the binary at a distance $R_{\rm cbe} \gtrsim P_{\rm orb}V_{\rm pl\infty} \sim 4 \times 10^{11}P_{9.9}V_7$ cm, where $V_{\rm pl\infty}$ is the radial velocity of the ejected stream at a distance that is much larger than the size of the binary system. Our numerical calculations indicate that

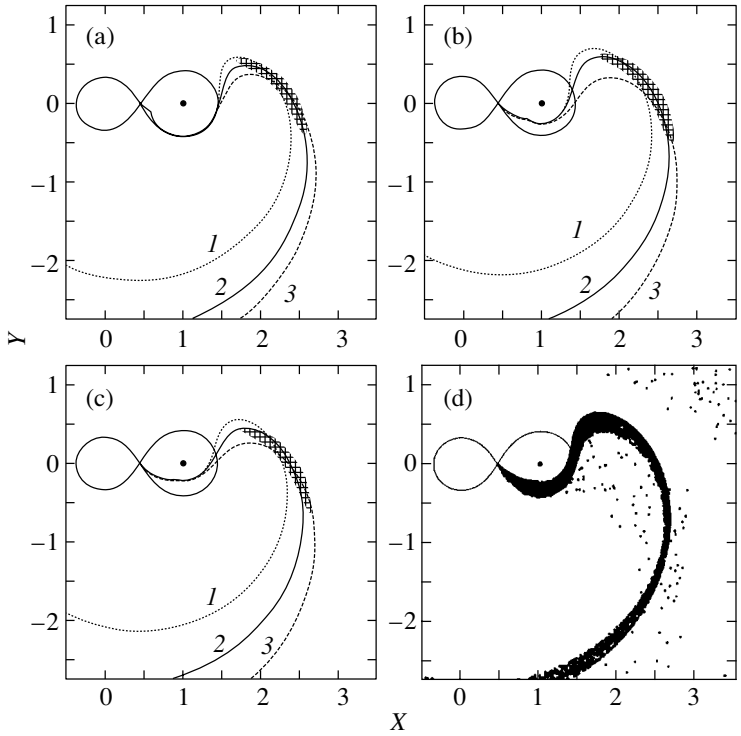

Fig. 1. Trajectories of the stream in coordinate space computed for the following mass loss rates in the binary: (a) 10^{16}, (b) 5×10^{16}, and (c) 10^{17} g s^{-1}. The distance to the point of stream disintegration into blobs is assumed to be $r \gg r_0$. The unit scale along both axes corresponds to the separation between the binary components. The position of the white dwarf is marked by a dot. Lines *1*, *2*, and *3* correspond to the trajectories of blobs with different masses. The region where the blob trajectories intersect is hatched. (d) The pattern of mass transfer averaged over the orbital period.

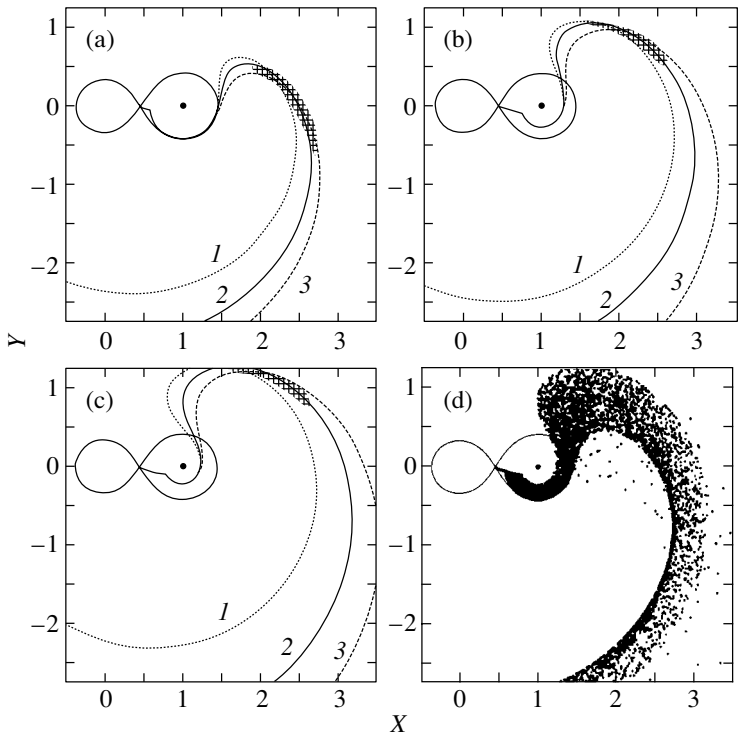

Fig. 2. Trajectories of the stream in coordinate space computed by assuming that the region of stream disintegration lies near the Alfvén surface of the white dwarf. The parameters and the notation are the same as those in Fig. 1.

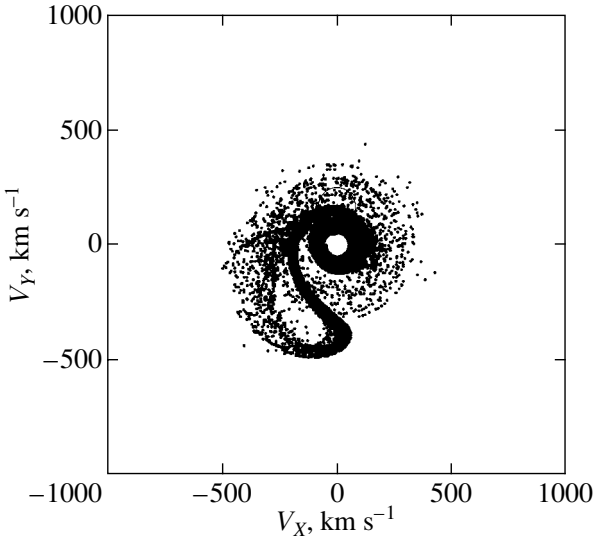

Fig. 3. Expected structure of the Doppler Hα tomogram in the ejector model of AE Aquarii.

$V_{\mathrm{pl}\infty}$ lies within the range $(1-2) \times 10^7$ cm s^{-1}. The cause of the envelope formation is as follows. According to the computational results presented in Figs. 1 and 2, the stream of matter leaves the binary at phase 0.50–0.75 (the phase is measured in the coordinate system centered on the white dwarf counterclockwise from the ray that connects the binary components) and recedes with deceleration, forming a spiral around the binary. However, the position angle of the ejected stream periodically varies due to the orbital rotation. Therefore, the structure of the matter ejected from the binary at distance R_{cbe} will be axisymmetric. Since the radial velocity of the ejected plasma is much higher than its thermal velocity, the expected size of the envelope in a direction perpendicular to the plane of the binary will be much smaller than its radius, which corresponds to a disk-type geometry.

At distance R_{cbe}, the area of the inner boundary of the disklike envelope will be $\sim$0.5% of the area of the sphere of the corresponding radius. This allows the rate of absorption of the relativistic-wind energy by the envelope matter to be estimated, $\lesssim 0.005 L_{\mathrm{sd}} \sim 3 \times 10^{31}$ erg s^{-1}. Assuming that at least half of this energy will be released in the form of radiation, we conclude that the contribution of the envelope is comparable in order of magnitude to the total energy of the emission source in AE Aquarii. Consequently, it would be improper to ignore this additional source.

The pattern of mass transfer in AE Aquarii presented in Fig. 2d is shown in velocity space in Fig. 3. The tomogram of the object obtained in this way shows the closest similarity to the observed tomogram (see, e.g., Welsh *et al.* 1998), provided that the mean mass transfer rate in the binary on the scale of its orbital period is $\langle \dot{M} \rangle = 5 \times 10^{16}$ g s^{-1} and the parameter $k_0 = 4.8 \times 10^{-7}$ s^{-1}. Under these conditions, the minimum distance to which the stream approaches the white dwarf is $\bar{r}_0 \approx 5 \times 10^{10}$ cm. Accordingly, the rate of its gravitational energy release near the point of the closest approach is $\bar{L}_{\mathrm{st}} \simeq 10^{32}$ erg s^{-1}, which corresponds in order of magnitude to the luminosity of the extended source observed in the binary.

CONCLUSIONS

The interpretation of the rapid spin-down of the white dwarf in AE Aquarii in terms of the canonical ejector model is based on the assumption that its magnetic moment $\mu \gtrsim 10^{34}$ G cm^3. This assumption does not contradict any of the currently known properties of the binary. At the same time, using this assumption alone proves to be sufficient to satisfactorily explain the manifestations of AE Aquarii in the short-wavelength range and to interpret the pattern of mass transfer constructed from the observed properties of emission lines. The origin of the white dwarf with its rapid rotation and strong magnetic field remains the most difficult question in substantiating the ejector model of AE Aquarii. This problem can be solved in terms of the model of a merger of the white dwarf with its low-mass ($\sim 0.03 M_\odot$) companion or by invoking the model of magnetic field enhancement in a differentially rotating white dwarf.

This object is unique because of its comparatively small distance from the Earth ($\simeq$100 pc) and its relatively short lifetime in the state of an ejector ($\sim 10^7$ yr). The possibility of identifying an object similar to AE Aquarii and located at a distance that exceeds 100 pc severalfold is unlikely at the current detector sensitivity threshold.

Among the advantages of the ejector model for AE Aquarii are the relatively small number of basic assumptions and their agreement with observational data, which distinguishes the presented model from alternative interpretations of this object. In particular, a necessary condition for the applicability of a magnetohydrodynamic propeller (Meintjes and de Jager 2000) is the presence of an inhomogeneous accretion disk in the binary, which is not confirmed by spectroscopic observations. On the other hand, one of the attempts to explain the rapid spin-down of the white dwarf due to the emission of gravitational waves by it (Choi and Yi 2000) is based on the definitely unrealistic assumption about the distribution of matter on the surface of the white dwarf (Ikhsanov and Beskrovnaya 2002). The list of assumptions made in the magnetic propeller model (Wynn *et al.* 1997;

Welsh *et al.* 1998) currently contains at least seven items:

(1) The magnetic moment of the white dwarf is assumed (based on the classification of the binary as an intermediate polar) to be $\sim 10^{32}$ G cm^3.

(2) The spin-down of the white dwarf is interpreted in terms of the propeller mechanism, which requires that the mass loss rate in the binary be assumed to be $\gtrsim 10^{18}$ g s^{-1} (Choi and Yi 2000).

(3) The plasma stream flowing into the Roche lobe of the white dwarf is initially assumed to be highly inhomogeneous, i.e., 99.99% of its mass is contained in blobs (otherwise, the formation of a disk by a homogeneous component is inevitable).

(4) It is assumed that during the interaction of blobs with the magnetic field, their internal energy (and, accordingly, the temperature) does not change, and the entire spin-down energy of the white dwarf transforms into the kinetic energy of the blobs (otherwise, the theoretical tomogram would differ greatly from the one observed).

(5) The emission source is located outside the binary in the region where the trajectories of the blobs with different masses intersect.

(6) The cooling rate of the blobs is much lower than the cooling rate attributable to the radiative losses (otherwise, the significant contribution of the emission from the matter with velocities $\sim$100 km s^{-1} to the observed tomogram could not be explained in terms of the magnetic propeller model).

(7) It is assumed that 99.9% of the matter leaves the binary through the propeller effect, but at the same time, 0.1% of the inflowing matter is accreted onto the surface of the white dwarf (otherwise, the origin of the pulsing X-ray component could not be explained in terms of this approach).

It should be noted that none of the above assumptions is required when the binary is interpreted in terms of the ejector model. In light of this, the approach presented here seems promising for further studies of AE Aquarii.

ACKNOWLEDGMENTS

This work was supported by the Russian Foundation for Basic Research (project no. 03-02-17223a) and the Astronomy Federal program.

REFERENCES

1. M. Abada-Simon, T. S. Bastian, K. Horne, *et al.*, ASP Conf. Ser. **85**, 355 (1995).
2. J. Arons, Astrophys. J. **248**, 1099 (1981).
3. J. Arons and E. T. Scharlemann, Astrophys. J. **231**, 854 (1979).
4. T. S. Bastian, G. A. Dulk, and G. Chanmugam, Astrophys. J. **324**, 431 (1988).
5. W. Becker and J. Trümper, Astron. Astrophys. **326**, 682 (1997).
6. V. S. Beskin, A. F. Gurevich, and Ya. N. Istomin, *Physics of Pulsar Magnetosphere* (Cambridge Univ. Press, Cambridge, 1993).
7. N. G. Beskrovnaya, N. R. Ikhsanov, A. Bruch, and N. M. Shakhovskoy, Astron. Astrophys. **307**, 840 (1996).
8. A. Bruch, Astron. Astrophys. **251**, 59 (1991).
9. S. Campana, L. Stella, G. L. Israel, *et al.*, Astrophys. J. **580**, 389 (2002).
10. K. S. Cheng, C. Ho, and M. Ruderman, Astrophys. J. **300**, 500 (1986).
11. G. Chincarini and M. F. Walker, Astron. Astrophys. **104**, 24 (1981).
12. C.-S. Choi, T. Dotani, and P. C. Agrawal, Astrophys. J. **525**, 399 (1999).
13. C.-S. Choi and I. Yi, Astrophys. J. **538**, 862 (2000).
14. K. L. Clayton and J. P. Osborne, ASP Conf. Ser. **85**, 379 (1995).
15. O. C. de Jager, P. J. Meintjes, D. O'Donoghue, and E. L. Robinson, Mon. Not. R. Astron. Soc. **267**, 577 (1994).
16. M. Eracleous and K. Horne, Astrophys. J. **471**, 427 (1996).
17. M. Eracleous, K. Horne, E. L. Robinson, *et al.*, Astrophys. J. **433**, 313 (1994).
18. M. Friedjung, New Astron. **2**, 319 (1997).
19. J.-M. Hameury, A. R. King, and J.-P. Lasota, Mon. Not. R. Astron. Soc. **218**, 695 (1986).
20. N. R. Ikhsanov, Astron. Astrophys. **325**, 1045 (1997).
21. N. R. Ikhsanov, Astron. Astrophys. **338**, 521 (1998).
22. N. R. Ikhsanov, Astron. Astrophys. **347**, 915 (1999).
23. N. R. Ikhsanov, Astron. Astrophys. **374**, 1030 (2001).
24. N. R. Ikhsanov and N. G. Beskrovnaya, Astrophys. J. **576**, L57 (2002).
25. N. R. Ikhsanov, S. Jordan, and N. G. Beskrovnaya, Astron. Astrophys. **335**, 152 (2002).
26. V. M. Lipunov, *Astrophysics of Neutron Stars* (Nauka, Moscow, 1987) [in Russian].
27. P. J. Meintjes and O. C. de Jager, Mon. Not. R. Astron. Soc. **311**, 611 (2000).
28. P. J. Meintjes, O. C. de Jager, B. C. Raubenheimer, *et al.*, Astrophys. J. **434**, 292 (1994).
29. K. Menou and J. E. McClintock, Astrophys. J. **557**, 304 (2001).
30. F. C. Michel, *Theory of Neutron Star Magnetospheres* (Chicago Press, Chicago, 1991).
31. F. C. Michel and H. Li, Phys. Rep. **318**, 227 (1999).
32. A. G. Muslimov and A. I. Tsygan, Mon. Not. R. Astron. Soc. **255**, 61 (1992).
33. J. P. Osborne, K. L. Clayton, D. O'Donoghue, *et al.*, ASP Conf. Ser. **85**, 368 (1995).

34. B. Paczyński, Astrophys. J. **365**, L9 (1990).
35. J. Patterson, Astrophys. J. **234**, 978 (1979).
36. J. Patterson, Publ. Astron. Soc. Pac. **106**, 209 (1994).
37. K. Reinsch and K. Beuermann, Astron. Astrophys. **282**, 493 (1994).
38. E. M. Sion, Publ. Astron. Soc. Pac. **111**, 532 (1999).
39. H. S. Stockman, G. D. Schmidt, G. Berriman, *et al.*, Astrophys. J. **401**, 628 (1992).
40. V. V. Usov, Pis'ma Astron. Zh. **14**, 606 (1988) [Sov. Astron. Lett. **14**, 258 (1988)].
41. V. V. Usov, Astrophys. J. **410**, 761 (1993).
42. B. Warner, *Cataclysmic Variable Stars* (Cambridge Univ. Press, Cambridge, 1995).
43. W. F. Welsh, ASP Conf. Ser. **157**, 357 (1999).
44. W. F. Welsh, K. Horne, and R. Gomer, Mon. Not. R. Astron. Soc. **275**, 649 (1995).
45. W. F. Welsh, K. Horne, and R. Gomer, Mon. Not. R. Astron. Soc. **298**, 285 (1998).
46. D. T. Wickramasinghe and L. Ferrario, Publ. Astron. Soc. Pac. **112**, 873 (2000).
47. G. A. Wynn and A. R. King, Mon. Not. R. Astron. Soc. **275**, 9 (1995).
48. G. A. Wynn, A. R. King, and K. Horne, Mon. Not. R. Astron. Soc. **286**, 436 (1997).

Translated by V. Astakhov

Astronomy Letters, Vol. 30, No. 10, 2004, pp. 685–693. Translated from Pis'ma v Astronomicheskiĭ Zhurnal, Vol. 30, No. 10, 2004, pp. 754–763.

Weakly Radiating Radio Pulsars

V. S. Beskin[1]* and E. E. Nokhrina[2]

[1] *Lebedev Institute of Physics, Russian Academy of Sciences, Leninskiĭ pr. 53, Moscow, 119991 Russia*

[2] *Moscow Institute of Physics and Technology, Institutskiĭ per. 9, Dolgoprudnyĭ, Moscow oblast, 141700 Russia*

Received January 30, 2004

Abstract—We analyze the statistical distribution of weakly radiating pulsars, i.e., radio pulsars that have passed to the stage of an orthogonal rotator during the evolution of the inclination angle χ. We discuss in detail the factors that lead to a significant reduction in the energy losses for this class of objects. We have determined the number of weakly radiating radio pulsars and their distribution in spin period P. The predictions of a theory based on the model of current losses are shown to be consistent with observational data. © *2004 MAIK "Nauka/Interperiodica".*

Key words: *pulsars, neutron stars, and black holes; radio pulsars.*

INTRODUCTION

At present, it seems to have been proven that the spindown of radio pulsars is entirely determined by the longitudinal electric currents flowing in the neutron-star magnetosphere (Beskin *et al.* 1984, 1993; Mestel *et al.* 1999; Mestel 1999). In this case, an invariant of the motion is the quantity

$$I = \frac{\sin\chi}{P}, \qquad (1)$$

so the angle χ between the magnetic moment of the pulsar and its spin axis must tend to 90° as the spin period P increases.

Here, one important remark should be immediately made. Observations reveal an unquestionable decrease in the mean inclination angles χ (i.e., the values of χ averaged over the corresponding sample of pulsars) with increasing pulsar period P and with decreasing derivative of the period $\dot{P}$ (Malov 1990; Tauris and Manchester 1999). Therefore, the mean angle of axial inclination decreases with increasing dynamical age of pulsars $\tau_{\rm D} = P/\dot{P}$. However, this by no means proves that the angle of inclination for each individual pulsar must decrease. Such behavior of the mean angle of axial inclination χ can also take place if the angle χ for each pulsar increases with time.

Indeed, as Fig. 1 shows, the particle generation at given pulsar period P and magnetic field B will be suppressed exactly at angles χ close to 90°. This is because the Goldreich charge density,

$$\rho_{\rm GJ} \approx -\frac{\mathbf{\Omega B}}{2\pi c}, \qquad (2)$$

near the magnetic poles decreases significantly at such angles, which, in turn, causes the drop in electric potential near the neutron-star surface to decrease. As a result, a stable generation of secondary particles becomes impossible. Therefore, due to this χ dependence of the pulsar death line, the mean angle of axial inclination may decrease with increasing dynamical age, for example, for a uniform distribution of pulsars in the $P-\sin\chi$ plane. Our previous detailed analysis based on the kinetic equation describing the statistical distribution of neutron stars confirmed that the observed distribution of pulsars in axial inclination is consistent with the hypothesis that the angle χ increases for each individual pulsar.

Clearly, if the angle of axial inclination χ actually evolves toward $\chi \approx 90°$, then there must be a certain number of rapidly rotating neutron stars at the stage of an orthogonal rotator for which the condition for the generation of a secondary electron–positron plasma is satisfied. Such radio pulsars, whose existence was predicted by Beskin *et al.* (1984), must have the following properties:

(1) Fast ($P \sim 0.3$ s) or ultrafast ($P < 0.1$ s) rotation;

(2) Reduced spindown rate ($\dot{P} \sim 10^{-17}-10^{-19}$);

(3) Weak radio emission ($L_{\rm rad} \sim 10^{25}-10^{27}$ erg s^{-1});

(4) The presence of an interpulse.

In Fig. 1, the region where such pulsars are located is hatched.

We emphasize that this prediction does not pertain to the millisecond radio pulsars that have long been in binary systems and that have been spun up to periods

*E-mail: beskin@lpi.ru

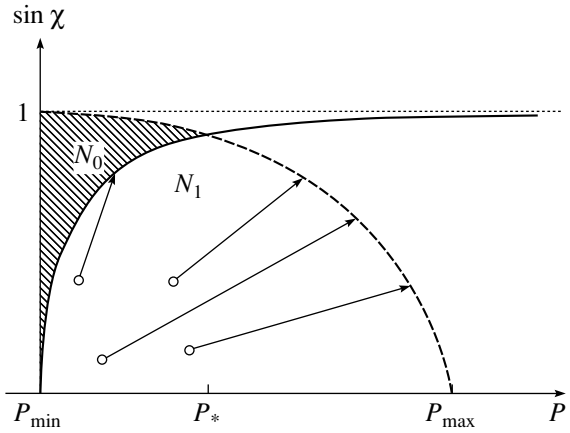

Fig. 1. The line of passage into the region of an orthogonal rotator (26) (solid) and the pulsar death line (28) (dashed) in the $P-\sin\chi$ diagram for magnetic fields of $B_0 = 10^{12}$ G. The evolution of individual pulsars is indicated by the arrows.

$P \sim 1-10$ ms via accretion from the companion star (Lipunov 1987).

Note that twenty years ago, when this prediction was made, and ten years ago, when this result was included in our monograph (Beskin *et al.* 1993), the number of weakly radiating radio pulsars was too small to be able to consistently compare theoretical predictions with observational data. Therefore, we then restricted our analysis to a general formulation of the properties of this class of objects. At present, when the total number of observable radio pulsars has reached 1300 (Manchester 2003) and the theory can be compared with observations, it has become necessary to study the statistical distribution of weakly radiating pulsars in more detail.

On the other hand, the energy losses by neutron stars at the stage of an orthogonal rotator also required a more detailed analysis. The point is that a simple consideration based on an analysis of only the longitudinal current leads to the reducing factor $(\Omega R/c)^{1/2}$ ($\Omega = 2\pi/P$ is the angular velocity of the neutron star, and R is its radius) compared to the current losses of a coaxial rotation (Mestel *et al.* 1999). Indeed, the energy losses can be estimated using the Poynting vector flux through the surface of the light cylinder $R_{\rm L} = c/\Omega$:

$$W_{\rm tot} = \frac{c}{4\pi}\int [\mathbf{E}\times\mathbf{B}]d\mathbf{S} \sim cE(R_{\rm L})B_\varphi(R_{\rm L})R_{\rm L}^2. \quad (3)$$

Here, the electric field near the light cylinder $E(R_{\rm L})$ is determined only by the poloidal magnetic field $B_{\rm p}$:

$$E(R_{\rm L}) \approx \left(\frac{\Omega R_{\rm L}}{c}\right) B_{\rm p} \approx B_{\rm p}; \quad (4)$$

due to the dipolar field fall-off within the light cylinder, $B_{\rm p}(R_{\rm L}) \approx (\Omega R/c)^3 B_0$, where B_0 is the surface magnetic field of the neutron star. In contrast, the toroidal magnetic field B_φ is directly related to the longitudinal current flowing in the magnetosphere. Therefore, for an oblique rotator where the charge density within the polar cap, $R_0 \sim (\Omega R/c)^{1/2}R$, is, on average, a factor of $(\Omega R/c)^{1/2}$ lower than that for a coaxial rotator, the toroidal magnetic field at the light cylinder can be estimated as

$$B_\varphi(R_{\rm L}) \approx \left(\frac{\Omega R}{c}\right)^{1/2} B_{\rm p}(R_{\rm L}). \quad (5)$$

This leads to the additional factor $(\Omega R/c)^{1/2}$ in the expression for the loss power. However, a more detailed analysis shows (Beskin *et al.* 1993) that the reducing factor must actually be $(\Omega R/c)$, so the total losses for an orthogonal rotator should be written as

$$W_{\rm tot} \approx \frac{B_0^2\Omega^4 R^6}{c^3}\left(\frac{\Omega R}{c}\right). \quad (6)$$

Clarifying this contradiction is also the subject of our analysis here.

Thus, our main goal is to refine the spindown law for neutron stars at the stage of an orthogonal rotator and to determine the statistical properties of weakly radiating pulsars. We will show that a consistent allowance for the surface currents flowing along the separatrix between the regions of closed and open field lines actually leads to a significant ($\sim (\Omega R/c)$) reduction in the energy losses for an orthogonal rotator. Next, by analyzing the kinetic equation that describes the evolution of such neutron stars, we will find the period and magnetic-field distribution functions that make it possible to study in detail their statistical properties. We will show that both the total number of weakly radiating pulsars and their distribution in period P are generally in good agreement with observations.

THE ELECTRODYNAMICS OF AN ORTHOGONAL ROTATOR

As was emphasized above, before analyzing the statistical distribution of weakly radiating pulsars in detail, it is necessary to consider in more detail the spindown dynamics of neutron stars at the stage of an orthogonal rotator. For this purpose, we need to repeat several results that were formulated previously in our monograph (Beskin *et al.* 1993).

Radio pulsars are known to spin down under the ponderomotive action of the Ampère force $\mathbf{F}_{\rm A} = \mathbf{J}_{\rm s}\times\mathbf{B}/c$ attributable to the currents $\mathbf{J}_{\rm s}$ that flow over the neutron-star surface. These surface currents close

the longitudinal current flowing in the pulsar magnetosphere. In the presence of a strong magnetic field, the surface current $\mathbf{J}_\mathrm{s}$ can be separated into two components, parallel and perpendicular to the surface electric field $\mathbf{E}_\mathrm{s}$:

$$\mathbf{J}_s^{(1)} = \Sigma_{||}\mathbf{E}_s, \tag{7}$$

$$\mathbf{J}_s^{(2)} = \Sigma_\perp \left[\frac{\mathbf{B}_\mathrm{n}}{B_\mathrm{n}} \times \mathbf{E}_s\right], \tag{8}$$

$$\mathbf{J}_s = \mathbf{J}_s^{(1)} + \mathbf{J}_s^{(2)}, \tag{9}$$

where $\Sigma_{||}$ and $\Sigma_\perp$ are the Pedersen and Hall conductivities, respectively.

Let us assume that the pulsar surface conductivity is uniform and that the electric field $\mathbf{E}_s$ has a potential $\Phi_\mathrm{e} = -\xi'/\Sigma_{||}$. Relations (7) and (8) can then be rewritten as

$$\mathbf{J}_s^{(1)} = \nabla\xi',$$

$$\mathbf{J}_s^{(2)} = \frac{\Sigma_\perp}{\Sigma_{||}}\left[\frac{\mathbf{B}_\mathrm{n}}{B_\mathrm{n}} \times \nabla\xi'\right].$$

Using the continuity equation $\mathrm{div}\mathbf{J}_s = -\partial\rho_\mathrm{e}/\partial t$ and taking into account the fact that $\partial\rho_\mathrm{e}/\partial t$ is equal to the bulk longitudinal current $i_{||}B_0$ flowing in the region of open field lines, we obtain

$$\nabla^2\xi' = -i_{||}B_0.$$

Making the change $x = \sin\theta_\mathrm{m}$ in this equation and introducing the dimensionless potential $\xi = 4\pi\xi'/B_0R^2\Omega$ and current $i_0 = -4\pi i_{||}/\Omega R^2$ ultimately yields

$$\left(1-x^2\right)\frac{\partial^2\xi}{\partial x^2} + \frac{1-2x^2}{x}\frac{\partial\xi}{\partial x} + \frac{1}{x^2}\frac{\partial^2\xi}{\partial\varphi_\mathrm{m}^2} = i_0(x,\varphi_\mathrm{m}), \tag{10}$$

where θ_m and φ_m are the polar and azimuth angles relative to the magnetic dipole axis, respectively, and the normalization of $i_{||}$ will become clearer below. Naturally, the solution of Eq. (10) depends significantly on the boundary condition. As we show below, the assumption that there are no surface currents related to the bulk longitudinal current flowing in the magnetosphere must be this boundary condition. In this case, the boundary condition can be written as

$$\xi[x_0(\varphi_\mathrm{m}),\varphi_\mathrm{m}] = \mathrm{const}, \tag{11}$$

where $x_0(\varphi_\mathrm{m})$ is the boundary of the polar cap.

We emphasize that the main uncertainty is contained here. Indeed, the absence of a longitudinal current in the region of closed field lines $x > x_0$, i.e., the satisfaction of the condition $i_0(x,\varphi_m)|_{x>x_0} = 0$, by no means implies that the gradient in potential ξ (and, hence, the surface current $\mathbf{J}_\mathrm{s}$) is also equal to zero here. For an oblique rotator, the longitudinal current can also be closed outside the polar cap where the equation for the potential ξ is $\nabla^2\xi = 0$. The set of multipole flows $\xi = A_n\cos^n\varphi_\mathrm{m}/x^n$, whose amplitude A_n can be arbitrary, is known to be the solution of this equation. At the same time, the corresponding jump in the derivative of ξ will fix the surface current flowing along the separatrix between the regions of closed and open field lines (see Fig. 2). In other words, this implies that, apart from the bulk current flowing in the region of open field lines, additional surface currents must flow in the magnetosphere along the separatrix surfaces. In this case, their value, at first glance, may not be related in any way to the bulk current.

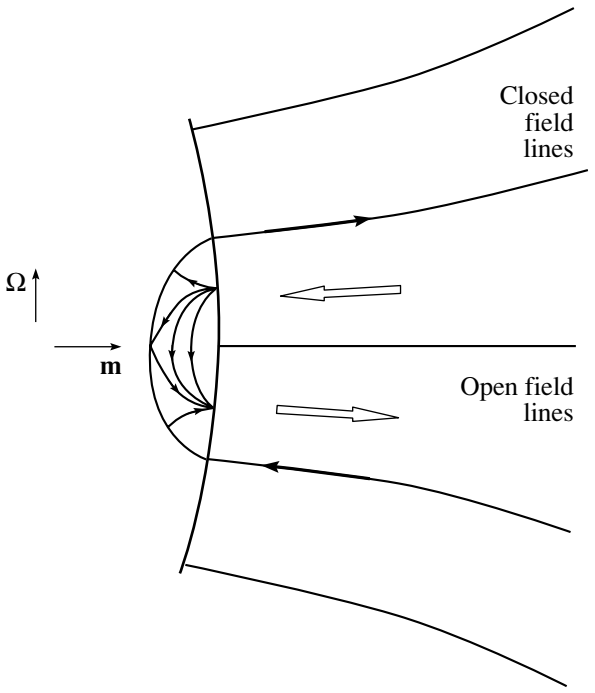

Fig. 2. Structure of the electric currents flowing near the magnetic poles of an orthogonal rotator. The currents flowing along the separatrix (thin arrows) between the regions of closed and open field lines are reconciled with the bulk currents (contour arrows) in such a way that the closing surface current is entirely concentrated within the polar cap.

However, it is easy to show that, in reality, the closing surface currents cannot go beyond the polar cap. If this were the case, then the longitudinal currents would also exist in the region of the closed magnetosphere (see Fig. 3). Indeed, as relations (7) and (8) show, the existence of a surface current $\mathbf{J}_\mathrm{s}$ must inevitably be accompanied by the appearance of an electric field $\mathbf{E}_\mathrm{s}$, i.e., a potential difference between the different points on the neutron-star surface connected by closed magnetic field lines (points A

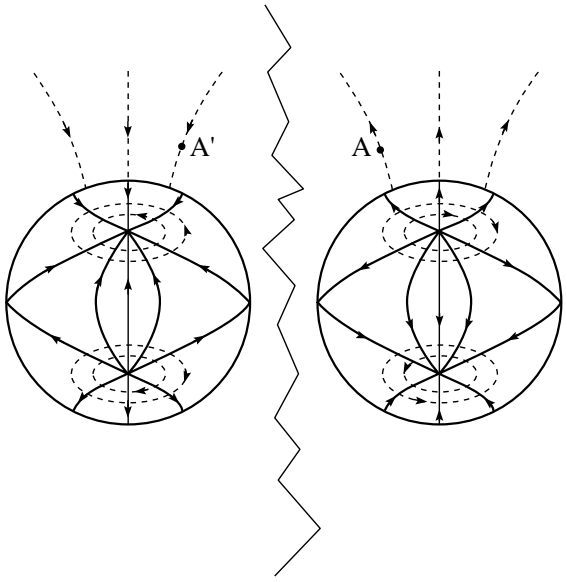

Fig. 3. Structure of the surface currents (solid lines) and the vortex magnetic field (dotted lines) for the two magnetic poles of an orthogonal rotator; the dashed lines indicate the surface currents outside the polar caps. The structure of the surface currents corresponds to solution (12).

and A′ in Fig. 3). However, this is in conflict with the assumption that there are no longitudinal currents in the region of the closed magnetosphere. Consequently, the currents flowing along the separatrix must be reconciled with the bulk currents flowing along the open field lines in such a way that the closing surface current is entirely concentrated within the polar cap. This leads to the boundary condition (11). As a result, the solution of Eq. (10) will be completely determined by the bulk longitudinal field i_0. For example, for the Goldreich current $i_0 = i_\mathrm{A} x \cos\varphi_\mathrm{m}$ and at $x_0 = \mathrm{const}$,

$$\xi = i_\mathrm{A} \frac{x(x^2 - x_0^2)}{8} \cos\varphi_\mathrm{m}. \qquad (12)$$

The subsequent line of reasoning is identical to that in our monograph Beskin *et al.* (1993). For an arbitrary angle of axial inclination χ, the current i_0 can be written as the sum of symmetric and asymmetric components, $i_\mathrm{S} + i_\mathrm{A}$. The time when the cone of open field lines whose boundary is specified by the angle $\theta_0 = (\Omega R/c)^{1/2}$ crosses the surface on which the Goldreich charge density ρ_GJ (2) changes sign is considered as the current asymmetry criterion. It would be natural to normalize the longitudinal current to the Goldreich current $j_\mathrm{GJ} = c\rho_\mathrm{GJ}$. Assuming that the magnetic field of the pulsar is dipolar, we obtain for the Goldrecih current at $x \ll 1$

$$i_\mathrm{GJ}(x, \varphi_\mathrm{m}) \approx \cos\chi + \frac{3}{2} x \cos\varphi_\mathrm{m} \sin\chi. \qquad (13)$$

Since $x \simeq (\Omega R/c)^{1/2}$ within the polar cap, $i_\mathrm{GJ} \sim 1$ at $\chi \simeq 0$ and $i_\mathrm{GJ} \sim (\Omega R/c)^{1/2}$ at $\chi \simeq 90^\circ$. Below, we write the current i_0 as $i_0 = i_\mathrm{S} + (\Omega R/c)^{1/2} i_\mathrm{A} \cos\varphi_\mathrm{m}$, where $i_\mathrm{S} \approx \cos\chi$ and $i_\mathrm{A} \approx \sin\chi$ are the amplitudes of the symmetric and asymmetric longitudinal currents normalized to the corresponding components of the Goldreich current (13).

Next, let us determine the torque exerted on the pulsar from the surface currents. It can be written as

$$\mathbf{K} = \frac{1}{c} \int [\mathbf{r} \times [\mathbf{J}_s \times (\mathbf{B}_0 + \mathbf{B}_\mathrm{c})]]\, dS, \qquad (14)$$

where $\mathbf{B}_\mathrm{c}$ is the magnetic field induced by the current $i_{||}$. The field $\mathbf{B}_\mathrm{c}$ at distances of the order of the size of the polar cap from the spin axis (when $\chi = 0$, i.e., when $\mathbf{B}_\mathrm{c}$ is at a maximum) is weaker than the dipole magnetic field $\mathbf{B}_0$ by a factor of $(\Omega R/c)^{3/2}$, so this term in the expression for $\mathbf{K}$ may be disregarded.

Let us decompose the braking torque $\mathbf{K}$ into unit vectors $\mathbf{e}_\mathrm{m}$, $\mathbf{n}_1$, and $\mathbf{n}_2$, where $\mathbf{e}_\mathrm{m} = \mathbf{m}/|\mathbf{m}|$, the vector $\mathbf{n}_1$ is perpendicular to the magnetic moment $\mathbf{m}$ and lies in the plane formed by the vectors $\mathbf{\Omega}$ and $\mathbf{m}$, and the vector $\mathbf{n}_2$ complements these to a right-hand triple:

$$\mathbf{K} = K_{||}\mathbf{e}_\mathrm{m} + K_\perp \mathbf{n}_1 + K_\dagger \mathbf{n}_2. \qquad (15)$$

As a result, we obtain (Beskin *et al.* 1993)

$$K_{||} = -\frac{B_0 R^2}{c} \int_0^{2\pi} d\varphi_\mathrm{m} \int_0^{x_0(\varphi_\mathrm{m})} dx x^2 \sqrt{1 - x^2} \frac{\partial \xi}{\partial \varphi_\mathrm{m}}, \qquad (16)$$

$$K_\perp = K_1 + K_2, \qquad (17)$$

$$K_1 = \frac{B_0 R^2}{c} \int_0^{2\pi} d\varphi_\mathrm{m} \int_0^{x_0(\varphi_\mathrm{m})} dx \left[x \cos\varphi_\mathrm{m} \frac{\partial \xi}{\partial x} - \sin\varphi_\mathrm{m} \frac{\partial \xi}{\partial \varphi_\mathrm{m}} \right], \qquad (18)$$

$$K_2 = \frac{B_0 R^2}{c} \int_0^{2\pi} d\varphi_\mathrm{m} \int_0^{x_0(\varphi_\mathrm{m})} dx x^3 \cos\varphi_\mathrm{m} \frac{\partial \xi}{\partial x}; \qquad (19)$$

$K_\dagger$ does not appear in the Euler equation that describes the rotation dynamics of the neutron star at all (see below (21)).

The following should be noted here: the magnetic-field structure near the pulsar surface is symmetric

relative to the plane that passes through the angular velocity and magnetic moment vectors of the neutron star. Therefore, the surface currents must have the same symmetry. This is because the terms in $K_{||}$ and $K_\perp$ proportional to $\Sigma_\perp/\Sigma_{||}$ are equal to zero.

Since the integration over x in (18) and (19) is performed to the boundary of the polar cap $x_0(\varphi_m) \sim (\Omega R/c)^{1/2}$, we could set $K_2 \sim (\Omega R/c)K_1$, i.e., $K_2 \ll K_1$, as an estimate. However, as is easy to verify, when the boundary condition (11) is satisfied, the integrand in (18) is the total derivative with respect to φ_m:

$$\int_0^{x_0(\varphi_m)} dx\left(x\cos\varphi_m\frac{\partial\xi}{\partial x} - \sin\varphi_m\frac{\partial\xi}{\partial\varphi_m}\right) = \frac{\partial}{\partial\varphi_m}$$

$$\times\left[-\int_0^{x_0(\varphi_m)} dx\xi\sin\varphi_m + \xi(x_0,\varphi_m)x_0(\varphi_m)\sin\varphi_m\right].$$

Therefore, the contribution of K_1 proves to be identically equal to zero.

At the same time, the estimates for $K_{||}$ and $K_\perp$ are

$$K_{||} = \frac{B_0^2\Omega^3R^6}{c^3}\left[-c_{||}i_S + \mu_{||}\left(\frac{\Omega R}{c}\right)^{1/2}i_A\right],$$

$$K_\perp = \frac{B_0^2\Omega^3R^6}{c^3}\left[\mu_\perp\left(\frac{\Omega R}{c}\right)^{1/2}i_S + c_\perp\left(\frac{\Omega R}{c}\right)i_A\right],$$

where $c_{||}$ and $c_\perp$ are factors of the order of unity that depend on the specific profile of the longitudinal current and on the shape of the polar cap. As regards the coefficients μ, these are completely related to the asymmetry of the polar cap, and their contribution is insignificant (for more detail, see Beskin *et al.* 1993). In particular, $\mu_{||}(0) = \mu_\perp(0) = 0$ and $\mu_{||}(\pi/2) = \mu_\perp(\pi/2) = 0$.

The disappearance of the leading term in Eq. (17) for the energy losses can be explained as follows. It is well known that the energy losses by radio pulsars (3) can be identically rewritten as (Beskin 1997)

$$W_{tot} = c\int(\mathbf{B}\mathbf{b}_R)(\mathbf{B}d\mathbf{S}), \qquad (20)$$

where the vector $\mathbf{b}_R = [\mathbf{\Omega}\times\mathbf{r}]/c$ is directed along the $\mathbf{e}_\varphi$ axis. At the light cylinder, Eq. (20) is identical to (3), but it can also be used near the neutron-star surface. It can be easily verified that the condition for the current closing within the polar cap (11) is equivalent to the condition for the total screening of the magnetic field $\mathbf{B}_c$ attributable to the longitudinal currents outside the region of open field lines. Therefore, as shown in Fig. 3, the toroidal magnetic field that determines $(\mathbf{B}\mathbf{b}_R)$ cannot go beyond the polar cap either. As a result, in the zeroth approximation, the mean value of the scalar product $(\mathbf{B}\mathbf{b}_R)$ in the region of open field lines is equal to zero, and the losses (20) themselves are determined by the small corrections $\sim(\Omega R/c)$ related to the curvature of the neutron-star surface. Clearly, the picture must also be the same at the light cylinder. In other words, the mean toroidal magnetic field $B_\varphi(R_L) \sim i_0B_p(R_L)$ at the light cylinder must be equal to zero. This is the reason for the difference between the energy loss estimates for pulsars at the stage of an orthogonal rotator.

Writing now the Euler equations, we can find the changes in the angular velocity $\dot\Omega$ and in the angle between the magnetic-field direction and the pulsar spin axis $\dot\chi$:

$$J_r\frac{d\Omega}{dt} = K_{||}\cos\chi + K_\perp\sin\chi, \qquad (21)$$

$$J_r\Omega\frac{d\chi}{dt} = K_\perp\cos\chi - K_{||}\sin\chi.$$

Here, for simplicity, we assume that the neutron star is spherically symmetric, so its moment of inertia J_r does not depend on the orientation of the spin axis. As a result, for angles χ that are not too close to 90°, so that $\cos\chi > (\Omega R/c)^{1/2}$ (i.e., when the symmetric currents play a major role), we obtain

$$\frac{d\Omega}{dt} = -c_{||}\frac{B_0^2\Omega^3R^6}{J_rc^3}i_S\cos\chi, \qquad (22)$$

$$\frac{d\chi}{dt} = c_{||}\frac{B_0^2\Omega^2R^6}{J_rc^3}i_S\sin\chi. \qquad (23)$$

As can be easily seen, Eqs. (22) and (23) lead to the conservation of invariant (1), $\Omega\sin\chi = \text{const}$. This is because the braking torque $\mathbf{K}$ (14) for the symmetric currents is opposite to the magnetic dipole $\mathbf{m}$, so the angular velocity component $\mathbf{\Omega}$ along the axis perpendicular to $\mathbf{m}$ is an integral of motion. In contrast, for $\chi \approx 90°$,

$$\frac{d\Omega}{dt} = -c_\perp\frac{B_0^2\Omega^4R^7}{J_rc^4}i_A, \qquad (24)$$

since the contribution of the symmetric current may be disregarded here due to the dependence $i_S \approx \cos\chi$. A comparison of Eqs. (22) and (23) indicates that, other things being equal, the energy release for pulsars at the stage of an orthogonal rotator is a factor of $\Omega R/c$ smaller than that for coaxial pulsars.

THE STATISTICS OF WEAKLY RADIATING PULSARS

Let us now discuss the statistics of weakly radiating pulsars. As was noted above, if the initial period P_0 of the neutron star was short, then the

radio pulsar will pass into the region of an orthogonal rotator, $\chi > \pi/2 - (\Omega R/c)^{1/2}$, where $\cos\chi < (\Omega R/c)^{1/2}$, before it reaches the death line $P = P_d(\chi)$, $\chi = \chi_d(P)$. In this case, as was shown above, the asymmetric surface current begins to play a major role, while the energy losses decrease by a factor of $\Omega R/c$ and, at the same time, cease to depend on the angle χ. Therefore, for such pulsars, we may not consider their distribution in χ, but immediately pass to the averaged the distribution function

$$N_0(P, B_0) = \int N_0(P, B_0, \chi) d\chi.$$

Below, we assume that the function $N_0(P, B_0)$ depends on the magnetic field B_0 of the neutron star only as on a parameter. In other words, we disregard the evolution of the magnetic field over the lifetime of the radio pulsar. The validity of this assumption for normal radio pulsars now seems to have been proven, since their lifetime does not exceed the evolution time scale of the magnetic field. As regards weakly radiating pulsars, this question will be considered below.

As a result, the continuity equation for the distribution function $N_0(P, B_0)$ of weakly radiating pulsars can be written as

$$\frac{d}{dP}\left(N_0 \frac{dP}{dt}\right) = F(P, B_0), \qquad (25)$$

where the source $F(P, B_0)$ is determined by the flux of neutron stars from the region of normal radio pulsars. For $\chi \sim 90^\circ$, it can be written as

$$F(P, B_0) = F(P, B_0, \chi)|_{\cos\chi = (\Omega R/c)^{1/2}},$$

where

$$F(P, B_0, \chi) = \dot{\chi} N_1 = \frac{\dot{P}}{P} \tan\chi N_1.$$

Here, $N_1(P, B_0, \chi)$ is the distribution function of normal pulsars, and we use the integral of motion $I = \sin\chi/P$ in explicit form. At the same time, the sink will be the crossing of the death line by pulsars at the period $P_*(B_0)$ that must now be determined from the condition

$$\cos\chi_d(P) = (2\pi R/cP)^{1/2}. \qquad (26)$$

As a result, the full distribution function of weakly radiating pulsars is $N^{(\mathrm{orth})}(P, B_0) = N_0(P, B_0)\theta[P_*(B_0) - P]$.

In this paper, we rely on our previous results (Beskin *et al.* 1993). Thus, for the distribution function of normal radio pulsars, we use the expression

$$N_1(P, B_0, \chi) = 2k_{\mathrm{N}} N_f P \frac{1}{B_k}\left(\frac{B_0}{B_k}\right)^{0.57} \times \left(1 + \frac{B_0}{B_k}\right)^{-3.7} \frac{1 - \cos\chi}{\sin^2\chi} \cos^{-0.5}\chi. \qquad (27)$$

Here, $B_k = 10^{12}$ G is the magnetic field typical of radio pulsars, k_{N} is the normalization factor defined below, and N_f is the number of normal pulsars far from the death line. The death line itself for normal pulsars (see Fig. 1) is given by the relation

$$P_{\mathrm{d}}(\chi) = B_{12}^{8/15} (\cos\chi)^{0.29} \quad \mathrm{s}, \qquad (28)$$

so $P_* = 0.3 B_0^{4/9}$ s. As a result, the differential equation for the function $N_0(P, B_0)$ takes the form

$$\frac{d}{dP}(N_0 P^{-2}) = 2k_{\mathrm{N}} N_f \frac{1}{B_k}\left(\frac{B_0}{B_k}\right)^{0.57} \times \left(1 + \frac{B_0}{B_k}\right)^{-3.7} \frac{1}{a^{3/2} P^{5/4}},$$

where we denote $a = (2\pi R/c)^{1/2}$. The solution of this equation is the sought distribution function:

$$N_0 = k_{\mathrm{N}} N_f \frac{1}{B_k}\left(\frac{B_0}{B_k}\right)^{0.57} \left(1 + \frac{B_0}{B_k}\right)^{-3.7} \times \frac{8P^2}{a^{3/2}}\left[\frac{1}{P_{\min}^{1/4}} - \frac{1}{P^{1/4}}\right]. \qquad (29)$$

Here, we had to introduce the minimum period $P_{\min}$ that can be determined from the condition $N_0(P_{\min}) = 0$; below, it is set equal to 0.1 s. The distribution function depends weakly on this parameter due to the factor $P_{\min}^{-1/4}$.

Let us now compare our results with the observational data. In this case, several corrections to N_0 and N_1 must be applied. First, we must take into account the probability that the observer falls within the beam of the radio pulsar. The visibility function A that defines this probability is proportional to $\sin\chi$ (this factor is determined by the solid angle subtended by the cone into which the radio emission from the pulsar goes), and the window width w_r that, according to the observational data, is proportional to $P^{-0.1\pm0.1}$ (for more detail, see Beskin *et al.* 1993). As a result, multiplying the distributions N_0 and N_1 by the visibility function $A = \sin\chi P^{-0.1}$ yields

$$N_0' = 8k_{\mathrm{N}} N_f \frac{1}{B_k}\left(\frac{B_0}{B_k}\right)^{0.57} \left(1 + \frac{B_0}{B_k}\right)^{-3.7} \times \frac{P^{1.9}}{a^{3/2}}\left[\frac{1}{P_{\min}^{1/4}} - \frac{1}{P^{1/4}}\right], \qquad (30)$$

$$N_1' = 2k_{\mathrm{N}} N_f P^{0.9} \frac{1}{B_k}\left(\frac{B_0}{B_k}\right)^{0.57}$$

$$\times \left(1+\frac{B_0}{B_k}\right)^{-3.7} \frac{1-\cos\chi}{\sin\chi}\cos^{-0.5}\chi.$$

Next, the sensitivity of the instruments that record the signals from radio pulsars should be taken into account. Here, the following corrections are possible:

(1) The period dependence of the radiation intensity and, hence, the shift in the maximum of the visible distribution function toward the shorter periods;

(2) The small factor $\Omega R/c$ in the intensity of weakly radiating pulsars compared to normal pulsars.

Let us discuss the necessity of applying the correction attributable to the period dependence of the intensity. The intensity of the received signal depends on the distance to the pulsar r, its magnetic field B_0, and the pulsar spin period P: $I \propto W/r^2 \propto \Omega\dot{\Omega}/r^2 \propto B_0^2(r^2P^5)^{-1}$ and $I \propto B_0^2(r^2P^4)^{-1}$ for weakly radiating and normal pulsars (see (22) and (24)), respectively. For example, if an instrument is sensitive enough for a pulsar with period P_0 to be observed from the maximum distance r_0, then this instrument will record sources with periods $P_1 < P_0$ at distances $r_1 = r_0\,(P_0/P_1)^{5/2} > r_0$. If the pulsars are assumed to have a disk spatial distribution so that the number of sources increases with distance as r^2, then the functions N_0 and N_1 should have been multiplied by B_0^2/P^5 and B_0^2/P^4, respectively. In this case, the shape of the distributions would change; in particular, the maxima of the period distribution functions would shift. However, analyzing the period distribution of pulsars for various distances (see Fig. 4), we see that the maxima of the distributions are not shifted relative to one another. For this reason, we will not apply the corresponding correction to the observed distribution functions. This is because the observed sample of pulsars was drawn using the observations of different groups with instruments of different sensitivities, and the above possible additional period dependence blurred.

Let us now discuss the correction attributable to the significantly reduced energy release of weakly radiating pulsars. As was noted above, the radiation from pulsars with $\chi \approx 90^\circ$ is a factor of $(\Omega R/c)$ weaker than that from normal pulsars. Therefore, to determine the distribution function of visible weakly radiating pulsars $N_0^{\rm v}$, the distribution N_0 must be multiplied by $(\Omega R/c)^{d/2}$, where d is a number that depends on the assumed (disk or volume) distribution of pulsars in space and that takes on values from 2 (disk distribution) to 3 (volume distribution). The table gives the distances from the observer to the weakly radiating pulsars, r, and the distances from these pulsars to the plane of the Galactic disk, z. When this table was compiled, the selection criterion was a low spindown rate: $\dot{P} < 10^{-17}$. In addition, we excluded from our analysis millisecond pulsars with $P < 10$ ms, since their evolution, as was emphasized above, differs from that of normal radio pulsars. As we see, the ratio z/d averaged over these 11 weakly radiating radio pulsars is 0.26; this ratio would be equal to zero and 0.25 for disk and volume distributions, respectively. Below, we assume that $d = 3$. We emphasize that, in this case, the correction is mainly related not to the dependence of the energy losses on the radio pulsar period, but to the reducing factor $(\Omega R/c)^{3/2}$, in which the small quantity a^2 rather than the period dependence plays a major role.

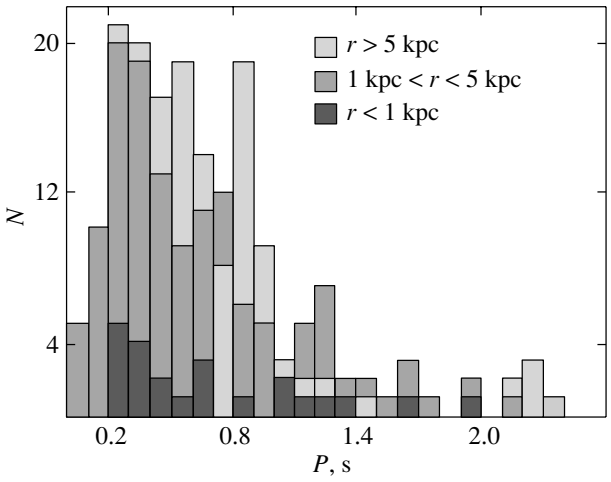

Fig. 4. Period distribution of pulsars for $r < 1$ and from 1 kpc $< r <$ 5 kpc and for $r > 5$ kpc.

Thus, we eventually obtain for the visible distribution functions $N_0^{\rm v}$ and $N_1^{\rm v}$

$$N_0^{\rm v} = 8k_{\rm N}N_f\frac{1}{B_k}\left(\frac{B_0}{B_k}\right)^{0.57} \tag{31}$$
$$\times \left(1+\frac{B_0}{B_k}\right)^{-3.7} P^{0.4}a^{3/2}\left[\frac{1}{P_{\rm min}^{1/4}}-\frac{1}{P^{1/4}}\right],$$

$$N_1^{\rm v} = 2k_{\rm N}N_f P^{0.9}\frac{1}{B_k}\left(\frac{B_0}{B_k}\right)^{0.57} \tag{32}$$
$$\times \left(1+\frac{B_0}{B_k}\right)^{-3.7} \frac{1-\cos\chi}{\sin\chi}\cos^{-0.5}\chi.$$

Let us now determine the numbers of weakly radiating and normal pulsars by integrating distributions (31) and (32) over the domains of these functions. As was showed in our monograph (Beskin *et al.* 1993), for a consistent comparison of the theory with observations, only the pulsars that are far from the death line should be taken into account when determining the function N_1. These pulsars

Weakly radiating pulsars

N	Pulsar	P, s	$\dot{P}$	Distance, kpc	z, kpc	$W_{\rm tot}$, erg s^{-1}
1	J0051 + 0423	0.354	7.00×10^{-18}	0.94	−0.80	$6.2 \times 10^{+30}$
2	B0331 + 45	0.269	7.35×10^{-18}	2.08	−0.29	$1.5 \times 10^{+31}$
3	J1124−5638	0.185	9.00×10^{-18}	23.74	1.76	$5.6 \times 10^{+31}$
4	J1320−3512	0.458	1.90×10^{-18}	0.93	0.43	$7.8 \times 10^{+29}$
5	J1355−6206	0.276	3.10×10^{-18}	7.95	−0.02	$5.8 \times 10^{+30}$
6	J1410−7404	0.278	6.74×10^{-18}	2.15	−0.45	$1.2 \times 10^{+31}$
7	J1548−4821	0.145	8.00×10^{-19}	3.76	0.31	$1.0 \times 10^{+31}$
8	J1819−1510	0.226	7.90×10^{-18}	5.61	−0.01	$2.7 \times 10^{+31}$
9	B1952 + 29	0.426	1.71×10^{-18}	0.42	0.01	$8.7 \times 10^{+29}$
10	J2222 + 2923	0.281	6.17×10^{-18}	4.46	−1.76	$1.1 \times 10^{+31}$
11	J2307 + 2225	0.535	8.70×10^{-18}	0.38	−0.22	$2.2 \times 10^{+30}$

can be found from the condition $Q < 1$, where $Q = 2P^{11/10}\dot{P}_{-15}^{-2/5}$. 700 such pulsars are currently known (Manchester 2003). As a result, integrating the distribution function of normal radio pulsars $N_1^{\rm v}$ yields

$$I_1(B_{12}) = \int_{P_{min}}^{P_*} dPP^{0.5} \tag{33}$$

$$\times \int_0^{\arccos(P^4/B_{12}^{2.13})} d\chi \frac{1-\cos\chi}{\sin\chi}\cos^{-0.5}\chi,$$

$$I_2(B_{12}) = \int_{P_*}^{P_{max}} dPP^{0.5}$$

$$\times \int_0^{\arccos(a/P^{1/2})} d\chi \frac{1-\cos\chi}{\sin\chi}\cos^{-0.5}\chi,$$

$$I_3 = \int_0^{\infty} d\left(\frac{B_0}{B_k}\right)\left(\frac{B_0}{B_k}\right)^{0.57}\left(1+\frac{B_0}{B_k}\right)^{-3.7}$$

$$\times \left[I_1(B_{12}) + I_2(B_{12})\right],$$

where $P_{\rm min} \simeq 0.1$, $P_{\rm max} = (B_0/B_k)^{0.53}$ and $P_* = a^{0.33}\left(\frac{B_0}{B_k}\right)^{0.44}$, and B_{12} is the magnetic field in

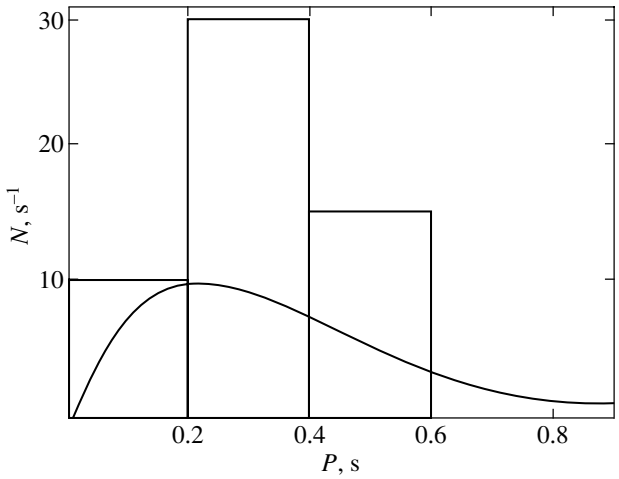

Fig. 5. Theoretical (line) and observed (histogram) period distribution functions of weakly radiating pulsars.

10^{12} G. Given I_3, the constant k_N can be determined from the normalization condition $2k_N I_3 = 1$. As a result, we obtain $k_N \approx 4.4$.

Integrating N_0^v over B_0 yields the period distribution function of weakly radiating pulsars shown in Fig. 5. The derived curve is in good agreement with the histogram constructed from observational data. In particular, it correctly reproduces the shape of the observed distribution, and the number of weakly radiating pulsars calculated from the function N_0^v and equal to 5 closely matches the number of such pulsars as estimated from ATNF data (Manchester 2003) equal to 11 (these are given in the table). As we see, the theoretical predictions and the observations are in good agreement.

CONCLUSIONS

Thus, our detailed analysis of the energy losses by weakly radiating radio pulsars has confirmed our conclusion that when neutron stars pass into the region of angles $\chi \sim 90°$, their total rotational energy losses prove to be a factor of $(\Omega R/c)$ smaller than those for a coaxial rotator. We showed that this conclusion directly follows from the absence of closing surface currents outside the polar cap. Both the total number of weakly radiating radio pulsars and their distribution in period P were shown to be in good agreement with theoretical predictions. Thus, the theory of current losses itself has received yet another confirmation.

Note, however, that if we assumed a disk distribution of weakly radiating radio pulsars, i.e., took $d = 2$, then integration of the distribution function would yield 169 weakly radiating pulsars. Thus, the pattern of the assumed distribution of pulsars in space affects significantly their number obtained using the period distribution function for these pulsars.

However, there are several factors that can be invoked to explain such a large discrepancy (by more than a factor of 10). First, the number of weakly radiating pulsars is determined by the distribution function of normal pulsars at short periods where the simple analytical expression (27) may not hold. This distinction does not affect the complete sample of pulsars, but can change significantly the number of short-period pulsars. In addition, the dynamical ages of weakly radiating pulsars $\tau_D^{(orth)}$, $\tau_D^{(orth)} \sim a^{-2}\tau_D$, must be at least three orders of magnitude older than those of normal pulsars τ_D, i.e., 10^9–10^{10} yr, which may exceed the evolution time of the neutron-star magnetic field (Yakovlev *et al.* 1999). In other words, the hypothesis itself about a constant magnetic field for weakly radiating pulsars may no longer realistic. Consequently, the lifetimes of neutron stars at the stage of weakly radiating pulsars (and, hence, their total number) could be much smaller than follows from our simplified analysis.

ACKNOWLEDGMENTS

We wish to thank A.V. Gurevich and Ya.N. Istomin for their fruitful discussions. This work was supported by the Russian Foundation for Basic Research (project no. 02-02-16762). E.E. Nokhrina also thanks the Dynasty Foundation for their financial support.

REFERENCES

1. V. S. Beskin, Usp. Fiz. Nauk **167**, 689 (1997).
2. V. S. Beskin, A. V. Gurevich, and Ya. N. Istomin, Astrophys. Space Sci. **102**, 301 (1984).
3. V. S. Beskin, A. V. Gurevich, and Ya. N. Istomin, *Physics of the Pulsar Magnetosphere* (Cambridge Univ. Press, Cambridge, 1993).
4. V. M. Lipunov, *Astrophysics of Neutron Stars* (Nauka, Moscow, 1987) [in Russian].
5. I. V. Malov, Astron. Zh. **67**, 377 (1990) [Sov. Astron. **34**, 189 (1990)].
6. R. N. Manchester, ATNF Catalog, www.atnf.csiro.au/research/pulsar (2003).
7. L. Mestel, *Stellar Magnetism* (Clarendon Press, Oxford, 1999).
8. L. Mestel, P. Panagi, and S. Shibata, Mon. Not. R. Astron. Soc. **309**, 388 (1999).
9. T. M. Tauris and R. N. Manchester, Mon. Not. R. Astron. Soc. **306**, 50 (1999).
10. D. G. Yakovlev, K. P. Levenfish, and Yu. A. Shibanov, Usp. Fiz. Nauk **169**, 825 (1999).

Translated by V. Astakhov

Astronomy Letters, Vol. 30, No. 10, 2004, pp. 694–706. Translated from Pis'ma v Astronomicheskiĭ Zhurnal, Vol. 30, No. 10, 2004, pp. 764–777.

Disk Wind in Young Binaries and the Origin of the Cyclic Activity of Young Stars

V. P. Grinin[1, 2, 3*], L. V. Tambovtseva[1], and N. Ya. Sotnikova[2]

[1] *Pulkovo Astronomical Observatory, Russian Academy of Sciences, Pulkovskoe shosse 65, St. Petersburg, 196140 Russia*

[2] *Sobolev Astronomical Institute, St. Petersburg State University, Universitetskiĭ pr. 28, St. Petersburg, 198504 Russia*

[3] *Crimean Astrophysical Observatory, pos. Nauchnyĭ, Crimea, Ukraine*

Received March 19, 2004

Abstract—We present the results of our numerical simulations of the cyclic brightness modulation in young binary systems with eccentric orbits and low-mass secondary components. We suggest that the binary components accrete matter from the remnants of the protostellar cloud, with the main accretor (according to current models) being the low-mass component. The brightness variations of the primary are attributable to the periodic extinction variations on the line of sight caused by the disk wind from the secondary and by the common envelope produced by this wind. The distribution of matter in the envelope was calculated in the ballistic approximation. When calculating the optical effects produced by the dust component of the disk wind, we adopted the dust-to-gas mass ratio of 1 : 100 characteristic of the interstellar medium and the optical parameters of the circumstellar dust typical of young stars. Our calculations show that the theoretical light curves for binaries with elliptical orbits exhibit a wider variety of shapes than those for binaries with circular orbits. In this case, the parameters of the photometric minima (their depth, duration, and shape of the light curve) depend not only on the disk-wind parameters and the orbital inclination of the binary to the line of sight, but also on the longitude of the periastron. We investigate the modulation of the scattered radiation from the common envelope with orbital phase in the single-scattering approximation. The modulation amplitude is shown to be at a maximum when the system is seen edge-on and to be also nonzero in binaries seen pole-on. We discuss possible applications of the theory to young stellar objects. In particular, several model light curves have been found to be similar to those of candidate FU Orionis stars (FUORs).

Key words: *stars—young binaries, accretion, disk wind, activity cycles, UXORs.*

INTRODUCTION

Recent photometric studies have shown that eclipsing systems with long-lasting eclipses are encountered among young binary stars. For example, in the binary GW Ori ($P = 242^d$; Mathieu *et al.* 1991) whose primary is a T Tauri star, the eclipse duration is about 1/10 of the orbital period (Shevchenko *et al.* 1998). In the weak T Tauri star (WTTS) KH 15D ($P = 48\overset{d}{.}36$; Kearns and Herbst 1998; Hamilton *et al.* 2001; Herbst *et al.* 2002), the eclipse duration, in fractions of the orbital period, is even longer, about 1/3. In the binary HD 200 775 with an orbital period of about three years (Pogodin *et al.* 2004) whose primary is a Herbig Ae/Be star, the eclipse duration is comparable to the orbital period (Ismailov 2003). Quite recently, yet another WTTS, H 187, with an eclipse duration of 3.6 yr, has been discovered in the cluster IC 348 (Cohen *et al.* 2003). Only one eclipse has been completely observed to date. Therefore, the period of this binary can be estimated only roughly: about four years (Cohen *et al.* 2003). The interpretation of such eclipses in terms of classical models for eclipsing binaries in which the eclipsing body is either the secondary itself or a gas and dust envelope that fills its Roche lobe leads to serious contradictions with the physics of young stars or is not possible in principle (as, e.g., in the case of KH 15D and H 187), because the gas and dust envelope around the secondary for such long-lasting eclipses must have sizes comparable to the orbital radius. Such envelopes are unstable and are rapidly destroyed by tidal perturbations.

It has recently been shown (Grinin and Tambovtseva 2002) that a somewhat unusual mechanism of eclipses can take place in young binaries that still

* E-mail: grinin@vg1723.spb.edu

continue to accrete matter from the remnants of the protostellar cloud. In this mechanism, the disk wind from the secondary or, more precisely, its dust component acts as the eclipsing body. Since the disk wind is an extended structure, the eclipses of the primary caused by it can be long-lasting. In contrast to the classical models of eclipsing binaries in which eclipses occur only when the line of sight lies in the orbital plane or deviates from it by a small angle, eclipses by the disk wind are possible even at large inclinations of the binary to the line of sight. In this case, the larger the inclination, the longer-lasting the eclipses can be. This suggests that the fraction of eclipsing systems among young pairs must be, first, higher than that among main-sequence binary stars. Second, the fraction of eclipsing systems with long-lasting eclipses must be higher among young pairs.

Therefore, further study of the optical effects produced by the disk wind in young binaries is of considerable interest. In this paper, which is a continuation of our previous paper (Grinin and Tambovtseva 2002), we present the results of our numerical simulations of the cyclic phenomena created by the dust component of the disk wind from a low-mass secondary during its orbital motion. We analyze the dependence of the theoretical light curves on the parameters of the disk wind and the binary system, including its orientation in space. In contrast to our previous paper, in which we solved a similar problem for binaries with circular orbits, we below consider the general case of binaries with elliptical orbits.

FORMULATION OF THE PROBLEM

As in our previous paper (Grinin and Tambovtseva 2002), we take the model of a young binary system by Artymowicz and Lubow (1996) as the basis and restrict our analysis to the case where the mass of the secondary is much lower than that of the primary.[1] A gap that is almost free from matter is formed at the center of such a system under periodic gravitational perturbations (Fig. 1). Its characteristic size depends on the eccentricity e and the component mass ratio $q = m_2/m_1$ and is equal to $\approx(2-3)a$, where a is the orbital semimajor axis of the secondary (Artymowicz and Lubow 1994).

[1] According to the statistics of main-sequence binary stars (Duquennoy and Mayor 1991; Mazeh *et al.* 2000), such component mass ratios are characteristic of binaries with periods $P \geq 3$ yr, but are also encountered in binaries with shorter periods. The latter include, in particular, stars with substellar companions whose number rapidly increases owing to the ongoing searches for such systems (Mayor and Urdy 2000)

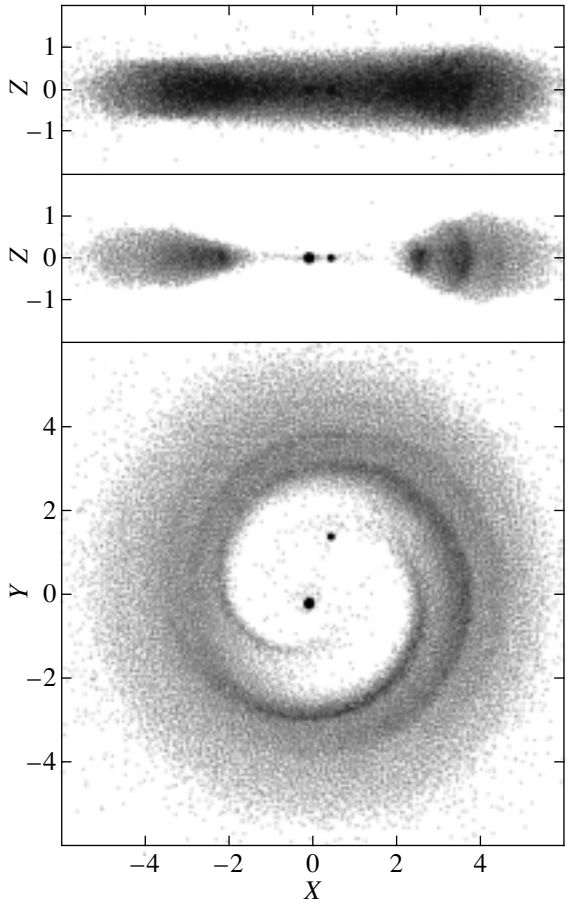

Fig. 1. Distribution of matter in the CB disk of a young binary system calculated by the SPH method for one of the orbital phases; from top to bottom: an edge-on view in projection onto the XZ plane, the CB-disk cross section in this plane, and a pole-on view. The X, Y, Z coordinates are given in units of the orbital semimajor axis of the secondary. The model parameters are as follows: eccentricity $e = 0.5$ and component mass ratio $q = 0.22$.

The binary components accrete matter from the remnants of the protostellar cloud that forms the so-called circumbinary (CB) disk. In this case, as Artymowicz and Lubow (1994) showed (see also Bate and Bonnell 1997; Rožiczka and Laughlin 1997), the accretion rate onto the low-mass component can exceed significantly the accretion rate onto the primary in the binary system. Since disk accretion is accompanied by mass outflow from the accretion disk (disk wind), the low-mass component under these conditions becomes an intense source of matter that it scatters during its orbital motion above (and below) the plane of the CB disk. Calculations show that the dust present in the wind[2] can cause long-lasting eclipses of the primary in the binary system (Grinin

[2] As was shown by Safier (1993), as a result of their collisions with gas atoms, dust grains in the accretion disk are en-

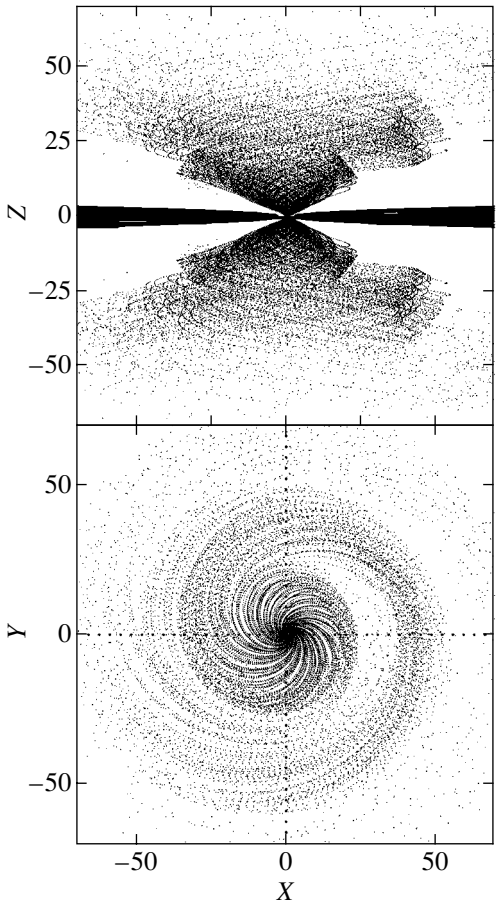

Fig. 2. Distribution of matter in the common envelope of a young binary system produced by the disk wind from the secondary in projection onto XZ plane (upper panel) and the equatorial XY plane (lower panel) of the binary. The secondary is at the point with coordinates $X = 1$ and $Y = 0$. The coordinates of the primary in the XY plane are (0, 0). All coordinates are given in units of the orbital semimajor axis of the secondary. The model parameters are as follows: $V_w = 3$, $U_w = 0.5$, and $e = 0.5$.

and Tambovtseva 2002) and can become a source of thermal radiation in the near infrared comparable in intensity to the radiation from the CB disk itself (Grinin 2002).

Structure of the CB Disk

As an example, Fig. 1 shows the structure of the CB disk around a young binary system with a low-mass secondary. We computed the distribution of matter in the disk in the hydrodynamic approximation by the SPH (smoothed particle hydrodynamics) method using a scheme similar to that described by Hernquist and Kats (1989), but with a constant smoothing length of the hydrodynamic quantities. Two streams of matter from the CB disk that feed the accretion disks around the binary components are seen in projection onto the equatorial plane. The density waves attributable to periodic gravitational perturbations are seen in the CB disk itself. This distribution of matter in the CB disk is in good agreement with the SPH simulations (Artymowicz and Lubow 1996).

A peculiarity of binary systems with elliptical orbits is the global asymmetry in the azimuthal distribution of matter in the CB disk that is clearly seen when the binary is viewed pole-on, edge-on, and in cross section (Fig. 1). As Lubow and Artymowicz (2000) showed, an asymmetric CB disk slowly precesses with a precession period much longer than the orbital period. In cross section, the CB disk resembles the classical accretion disk around a single young star in which the bulk of the matter is concentrated in a geometrically thin equatorial layer with a thickness $H \ll r$.

A manifestation of the global asymmetry of the CB disk noted above is the dependence of its geometric thickness H not only on the distance from the center r, but also on the azimuth. For this reason, precession of the CB disk must cause long-term periodic extinction variations in young binaries seen nearly edge-on, where the line of sight is tangential to the disk surface. It is also clear that the global asymmetry of the CB disk is a source of intrinsic polarization in young binaries.

FORMATION OF THE COMMON ENVELOPE

The disk wind from the secondary makes significant changes to the model of a young binary system: during the orbital motion of the secondary, it forms a structurally complex asymmetric common envelope (Fig. 2) that partially dissipates into ambient space and partially can be captured by the primary. As a result, dust that produces additional extinction on the line of sight appears above the plane of the binary.

Inertial Properties of Accretion Disks

A peculiarity of young binary systems with elliptical orbits is that the accretion rate on the binary components is strongly modulated with a period equal to the orbital period (Artymowicz and Lubow 1996). In binaries with highly eccentric orbits ($e \geq 0.3$), the modulation depth can be so large that the accretion rates at the apoastron and periastron of the orbit can differ by a factor of 10 or more (Artymowicz and Lubow 1996; Rožiczka and Laughlin 1997). A possible result of the dependence of the accretion rate $\dot{M}_a$ on the orbital phase is that the mass loss rate

trained by atoms and are present in approximately the same proportion in the disk wind.

in the disk wind $\dot{M}_w$ can also be a periodic function of the time. However, since the accretion disk is an inertial system, the modulation depth of $\dot{M}_w$ depends on the relationship between the orbital period P and the gas-dynamic time t_g. The latter is the characteristic dissipation time of an accretion disk without external replenishment. If it is shorter than the orbital period P, then the accretion disk has time to track the changes at its outer boundary attributable to the changes in the accretion rate. In this case, $\dot{M}_w \propto \dot{M}_a$. Otherwise, the response of the disk to the changes in $\dot{M}_a$ can be strongly smoothed.

According to Shakura and Sunyaev (1973),

$$t_g = R^2/\nu. \quad (1)$$

Here, R is the outer radius of the accretion disk, ν is the turbulent viscosity, $\nu = \alpha v_s H$, where H is the geometric thickness of the disk, v_s is the speed of sound, and α is a dimensionless parameter that depends on the turbulence generation mechanism in the accretion disk. Given that $v_s/v_\phi \approx H/R$, where v_ϕ is the Keplerian velocity at the outer boundary of the disk, and expressing t_g in units of the orbital period, we obtain

$$t_g = (2\pi\alpha)^{-1}(R/H)^2(t_{rot}/P), \quad (2)$$

where t_{rot} is the Keplerian rotation period at the outer boundary of the accretion disk around the low-mass component.

Relation (1) can be rewritten as

$$t_g = (2\pi\alpha)^{-1}(R/H)^2 q^{-1/2}(R/a)^{3/2}. \quad (3)$$

According to Artymowicz and Lubow (1994), for a component mass ratio of $q \approx 0.1$, the outer radius of the accretion disk around the low-mass component is $R \approx 0.1a$. Taking the standard (for accretion disks) ratio $H/R = 0.05$ and $R = 0.1a$, we obtain $t_g \approx 6.5\alpha^{-1}$ from Eq. (3).

The values of α are currently believed (see the review by Stone *et al.* (2000) and the references therein) to lie within the range $\alpha \approx 0.005$–0.5. Taking $\alpha = 0.5$ to estimate the lower limit for t_g, we obtain $t_g \geq 13$.

It thus follows that the characteristic gas-dynamic time of the accretion disk is much longer than the orbital period even in the models with highly efficient angular momentum transfer. Therefore, we conclude that the disk wind being formed mainly in the central part of the disk has no time to track the changes in the accretion rate at its outer boundary. However, the observations of certain young binaries with eccentric orbits suggest (see, e.g., Pogodin *et al.* 2004) that such parameters of the H_α emission line as its equivalent width and profile parameters are modulated with orbital period. This implies that the physical conditions in the central region of the accretion disk in which this line originates are subject to periodic variations attributable to the orbital motion of the binary components. These variations can be triggered by tidal perturbations and spiral shocks generated in the accretion disks of binary systems (Sawada *et al.* 1986a, 1986b; Bisikalo *et al.* 1995; Makita *et al.* 2000). As a result, the disk wind can be enhanced near the periastron of the orbit. Therefore, below, in addition to the conservative model with $\dot{M}_w = \text{const}$, we also consider the model of a binary system in which the disk wind is enhanced as the binary components approach each other. For simplicity, we consider the case where the outflow rate is proportional to the accretion rate.

Parameters of the Disk Wind

Let us recall briefly the basic parameters of the disk winds from young stars. Numerical simulations show (Goodson *et al.* 1999) that the bulk of the matter (up to 80%) is concentrated in the low-velocity component of the wind and is ejected from the accretion disk in the range of angles $\omega \approx 40°$–$60°$, where ω is the angle between the radial velocity vector of the wind and the axis of symmetry of the disk. In addition to the radial velocity component V_w, the wind matter near the accretion disk also has the azimuthal component U_w. Far from the accretion disk, the latter decreases according to the law of conservation of angular momentum, and the radial velocity is the dominant component. Below, while specifying the kinematic parameters of the wind, by the velocity components V_w and U_w we mean the values that the wind fragments gain after the completion of the acceleration phase, when the matter moves by inertia. According to the estimates obtained by Hartigan *et al.* (1995) and Hirth *et al.* (1997) from the observations of forbidden lines in the spectra of T Tauri stars, the characteristic velocity of the slow wind component at distances of ~ 1 AU from the star is of the order of several tens of kilometers per second.

Given the aforesaid, we assume that all particles of the wind are isotropically ejected with the same radial velocity V_w in the range of angles $40° \leq \omega \leq 60°$. The disk wind is assumed to have a mirror symmetry relative to the orbital plane. The radius of the accretion disk around the secondary is small compared to the orbital semimajor axis. Therefore, to simplify our calculations, we assume that the matter outflows from a point source whose coordinates coincide with those of the secondary and that the center of mass of the binary coincides with the position of the primary. In our simulations, we disregard the disk wind from

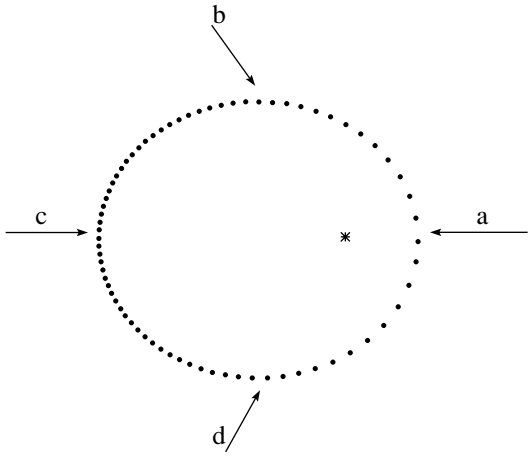

Fig. 3. Orbit of the low-mass companion in a binary system with an eccentricity of $e = 0.5$. The arrows indicate the four different directions to the observer for which the phase dependences of the column density (Fig. 4) and the light curves (Figs. 5–7) were calculated.

the primary, because, according to the conditions of the problem, the accretion rate on this component is much lower than that on the secondary.

We also assume that the disk wind is axisymmetric in the coordinate system of the secondary. This condition is satisfied in the cases where the tidal perturbations from the primary may be ignored. Since the radius of the accretion disk around the secondary is smaller than the radius of the tidal interaction and since, in addition, the inner layers of the accretion disk mainly contribute to the disk wind, this assumption seems quite justifiable. The highly eccentric binary systems constitute an exception. In such systems, the outer radius of the accretion disk around the secondary at the periastron of the orbit can be smaller than the radius of the tidal interaction; as a result, part of the matter from its disk could be captured by the primary at the closest approach. Under these conditions, large deviations from azimuthal symmetry can take place in the disk wind.

THE METHOD OF CALCULATION

As in our previous paper (Grinin and Tambovtseva 2002), we assume that the disk wind consists of weakly interacting fragments that are treated as independent (test) particles. When passing to the coordinate system of the primary, the particle velocity vector $\mathbf{V}_\mathrm{w} + \mathbf{U}_\mathrm{w}$ is added to the orbital velocity vector of the secondary $\mathbf{V}_\mathrm{K}$, causing the disk wind to become anisotropic:

$$\mathbf{V}_0 = \mathbf{V}_\mathrm{w} + \mathbf{U}_\mathrm{w} + \mathbf{V}_\mathrm{K}. \qquad (4)$$

In this case, part of the matter (ejected in directions opposite to the orbital motion of the secondary) can gain a velocity lower than the local escape velocity and can be captured by the primary.

We calculated the trajectories of particles in the gravitational field of the primary[3] in the ballistic approximation. In this case, the velocity of a particle $\mathbf{V}_0$ defined by Eq. (4) and its coordinates at the ejection time are considered as the initial conditions when calculating its trajectory. During our calculations, we divided the orbit of the secondary into n segments in such a way that the motion in each of them occurred during the same time interval $\Delta t = P/n$. We assumed that $n = 72$ or 180 (which corresponds to a 5° or 2° step in orbital motion, respectively, for a circular orbit). We used the same technique for simulating the common envelope as in our previous paper (Grinin and Tambovtseva 2002). The disk wind was simulated by isotropically ejecting test particles at each step in the above range of solid angles into the upper and lower half-spaces.

Thus, the model parameters of the problem are as follows:

(1) The orbital eccentricity e (we took $e = 0.5$ in our simulations);

(2) The radial V_w and azimuthal U_w velocities of the disk wind from the secondary (the Keplerian velocity of the secondary at the periastron was taken as unity: $V_\mathrm{K} = 1$);

(3) The rate of mass outflow from the accretion disk around the secondary $\dot{M}_\mathrm{w}$.

When calculating the optical parameters of the dust component of the disk wind, we assumed the dust-to-gas ratio to be the same as that in the interstellar medium, i.e., 1 : 100. For simplicity, we consider a monodisperse graphite–silicate mixture of dust grains similar in chemical composition to the interstellar dust (Mathis *et al.* 1977). The so-called astrosilicate is used as silicate. The grain radius is $s = 0.1$ μm, and the mean density is 3 g cm^{-3}. The optical parameters of such particles were calculated using the Mie theory previously (Grinin and Tambovtseva 2002).

RESULTS

The method described above was used to compute several models of the common envelopes for different orbital phases. As an example, one of these models is shown in Fig. 2. In binary systems with elliptical orbits, the test particle column density N

[3] The masses of the circumstellar disks of young stars generally do not exceed 0.1 $M_\odot$ (see, e.g., Natta *et al.* 2000), and their self-gravity may be disregarded.

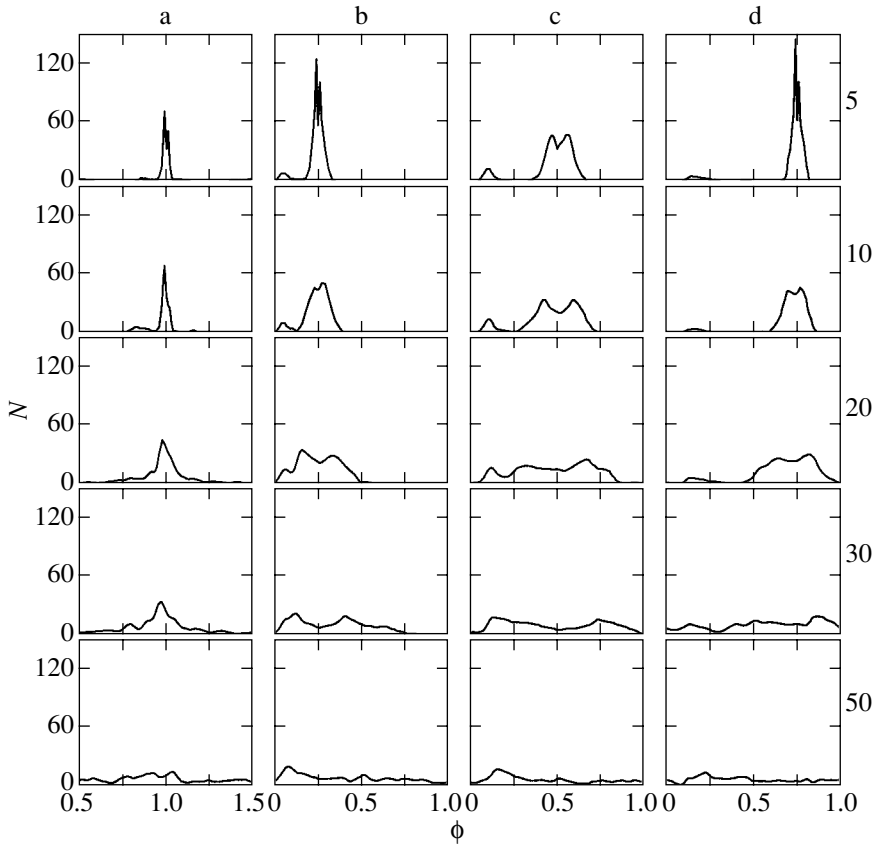

Fig. 4. Test particle column density N versus orbital phase ϕ in the model with $V_w = 1$, $e = 0.5$, and $U_w = 0$ for four orientations of the binary relative to the observer. The angle θ between the line of sight and the equatorial plane of the binary is indicated on the right.

toward the primary depends not only on the orbital phase ϕ and the inclination of the orbital plane to the line of sight θ, but also on the orbital orientation relative to the observer. Figure 3 shows the four orbital orientations of the secondary relative to the observer for each of which we calculated the column densities N as functions of ϕ and the corresponding optical depths τ. We passed from N to the column density of the actual dust grains N_d by rescaling in which we took into account the ratio of the total number of dust grains ejected by the wind over one period to the corresponding number of test particles (for details, see Grinin and Tambovtseva (2002)). We also took into account the difference in the column cross sections: the column density of the test particles was calculated for the cross section σ (see below), while the column density of the dust grains N_d was normalized to the cross section with an area of 1 cm^2.

As an example, Fig. 4 shows plots of N against ϕ for one of the models under consideration. Integer phases correspond to the time of periastron passage by the secondary. The calculations were performed for different inclinations of the orbital plane θ and different orbital orientations relative to the observer. The column cross section σ was taken to be $0.1a \times 0.2a$. Test calculations show that the statistical fluctuations attributable to the small number of test particles in the column increase at lower values of σ, while at higher values of σ the features in the light curves are smoothed out.

The Amplitudes and Shapes of the Light Curves

In calculating the fadings of a binary system caused by extinction variations along the line of sight, we assumed that the main radiation source is the primary, which was treated in our calculations as a point source. The flux from the primary is attenuated by a factor of $e^{-\tau}$ as it passes through the dust component of the disk wind. At $\tau \gg 1$, when the direct radiation from the primary is severely attenuated, the flux is determined by the scattered radiation from the circumstellar dust, which includes the scattered radiation from the circumstellar and CB disks and from the common envelope. Thus,

$$F_{obs} = \frac{L_*}{4\pi D^2} e^{-\tau} + F_{sc}, \qquad (5)$$

where D is the distance to the observer.

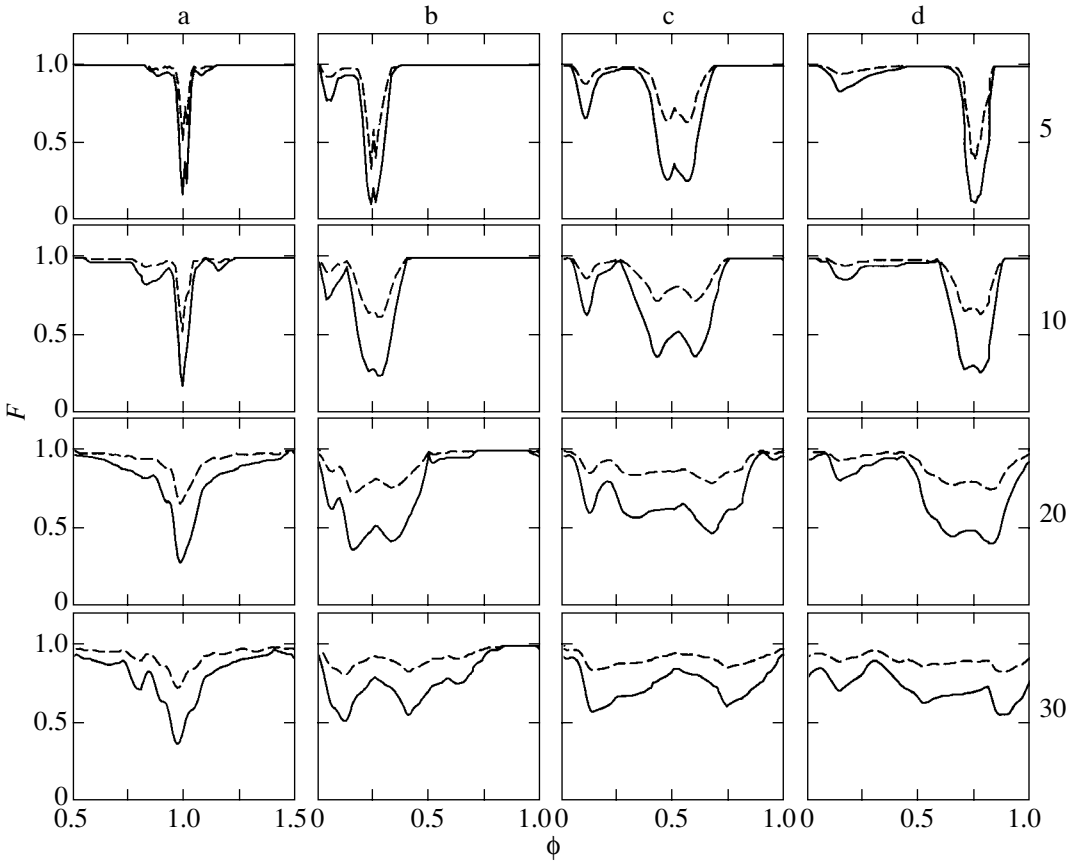

Fig. 5. Theoretical light curves for the primary component of the binary for the orbital orientations shown in Fig. 3. The model parameters are $e = 0.5$, $V_w = 1$, $U_w = 0$; the outflow rate of the disk wind from the low-mass component $\dot{M}_w = 10^{-8} M_\odot$ yr^{-1} (solid line) and $3 \times 10^{-9} M_\odot$ yr^{-1} (dashed line). The angle θ between the line of sight and the plane of the binary is indicated on the right.

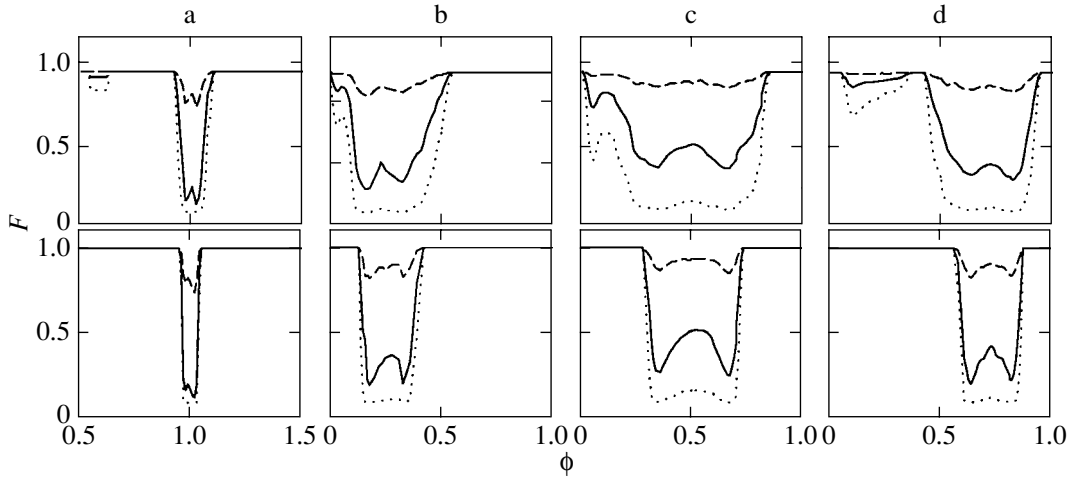

Fig. 6. Light curves for the model with $V_w = 2$, $U_w = 0$, $e = 0.5$ at the outflow rate $\dot{M}_w = 3 \times 10^{-9} M_\odot$ yr^{-1} (dashed line), 3×10^{-8} (solid line), and $3 \times 10^{-7} M_\odot$ yr^{-1} (dotted line). The angle $\theta = 20°$. Top: $40° < \omega < 60°$; bottom: $\omega = 45°$.

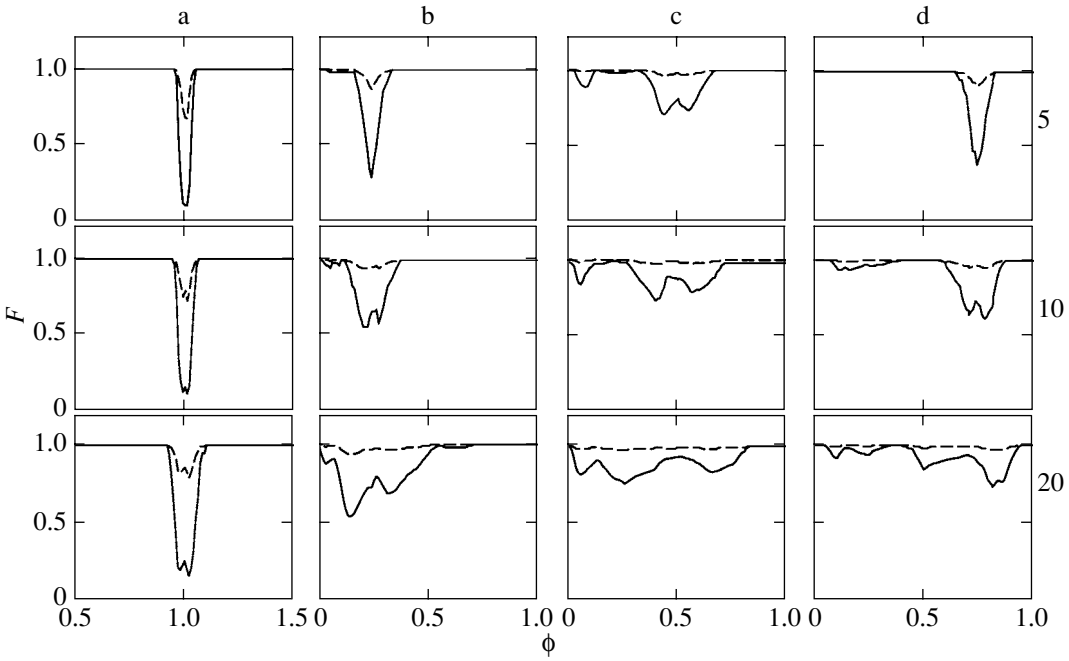

Fig. 7. Light curves for the model with a variable outflow rate ($\dot{M}_w \propto \dot{M}_a$). The solid and dashed lines correspond to outflow rates at the periastron of $\dot{M}_w = 3 \times 10^{-8} M_\odot$ and $3 \times 10^{-9} M_\odot$ yr^{-1}, respectively. The model parameters are: $V_w = 2$, $U_w = 0$, $e = 0.5$. The angle θ between the line of sight and the plane of the binary is indicated on the right.

In general, the scattered light contributes only slightly to the direct radiation from the young star, and its main function is to limit the amplitude of the minima in the cases where the direct stellar radiation is severely attenuated by absorption in the circumstellar medium. Such limiting functions of the scattered radiation from the circumstellar disks of young stars are well known for UX Ori stars, which undergo dramatic fadings due to variable circumstellar extinction (Grinin 1988).

Figures 5–7 show a family of light curves computed for several binary models. For simplicity, the scattered flux is assumed to be independent of the orbital phase and equal to $0.1F_*$. The computations were performed for the wavelength of 5500 Å that corresponds to the maximum of the V passband.

As in the models of binaries with circular orbits (Grinin and Tambovtseva 2002), the light curves in Figs. 5–7 have an asymmetric two-component shape due to the conical structure of the disk wind. At certain orientations of the binary, the two-component shape of the minima does not show up because of the low resolution attributable to the column cross section σ assumed in our calculations for which $N(\phi)$ was calculated. Since the stellar disk of the primary is finite in size, such a smoothing of the light curves is also possible in actual situations.

We see from Figs. 5–7 that, other things being equal, the longest minima are observed in binaries whose eclipses occur at the time of apoastron passage by the companion and, conversely, the eclipses are shortest when the binary is observed from the periastron. It is easy to show that the ratio of the eclipse durations at these two opposite orientations of the binary is

$$\Delta t_a / \Delta t_p = (1 + e)/(1 - e). \quad (6)$$

It thus follows that the eclipse durations at $e = 0.5$ differ by a factor of 3.

In most of the models considered for orbital orientation b (Fig. 3), when an eclipse occurs after the periastron passage by the secondary, the light curve is characterized by a steep fall and a slow rise, while in the same models, but for orbital orientation d (an eclipse occurs before the periastron passage), the reverse pattern is observed: the fall in brightness is slower than its rise.

At small orbital inclinations, the eclipse duration is short compared to the orbital period. The binaries whose apoastron is oriented toward the observer (case c in Figs. 5–7) constitute an exception: in such cases, an eclipse can last for a long time even at small θ. The eclipse duration increases with orbital inclination and can be comparable to the binary period at $\theta \geq 30°$.

As we see from Fig. 5, in addition to the primary minimum, a weaker minimum that precedes the primary one is observed in the models with low velocities

of the disk wind. There is also a similar peculiarity in the models with circular orbits. As was shown previously (Grinin and Tambovtseva 2002), it owes its origin to the wind particles ejected during the preceding passage of the secondary in the orbit and captured by the primary. In the models with high mass loss rates ($\dot{M}_{\rm w} \geq 10^{-7} M_\odot$ yr^{-1}) and large orbital inclinations, the boundary between the primary minimum and its predecessor disappears, which gives rise to a more extended two-component structure of the minima. In the models with a higher wind velocity (Fig. 6), the fraction of the matter captured by the primary decreases. As a result, only one primary minimum remains in the light curve.

Our calculations show that allowing for the rotation of the disk wind leads to a faster horizontal wind expansion than that in the models with $U_{\rm w} = 0$. As a result, the depth of the minima decreases and their duration increases (Grinin and Tambovtseva 2003). The parameters of the minima and their shapes also depend on the geometry of the disk wind. Figure 6 shows the results of our calculations for two wind models. These differ only by the wind opening angle: in one case, it is the same as that in Fig. 5 ($40^\circ \leq \omega \leq 60^\circ$; in the other, the outflow takes place at an angle of 45°. We see that, in the latter case, the minima are shorter and more symmetric in shape.

Recall that all the models presented above were computed by assuming the outflow rate to be constant. For comparison, we also considered the model with a variable outflow rate $\dot{M}_{\rm w} \propto \dot{M}_{\rm a}$ in which the dependence of $\dot{M}_{\rm a}$ on ϕ was taken from the paper by Artymowicz and Lubow (1996). Our calculations show (Fig. 7) that the amplitude of the minima in the models with a variable $\dot{M}_{\rm w}$ depends on the orbital orientation of the secondary component in the binary relative to the observer (which is quite natural): it is at a maximum in binaries whose periastron lies between the observer and the primary (case a in Fig. 3) and at a minimum for the opposite orbital orientation (case c in Fig. 3). As regards the shape of the light curves, the difference between these two models proves to be insignificant.

Modulation of the Scattered Radiation with Orbital Phase

When computing the light curves, we assumed, for simplicity, that the intensity of the scattered radiation did not depend on the orbital phase. This situation is possible if the CB disk is the main source of scattered radiation. In our case, part of the scattered radiation originates in the disk wind from the secondary and the common envelope produced by it, and this part is subject to periodic modulation. As an example, let us consider how the phase dependence of the scattered radiation can be reflected in the light curves of a binary system.

To this end, we calculated the intensity of the scattered radiation in the single-scattering approximation for two of the models considered above (as our analysis indicates, the single-scattering approximation holds for the bulk of the common envelope at $\dot{M}_{\rm w} \leq 10^{-8} M_\odot$ yr^{-1}). The scattered flux in this approximation is

$$F_{\rm sc} = \frac{L_*}{4\pi D^2} \pi s^2 Q_{\rm sc} \int\limits_V n(\mathbf{r}) r^{-2} f(\gamma) e^{-\tau_1 - \tau_2} d\mathbf{r}. \quad (7)$$

Here, $n(\mathbf{r})$ is the particle number density in 1 cm^3 at point $\mathbf{r}$, $Q_{\rm sc}$ is the particle scattering efficiency, s is the particle radius, τ_1 is the optical distance between point $\mathbf{r}$ and the primary, and τ_2 is the optical distance between point $\mathbf{r}$ and the observer. The integration in (7) is over the entire volume V of the common envelope.

As in the previous section, we assumed in our calculations that the dust grains consisted of a mixture of graphite and astrosilicate particles $s = 0.1$ μm in radius with the same content. The scattering process is described by the Henyey–Greenstein phase function

$$f(\gamma) = \frac{1}{4\pi} \frac{1 - g^2}{(1 + g^2 - 2g\cos\gamma)^{3/2}}, \quad (8)$$

where γ is the scattering angle, and the asymmetry factor g is taken to be 0.5.

The results of our calculations for two orientations of the binary, nearly edge-on ($\theta = 5^\circ$) and pole-on, are shown in Fig. 8a. In both cases, an integer phase ϕ corresponds to the time of periastron passage by the low-mass component. In the former case, the periastron lies between the primary and the observer. We see that the scattered flux $F_{\rm sc}$ reaches its maximum precisely at this phase. When the binary is seen edge-on, this occurs due to the forward-elongated phase function. In contrast, when the binary is seen pole-on, the maximum of $F_{\rm sc}$ is reached, because the dilution factor weighted over the entire envelope reaches its maximum at the time of periastron passage by the low-mass component.

As we see from Fig. 8a, the dependence of $F_{\rm sc}$ on the orbital phase is asymmetric and exhibits a steep rise as the companion approaches the periastron and a slower fall as it recedes from the periastron. Our calculations show that the degree of asymmetry depends on both the dimensionless velocity of the disk wind $V_{\rm w}$ and the orbital eccentricity e and inclination to the line of sight. In the model considered above (Fig. 8a), $F_{\rm sc}$ is most asymmetric when the binary is seen pole-on.

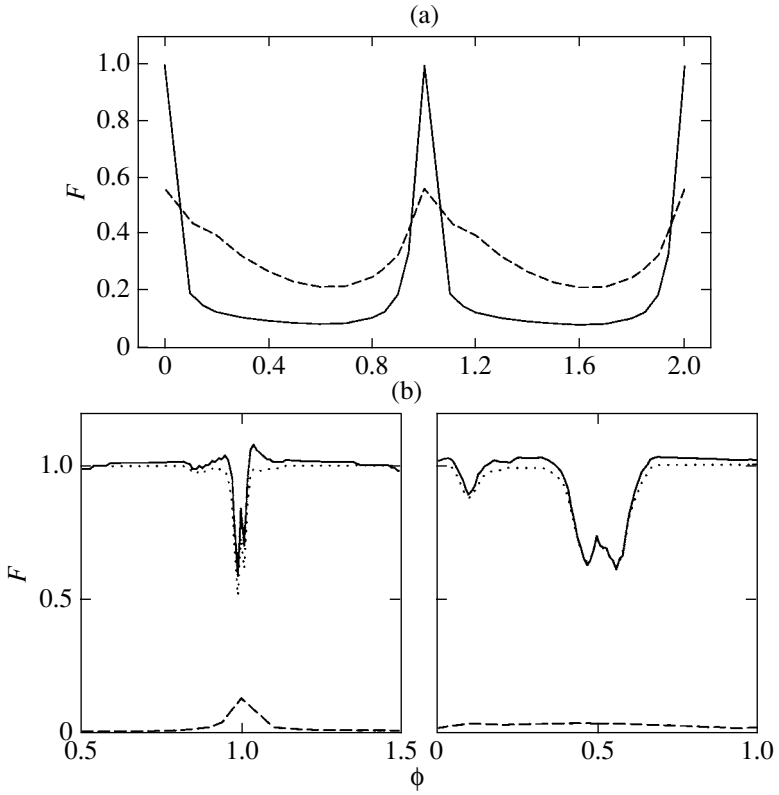

Fig. 8. (a) Phase dependence of the scattered radiation for two orientations of the binary: $\theta = 5^\circ$ (solid line) and $\theta = 90^\circ$ (dashed line). The model parameters are: $e = 0.5$, $V_w = 1$, $U_w = 0$. (b) A model of the eclipse of the primary component in the binary with an allowance made for the phase dependence of the scattered radiation for the same parameters: at periastron (left panel) and apoastron (right panel); the dotted lines represent the light curves without scattered radiation, and the dashed line represents the scattered flux.

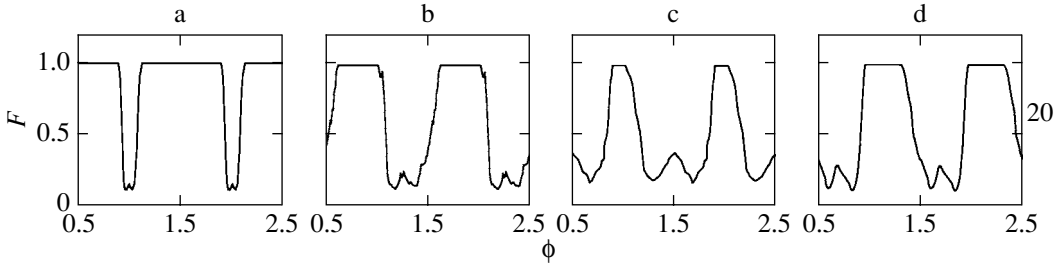

Fig. 9. Light curves for the model with $V_w = 3$, $U_w = 0.5$, $e = 0.5$ at the outflow rate $\dot{M}_w = 10^{-7} M_\odot$ yr^{-1} and $\theta = 20^\circ$.

The ϕ dependences of F_{sc} shown in Fig. 8 were computed for the model with $\dot{M}_w = \text{const}$. In the models with $\dot{M}_w \propto \dot{M}_a$, the overall pattern remains qualitatively the same. As in the previous case, the scattered radiation reaches its maximum at the periastron of the orbit and has an even larger amplitude.

If we use the values of F_{sc} in Eq. (5) calculated above, then asymmetric low-amplitude brightenings appear in the light curves during ingress and (or) egress (Fig. 8b). Such features are occasionally observed in the light curves of young eclipsing objects (see, e.g., Gürtler *et al.* 1999; Herbst *et al.* 2002) and can result from the scattering of the radiation from the primary by dust grains with a forward-elongated phase function. It is also clear that an allowance for the phase dependence of the scattered light can lead to a brightening in the central part of deep minima whose amplitude is limited below by the scattered radiation.

FUOR-Like Light Curves

As our calculations show, in the models with a high outflow rate, the common envelope produced by

the disk wind from the secondary component can be so thick that the primary component of the binary can be obscured from the observer during an appreciable part of the orbital cycle. In such cases, the light curve has a pattern of successive outbursts that are actually short time intervals corresponding to minimum extinction on the line of sight (Fig. 9).

This result can be of interest in connection with the ongoing discussion about the nature of FUOR outbursts (see Herbig *et al.* (2003) and references therein). According to Hartmann and Kenyon (1985), the outbursts of these objects are caused by recurrent enhancements of the accretion rate onto the young star, causing the luminosity of the accretion disk to increase sharply, which is associated with a FUOR outburst. According to another hypothesis (Herbig *et al.* 2003), the FUOR outbursts are caused by luminosity variations in the stars themselves. The two hypotheses are not free from difficulties. Therefore, it is of interest to consider the possibility of interpreting the light curves of certain FUORs as an alternative on the basis of the model for a young binary system in which the primary, a high-luminosity star, is periodically shielded by the gas and dust envelope produced by the disk wind from the secondary.

DISCUSSION

Thus, the theoretical light curves of young binaries in which the primary is eclipsed by the disk wind from the secondary exhibit a wide variety of shapes and, in many cases, bear no resemblance whatsoever to the classical light curves that are observed for ordinary eclipsing binary stars. At a mass loss rate of the accretion disk around the secondary $\dot{M}_{\rm w} \geq 3 \times 10^{-8}$, eclipses can be observed even if its orbital plane is highly inclined to the line of sight. The duration of such eclipses can be comparable to the orbital period. Given this and the high frequency of occurrence of binary and multiple systems among young stars (see the review by Mathieu *et al.* 2000), one might expect the existence of large-scale cyclic brightness variability in many young stars. Therefore, the several recently discovered young eclipsing systems with long-lasting eclipses may be assumed to be actually a widespread population of young stars whose number will increase rapidly as the photometric observations of young clusters are accumulated. We suggest that the UX Ori stars, whose cyclic activity was interpreted in terms of the binary nature of young stars by Grinin *et al.* (1998), Rostopchina *et al.* (1999), and Bertout (2000), belong to these eclipsing systems.

Another peculiarity of the eclipse model considered here that should be taken into account when analyzing long series of photometric observations of young stars is as follows. As was noted above, the CB disk in binary systems with eccentric orbits exhibits a global asymmetry (Fig. 1) and slowly precesses. When such systems are viewed at a small angle to their equatorial plane, slow (secular) variations in the extinction and, hence, the brightness of the primary must be observed. The situation where the direct radiation from the binary components will be completely obscured by the CB disk during a certain period is theoretically possible. In addition, the orbits of the binary components must also slowly precess under the influence of tidal interactions with the CB disk. This implies that in the eclipse models considered above (Figs. 5–7), a gradual transition from eclipse scenario a to scenario b etc. must occur, which must cause slow variations in the parameters of the minima: their depth, duration, and shape.

The exotic eclipsing system KH 15D, whose binary nature has recently been established by Johnson *et al.* (2004) from the radial-velocity variations of the primary and whose eccentricity was estimated ($0.68 \leq e \leq 0.80$), may belong to these objects. Analysis of archival photographic observations indicates (Johnson and Winn 2004) that the brightness of KH 15D has slowly decreased over the last forty years (see also Barsunova *et al.* 2004). The eclipse parameters, their durations (Herbst *et al.* 2002) and depths (Johnson and Winn 2004), also vary slowly. According to the Harvard College Observatory collection of photographic observations, the eclipse duration for KH 15D in the early 20th century was much shorter than that at the current epoch (Winn *et al.* 2003). The model of eclipses by the disk wind can account for all these peculiarities, provided that the orbit of the secondary is highly eccentric and precesses.

Another possible application of the eclipse model considered here is the interpretation of the large-scale photometric activity of certain candidate FUORs. Analysis of published photometry for such objects as V1515 Cyg (Hartmann *et al.* 1993) and Z CMa (van den Ancker *et al.* 2004) indicates that their light curves resemble some of the theoretical light curves for binary systems shown in Figs. 5–7. Given this and the fact that some FUORs are binary components, the possibility of large (in amplitude) variations in their brightness due to the cyclic extinction variations on the line of sight seems quite realistic and deserves further study.[4]

As we made sure above, the phase dependence of the scattered radiation can give rise to fine features in

[4]Note that the role of the binary nature of FUORs was previously discussed by Bonnel and Bastien (1992) in connection with the possibility of a periodic enhancement of the accretion rate onto the primary component of the binary that, in the opinion of these authors, trigger the outbursts of these objects.

the light curves: a small (in amplitude) brightening during ingress and (or) egress. More importantly, however, the orbital motion of the densest part of the common envelope must cause periodic modulation of both the intrinsic polarization of the young binary and its infrared excess; this modulation can be observed at any orientation of the binary relative to the observer. This opens up the possibility of discovering close binary systems whose orbital planes are close to the plane of the sky and which, for this reason, are difficult to discover by other methods.

To conclude, it should be noted that one of the assumptions made above to simplify the calculations is that the disk wind from the primary affects only slightly the structure of the common envelope. This approach is justified in the binary model considered above, in which the secondary is the main accretor and, hence, the main source of matter that produces the common envelope. However, even under these conditions, the role of the disk wind from the primary may prove to be significant when studying the cyclic activity of the binary in other wavelength ranges and, primarily, in the X-ray range. Indeed, as our estimates show, the collision between the two disk winds at a relatively low outflow rate of $\sim 10^{-9} M_\odot$ yr^{-1} and a velocity of 100 km s^{-1} is equivalent to energy release of $\sim 3 \times 10^{30}$ erg s^{-1}. It is comparable to the X-ray luminosities of many young stars (see the review by Glassgold *et al.* 2000), and it should be taken into account when interpreting the X-ray radiation from young objects.

CONCLUSIONS

The results presented above show that the behavior of the optical parameters of young binary systems with eccentric orbits depends significantly on how the following two main processes are related to each other: the accretion of matter from the CB disk onto the binary components and the outflow of matter from their surrounding accretion disks. Therefore, a key problem in the physics of young binary stars is the self-consistent solution of the problem in which these two processes are closely related. In particular, it is important to elucidate the role of tidal interactions in the formation of disk winds from the binary components and to determine the phase dependence of the rate of mass outflow from the accretion disk around the secondary.

ACKNOWLEDGMENTS

We wish to thank P. Artymowicz for his helpful discussion of the issues touched on in this paper and S.A. Lamzin who read the manuscript and made several valuable remarks. This work was supported by a grant from the Presidium of the Russian Academy of Sciences, "Nonstationary Phenomena in Astronomy," INTAS grant no. 03-51-6311, and grant no. NSh-1088.2003.2.

REFERENCES

1. M. van den Ancker, P. F. C. Blondel, H. R. E. Tjin, *et al.*, astro-ph/0401338 (2004).
2. P. Artymowicz and S. H. Lubow, Astrophys. J. **421**, 651 (1994).
3. P. Artymowicz and S. H. Lubow, Astrophys. J. **467**, L77 (1996).
4. O. Yu. Barsunova, V. P. Grinin, and S. A. Sergeev (in press).
5. M. R. Bate and I. A. Bonnell, Mon. Not. R. Astron. Soc. **285**, 33 (1997).
6. C. Bertout, Astron. Astrophys. **363**, 984 (2000).
7. D. V. Bisikalo, A. A. Boyarchuk, O. A. Kuznetsov, *et al.*, Astron. Zh. **72**, 190 (1995) [Astron. Rep. **39**, 167 (1995)].
8. I. A. Bonnel and P. Bastien, Astrophys. J. **401**, L31 (1992).
9. R. E. Cohen, W. Herbst, and E. C. Willams, astro-ph/0308484 (2003).
10. A. Duquennoy and M. Mayor, Astron. Astrophys. **248**, 485 (1991).
11. A. E. Glassgold, E. D. Feigelson, and T. Montmerle, *Protostars and Planets IV,* Ed. by V. Mannings, A. P. Boss, and S. S. Russel (Univ. of Arizona Press, Tucson, 2000), p. 429.
12. A. P. Goodson, K.-H. Böhm, and R. Winglee, Astrophys. J. **524**, 142 (1999).
13. V. P. Grinin, Pis'ma Astron. Zh. **14**, 65 (1988) [Sov. Astron. Lett. **14**, 27 (1988)].
14. V. P. Grinin, Astron. Zh. **79**, 422 (2002) [Astron. Rep. **46**, 380 (2002)].
15. V. P. Grinin, A. N. Rostopchina, and D. N. Shakhovskoĭ, Pis'ma Astron. Zh. **24**, 925 (1998) [Astron. Lett. **24**, 802 (1998)].
16. V. P. Grinin and L. V. Tambovtseva, Pis'ma Astron. Zh. **28**, 667 (2002) [Astron. Lett. **28**, 601 (2002)].
17. V. P. Grinin and L. V. Tambovtseva, *Towards Other Earths: DARWIN/TFP and the Search for Extrasolar Terresrial Planets,* Ed. by M. Fridlund and T. Henning (ESA SP-539, 2003), p. 429.
18. J. Gürtler, C. Friedemann, H.-G. Reimann, *et al.*, Astron. Astrophys. Suppl. **140**, 293 (1999).
19. P. Hartigan, S. E. Edwards, and L. Ghandour, Astrophys. J. **452**, 736 (1995).
20. L. Hartmann and S. J. Kenyon, Astrophys. J. **299**, 462 (1985).
21. L. Hartmann, S. Kenyon, and P. Hartigan, *Protostars and Planets III*, Ed. by E. H. Levy and J. I. Lunine (Univ. of Arizona Press, Tucson, 1993), p. 497.
22. G. H. Herbig, P. P. Petrov, and R. Duemmler, Astrophys. J. **595**, 384 (2003).
23. W. Herbst, C. M. Hamilton, F. Vrba, *et al.*, Publ. Astron. Soc. Pac. **114**, 1167 (2002).

24. L. Hernquist and H. Kats, Astrophys. J., Suppl. Ser. **70**, 419 (1989).
25. G. A. Hirth, R. Mundt, and J. Solf, Astron. Astrophys. Suppl. **126**, 437 (1997).
26. C. M. Hamilton, W. Herbst, C. Shih, and A. J. Ferro, Astrophys. J. **554**, L201 (2001).
27. N. Z. Ismailov, Astron. Zh. **80**, 231 (2003) [Astron. Rep. **47**, 206 (2003)].
28. J. A. Johnson, G. W. Marcy, C. M. Hamilton, *et al.*, astro-ph/0403099 (2004).
29. J. A. Johnson and J. N. Winn, astro-ph/0312428 (2004).
30. K. M. Kearns and W. Herbst, Astron. J. **116**, 261 (1998).
31. S. H. Lubow and P. Artimowicz, *Protostars and Planets IV,* Ed. by V. Mannings, A. P. Boss, and S. S. Russell (Univ. of Arizona Press, Tucson, 2000), p. 731.
32. M. Makita, K. Miyawaki, and T. Matsuda, Mon. Not. R. Astron. Soc. **316**, 906 (2000).
33. R. D. Mathieu, A. M. Ghez, E. K. N. Jensen, and M. Simon, *Protostars and Planets IV,* Ed. by V. Mannings, A. Boss, and S. S. Russell (Univ. of Arizona Press, Tucson, 2000), p. 559.
34. R. D. Mathieu, F. C. Adams, and D. W. Latham, Astron. J. **101**, 2184 (1991).
35. J. S. Mathis, W. Rumpl, and K. H. Nordsieck, Astrophys. J. **217**, 425 (1977).
36. M. Mayor and S. Urdy, ASP Conf. Ser. **219**, 441 (2000).
37. T. Mazeh, D. Goldberg, A. Duquennoy, and M. Mayor, Astrophys. J. **401**, 265 (1992).
38. A. Natta, V. P. Grinin, and V. Mannings, *Protostars and Planets IV,* Ed. by V. Mannings, A. Boss, and S. S. Russell (Univ. of Arizona Press, Tucson, 2000), p. 559.
39. M. A. Pogodin, A. S. Miroshnichenko, A. E. Tarasov, *et al.*, Astron. Astrophys. (2004, in press).
40. A. N. Rostopchina, V. P. Grinin, and D. N. Shakhovskoi, Pis'ma Astron. Zh. **25**, 291 (1999) [Astron. Lett. **25**, 243 (1999)].
41. M. Rožiczka and G. Laughlin, ASP Conf. Ser. **121**, 792 (1997).
42. P. N. Safier, Astrophys. J. **408**, 115 (1993).
43. K. Sawada, T. Matsuda, and I. Hachisu, Mon. Not. R. Astron. Soc. **219**, 75 (1986).
44. K. Sawada, T. Matsuda, and I. Hachisu, Mon. Not. R. Astron. Soc. **221**, 679 (1986).
45. N. I. Shakura and R. A. Sunyaev, Astron. Astrophys. **24**, 337 (1973).
46. V. S. Shevchenko, K. N. Grankin, S. Yu. Mel'nikov, and S. A. Lamzin, Pis'ma Astron. Zh. **24**, 614 (1998) [Astron. Lett. **24**, 528 (1998)].
47. J. M. Stone, C. F. Gammie, S. A. Balbus, and J. F. Hawley, *Protostars and Planets IV*, Ed. by V. Mannings, A. Boss, and S. S. Russell (Univ. of Arizona Press, Tucson, 2000), p. 589.
48. J. N. Winn, P. M. Garnavich, K. Z. Stanek, and D. D. Sasselov, Astrophys. J. **593**, L121 (2003).

Translated by V. Astakhov

Astronomy Letters, Vol. 30, No. 10, 2004, pp. 707–714. Translated from Pis'ma v Astronomicheskiĭ Zhurnal, Vol. 30, No. 10, 2004, pp. 778–786.

Radial Pulsations of Helium Stars with Masses from 10 to $50M_\odot$

Yu. A. Fadeyev* **and M. F. Novikova**

Institute of Astronomy, Russian Academy of Sciences, Pyatnitskaya ul. 48, Moscow, 119017 Russia

Received March 20, 2004

Abstract—We have performed hydrodynamic calculations of the radial pulsations of helium stars with masses $10M_\odot \le M \le 50M_\odot$, luminosity-to-mass ratios $5\times10^3 L_\odot/M_\odot \le L/M \le 2.5\times10^4 L_\odot/M_\odot$, and effective temperatures 2×10^4 K $\le T_{\rm eff} \le 10^5$ K for helium and heavy-element mass fractions of $Y = 0.98$ and $Z = 0.02$, respectively. We show that the high-temperature boundary of the instability region for radial pulsations at $L/M \gtrsim 10^4 L_\odot/M_\odot$ extends to $T_{\rm eff} \sim 10^5$ K. The amplitude of the velocity variations for outer layers is several hundred km s^{-1}, while the brightness variations in the B band of the UBV photometric system are within the range from several hundredths to half a magnitude. At constant luminosity-to-mass ratio, the radial pulsation period is determined only by the effective temperature of the star. In the ranges of luminosity-to-mass ratios $10^4 L_\odot/M_\odot \le L/M \le 2\times10^4 L_\odot/M_\odot$ and effective temperatures 5×10^4 K $\le T_{\rm eff} \le 9\times10^4$ K, the periods of the radial modes are within 6 min $\lesssim \Pi \lesssim 10^3$ min.
© *2004 MAIK "Nauka/Interperiodica".*

Key words: *stars—variable and peculiar, stellar pulsations, helium stars, Wolf–Rayet stars.*

INTRODUCTION

Among the many types of photometric and spectroscopic variability of Wolf–Rayet stars, the cyclic brightness and radial-velocity variations unrelated to the orbital motion in a close binary are of great interest. It is assumed that, apart from the effects of axial rotation and nonstationary stellar wind, stellar pulsations could be responsible for the cyclic brightness variations. The amount of data indicative of the pulsational variability of Wolf–Rayet stars has increased rapidly over the last two decades owing to spectroscopic (Vreux 1985; Vreux *et al.* 1985; Morel *et al.* 1998; Veen *et al.* 2002b) and photometric (Moffat and Shara 1986; van Genderen *et al.* 1987; Gosset *et al.* 1989; Balona *et al.* 1989; Blecha *et al.* 1992; Antokhin *et al.* 1995; Bratschi and Blecha 1996; Veen *et al.* 2002a) studies. Moreover, the irregular variations in the radial-velocity amplitude of WR 46 (Marchenko *et al.* 2000) can be naturally explained only by assuming this star to be pulsationally unstable (Veen *et al.* 2002a–2002c). Unfortunately, the detection of pulsational variability of Wolf–Rayet stars is severely complicated by the optically thick stellar wind that hides the stellar photosphere from the observer. It is for this reason that reports on pulsational variability have appeared only comparatively recently, and that the interpretation of observations is occasionally controversial. For example, the detection of pulsations with a period of 627 s in the star WR 40 (Blecha *et al.* 1992) has not been confirmed by more recent observations (Bratsci and Blecha 1996).

Despite the significant difficulties involved in detecting pulsational variability, the theory of stellar pulsations strongly suggests that this type of instability exists in Wolf–Rayet stars. Calculations of stellar pulsations in the linear approximation show that massive, high-luminosity helium stars can be unstable relative to radial and nonradial modes over wide ranges of masses M, luminosities L, and effective temperatures $T_{\rm eff}$ (Glatzel *et al.* 1993; Kiriakidis *et al.* 1996; Glatzel and Kaltschmidt 2002). Moreover, for radial modes, the nonlinear theory predicts high instability growth rates and large amplitudes of the motion of the outer layers at which the expansion velocity is comparable to the local escape velocity (Glatzel *et al.* 1999), and the dynamic scale height is larger than the static scale height by more than an order of magnitude (Fadeyev and Novikova 2003). Thus, a detailed analysis of the pulsational instability seems necessary to gain a fuller understanding of the physical nature of the mass outflow from Wolf–Rayet stars.

In this paper, we discuss our hydrodynamic calculations of the radial pulsations of helium stars with masses $10M_\odot \le M \le 50M_\odot$ for helium and heavy-element mass fractions of $Y = 0.98$ and $Z = 0.02$, respectively. The grid of hydrodynamic models computed here complements our previous calculations

*E-mail: fadeyev@inasan.rssi.ru

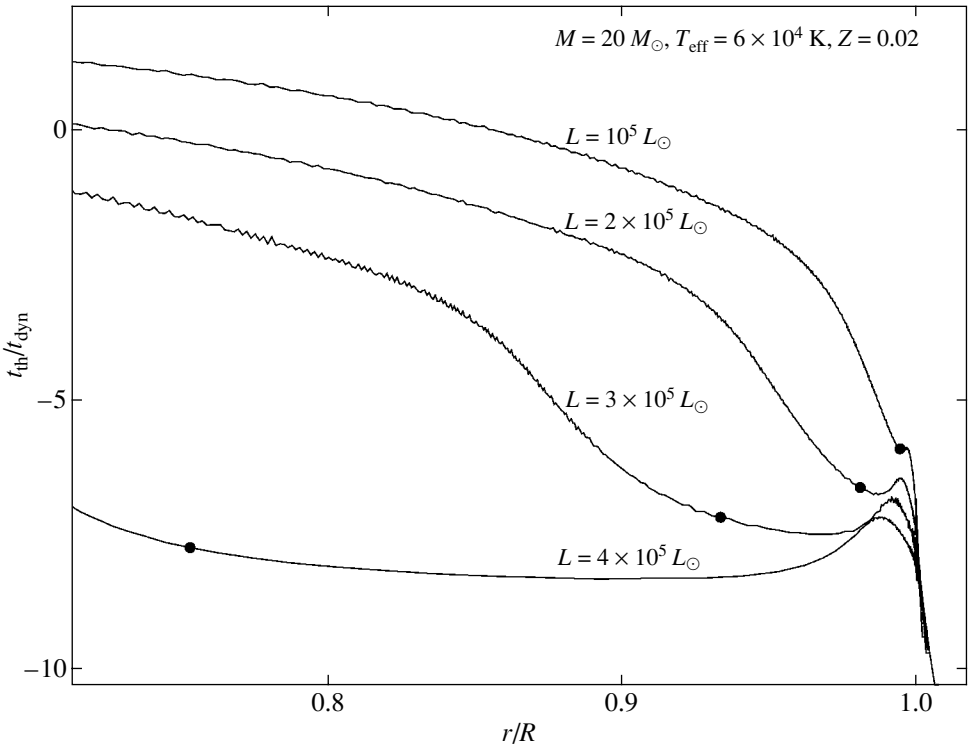

Fig. 1. Ratio of the thermal time scale $t_{\rm th}$ to the dynamic time scale $t_{\rm dyn}$ versus radial distance r for helium stars with a mass of $M = 20M_\odot$, a luminosity of $10^5 L_\odot \le L \le 4 \times 10^5 L_\odot$, and an effective temperature of $T_{\rm eff} = 6 \times 10^4$ K. The filled circles indicate the location of the layer with a temperature of $T \approx 2 \times 10^5$ K. The radial distance from the center is measured in units of the equilibrium stellar radius R.

for helium stars with masses $1M_\odot \le M \le 10M_\odot$ (Fadeyev and Novikova 2003).

HYDRODYNAMIC MODELS

As in our previous paper (Fadeyev and Novikova 2003), we consider here the radial stellar pulsations that develop from a thermal and hydrostatic equilibrium state due to small initial hydrodynamic perturbations. We used the OPAL tables (Iglesias and Rogers 1996; Rogers *et al.* 1996) to compute the opacity and the equation of state. Since the radial pulsation amplitude decreases rapidly toward the stellar center, we carried out the hydrodynamic calculations for the outer gas layers (i.e., the stellar envelope) with a temperature of $T \lesssim 10^7$ K. When setting the inner boundary conditions, we assumed that the radius and luminosity at the bottom of the envelope did not vary with time: $\partial r_1/\partial t = \partial L_1/\partial t = 0$.

A characteristic feature of the envelopes of high-luminosity helium stars is the short thermal time scale $t_{\rm th} = 4\pi r^3 \rho C_{\rm p} T/L_r$ compared to the dynamic time scale $t_{\rm dyn} = \left(R^3/GM\right)^{1/2}$, where G is the gravitational constant, M and R are the stellar mass and radius, L_r, T, ρ, $C_{\rm p}$ are the luminosity, temperature, density, and specific heat of the gas at constant pressure in a layer of radius r. The assumption that the stellar pulsations are adiabatic is valid for $t_{\rm th}/t_{\rm dyn} \gg 1$. Figure 1 shows the radial dependences of the ratio $t_{\rm th}/t_{\rm dyn}$ for several models of helium stars with a mass of $M = 20M_\odot$. The low value of this ratio within the bulk of the stellar envelope indicates that the pulsations are essentially nonadiabatic and explain both the rapid instability growth at a rate of $\eta \sim 1$ and the large pulsation amplitude after the instability ceases to grow.

For strictly periodic stellar pulsations, the completion of the stage of an exponential increase in the amplitude is associated with the transition to limit-cycle self-oscillations, which can be analyzed by expanding the solution of the hydrodynamic equations into Fourier series (Fadeyev 1994). However, the maximum kinetic energy of the pulsating envelope and the period for helium stars after the amplitude ceases to increase change from cycle to cycle, although the mean maximum kinetic energy is constant in an extended time interval spanning many cycles. The deviations from the repetition of pulsations increase with decreasing $t_{\rm th}/t_{\rm dyn}$, *i.e.*, with increasing luminosity-to-mass ratio L/M.

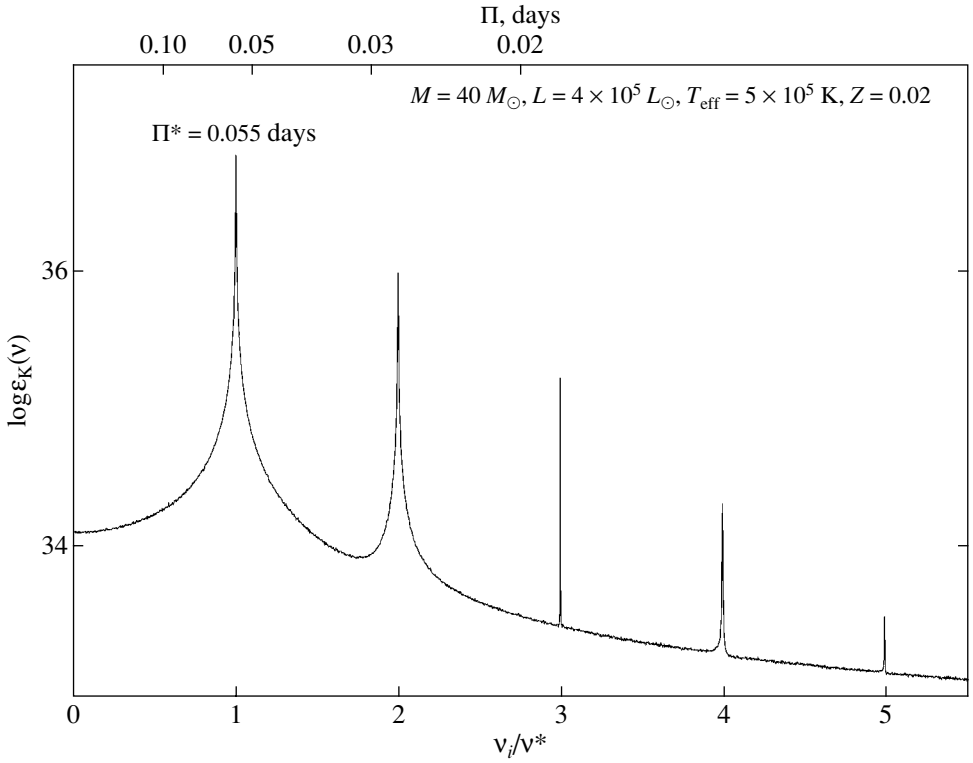

Fig. 2. Fourier spectrum of the kinetic energy for a radially pulsating helium star.

Taking into account the absence of a strict periodicity in the pulsations, we analyzed the hydrodynamic models of helium stars using the discrete Fourier transforms of the radius $r_j(t)$ and velocity $U_j(t)$ for each Lagrangian layer of the model with $2 \le j \le N$ in a time interval spanning ~300 fundamental oscillation cycles. For each hydrodynamic model at the stage of steady-state oscillations after the instability ceased to grow, we computed the Fourier spectra of the oscillator moment of inertia,

$$\mathcal{J}(\nu) = \sum_{j=2}^{N} |\mathcal{R}_j(\nu)|^2\, \Delta m_{j-1/2}, \qquad (1)$$

and the kinetic energy,

$$\mathcal{E}_{\rm K}(\nu) = \frac{1}{2} \sum_{j=2}^{N} |\mathcal{U}_j(\nu)|^2\, \Delta m_{j-1/2}, \qquad (2)$$

where $\mathcal{R}_j(\nu)$ and $\mathcal{U}_j(\nu)$ are the Fourier transforms of the radius and velocity of layer j, and $\Delta m_{j-1/2}$ is the mass of the Lagrangian interval between layers $(j-1)$ and j. We used $300 \le N \le 500$ Lagrangian layers to represent the hydrodynamic models. A larger number of layers was used in models with higher luminosity-to-mass ratios L/M characterized by larger pulsation amplitudes. For all of the initial equilibrium models, $\approx N/5$ Lagrangian layers were located in the outer, optically thin shells of the stellar envelope.

For small changes of the pulsation cycle length ($\delta\Pi/\Pi \lesssim 10^{-2}$), the Fourier spectra (1) and (2) are the sets of equidistant peaks that decrease as a power law, and the pulsation period is determined by the frequency of the largest peak: $\Pi^* = 1/\nu^*$ (Fig. 2). As with the Fourier expansion of a strictly periodic solution, the overtone order of the fundamental pulsation mode with period Π^* is determined by the number of nodes for the eigenfunction of the radial displacement and, for hydrodynamic models, is equal to the number of minima in the radial dependences of the amplitudes $|\mathcal{R}_j(\nu^*)|$ and $|\mathcal{U}_j(\nu^*)|$ between the inner and outer boundaries of the model. As the nonadiabaticity effects become stronger, the minima of the amplitude become less prominent for the outermost nodes, and the corresponding changes in the phase $\phi = \tan^{-1}(A/B)$, where A and B are the Fourier coefficient of order $k = 1$, exhibit lower values of $\partial\phi/\partial r$ near the node.

Figure 3 shows plots of the amplitude Δr and phase ϕ_r of the radial displacement for the outer layers of the envelope in a pulsating helium star with a mass of $M = 40 M_\odot$. For convenience, the radius r is given in units of the initial equilibrium stellar radius R, and the radial displacement is normalized to its value on the surface Δr_N. The plot of the

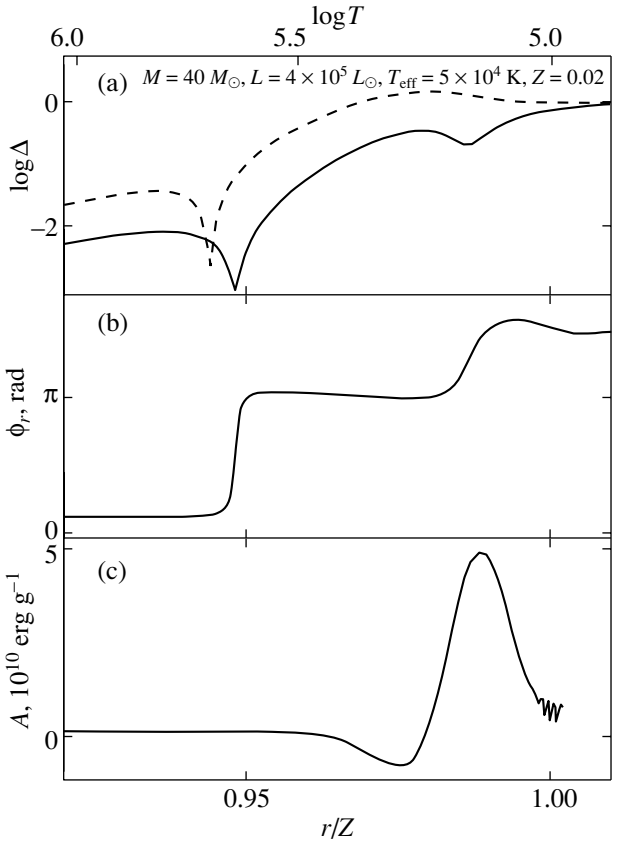

Fig. 3. (a) Normalized amplitudes of the radial displacement $\Delta r/\Delta r_N$ (solid line) and the luminosity variations $\Delta L_r/\Delta L_N$ (dashed line); (b) the radial displacement phase ϕ_r; (c) the mechanical work done by an elementary spherical layer during the pulsation cycle.

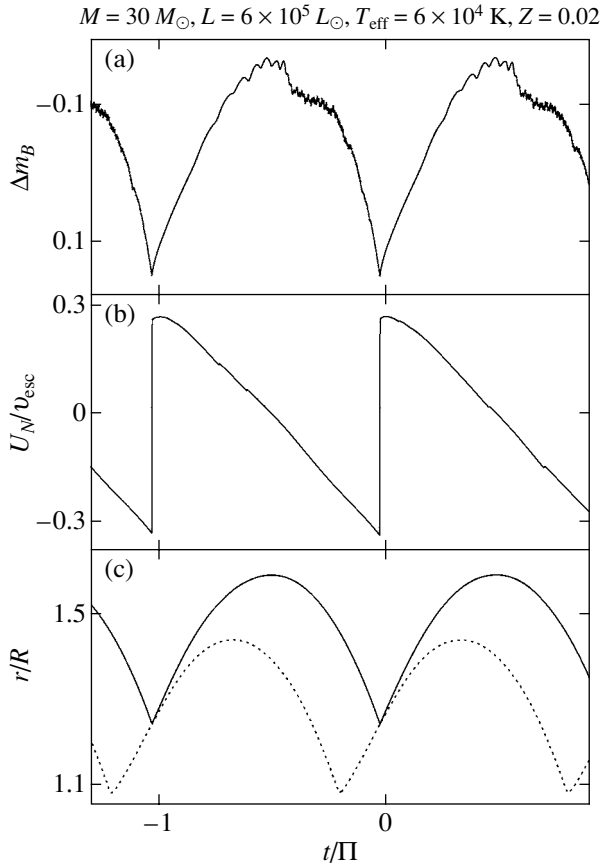

Fig. 4. Model of a helium star with $M = 30M_\odot$, $L = 6 \times 10^5 L_\odot$, and $T_{\rm eff} = 6 \times 10^4$ K at the stage of steady-state radial oscillations. (a) the B-band brightness variations; (b) the velocity of the outer boundary U_N in units of the local escape velocity $v_{\rm esc}$; (c) the radius of the outer boundary of the model r_N (solid line) and the photospheric radius $r_{\rm ph}$ (dotted line) in units of the initial equilibrium stellar radius R.

amplitude Δr has two minima, but only one of them ($r/R = 0.945$) is associated with the node of the standing wave, because the radial displacement phase ϕ_r rapidly changes by π radians only in this layer. The small depth of the outer minimum and the continuous increase in the phase ϕ_r with r near this minimum suggest the presence of a traveling component attributable to the pulsations being essentially nonadiabatic. The radial displacement phase difference between the inner and outer boundaries of the model is $\approx 1.4\pi$ radians. Thus, in contrast to classical pulsating variables (e.g., Cepheids), the radial pulsations of helium stars cannot be described in terms of standing-wave-type oscillations for which the phase difference between the stellar center and surface is a multiple of π radians.

Figure 3c shows a plot of the mechanical work $A = \oint PdV$ done by an elementary spherical layer during the closed pulsation cycle. Here, P is the total pressure, and $V = 1/\rho$ is the specific volume. A comparison with the plot of the amplitude of the radiative flux variations ΔL_r in Fig. 3a indicates that in layers with positive mechanical work, the amplitude of the luminosity variations decreases toward the surface: $\partial\left(\Delta L_r\right)/\partial r < 0$. This condition is necessary for the excitation of instability through the modulation of the radiative flux (see, e.g., Cox and Giuli 1968). Thus, this model clearly illustrates that the pulsations appear because of the gas opacity variations near the ionization zone of iron-group elements at a gas temperature of $T \sim 2 \times 10^5$ K.

The spread in mechanical work A at $r/R > 1$ is attributable to the nonlinearity effects and the deviations from periodicity in the outer layers of the stellar envelope. It should be noted that the curvilinear integral of the mechanical work can be calculated only for models with fairly good repetition of pulsations, i.e., for $L/M \lesssim 10^4 L_\odot/M_\odot$. Nevertheless, we can assert with confidence that the excitation of radial pulsations in stars with higher ratios L/M is also attributable to

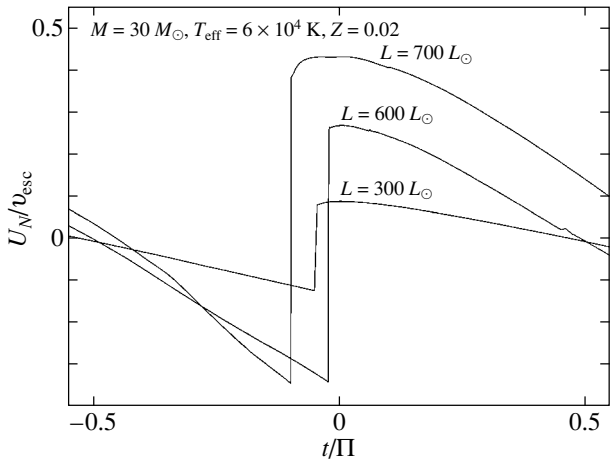

Fig. 5. Velocity of the outer boundary of the hydrodynamic model U_N, in units of the local escape velocity $v_{\rm esc}$, for the models of helium stars with a mass of $M = 30M_\odot$ and an effective temperature of $T_{\rm eff} = 6 \times 10^4$ K.

the modulation of the radiative flux in the ionization zone of iron-group elements, because layers in which $\partial(\Delta L_r)/\partial r < 0$ exist in the envelopes of such stars.

Figure 4 shows plots of the brightness variations m_B in the B band of the broadband UBV photometric system, the velocity of the outer boundary of the model U_N in units of the local escape velocity $v_{\rm esc}$, the radius of the outer boundary r_N, and the photospheric radius $r_{\rm ph}$. The zero time, $t = 0$, corresponds to the time the expansion velocity of the outer boundary reaches its maximum. The small oscillations in the light curve in Fig. 4a are attributable to the discreteness of the hydrodynamic model. As we see from Figs. 4a and 4 b, the brightness maximum and the maximum of the expansion velocity are spaced $\approx 1/2$ of the pulsation period apart. This peculiarity makes helium stars significantly different from classical pulsating variables in which the helium ionization zone causes the brightness maximum to be delayed from the maximum of the expansion velocity by $\approx 1/4$ of the period.

PULSATING HELIUM STARS IN THE HERTZSPRUNG–RUSSELL DIAGRAM

For a given stellar mass M and known elemental abundances, the pulsation period and amplitude are determined only by the luminosity L and effective temperature $T_{\rm eff}$. Here, we performed calculations for one chemical composition ($X = 0$, $Y = 0.98$, $Z = 0.02$). Therefore, combining the hydrodynamic models by mass M, we consider the basic parameters of radially pulsating helium stars as functions of their positions in the Hertzsprung–Russell (HR) diagram.

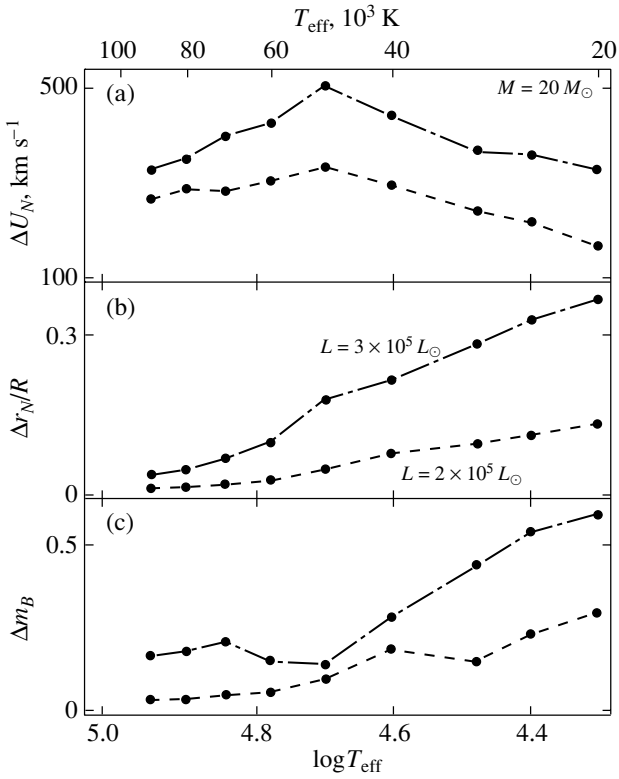

Fig. 6. Basic parameters of radially pulsating helium stars with a mass of $M = 20M_\odot$ and luminosities of $L = 2 \times 10^5 L_\odot$ (dashed lines) and $L = 3 \times 10^5 L_\odot$ (dot-dashed lines) versus effective stellar temperature $T_{\rm eff}$: (a) the velocity amplitude at the outer boundary of the model U_N; (b) the radial displacement amplitude at the outer boundary of the model Δr_N, in units of the equilibrium stellar radius R; (c) the amplitude of the brightness variations Δm_B.

We also use the luminosity-to-mass ratio, in solar units, to describe some of the properties of the models.

For helium stars with masses $1M_\odot \le M \le 50M_\odot$, the lower luminosity limit corresponding to the instability boundary of the radial modes is determined by the luminosity-to-mass ratio $L/M \sim 10^3 L_\odot/M_\odot$. Near this boundary, pulsations arise at effective temperatures $T_{\rm eff} \lesssim 3 \times 10^4$ K due to the instability of the fundamental mode. As the ratio L/M increases, the temperature boundary of the pulsational instability displaces toward higher $T_{\rm eff}$ and corresponds to $T_{\rm eff} \sim 10^5$ K for $L/M \approx 10^4 L_\odot/M_\odot$. The pulsations in the upper part of the instability region at $T_{\rm eff} \lesssim 4 \times 10^4$ K occur in the principal mode, while the fundamental pulsation mode at higher effective temperature is an overtone whose order increases with $T_{\rm eff}$.

The irregularity of the pulsations attributable to nonlinearity effects arises when the radial displacement amplitude of the outer boundary of the model is $\Delta r_N/R \gtrsim 1/2$. The pulsation amplitude increases

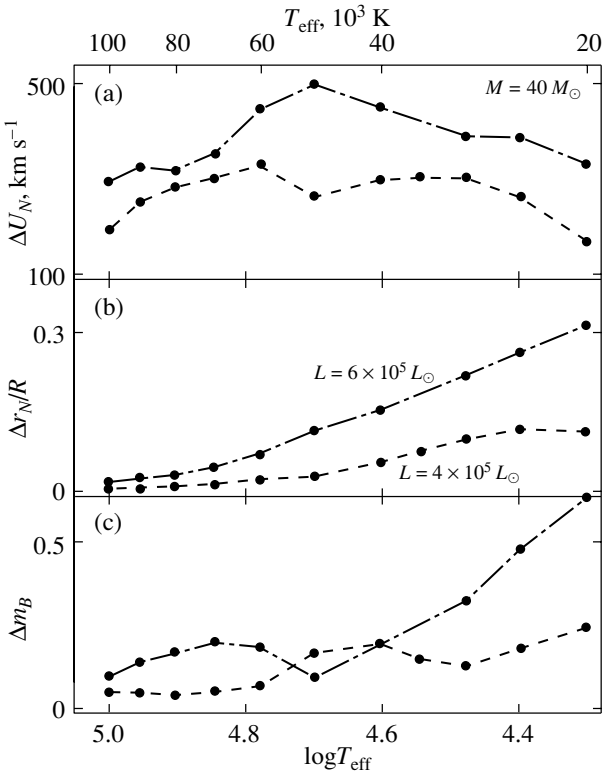

Fig. 7. Same as Fig. 6 but for helium stars with a mass of $M = 40M_\odot$.

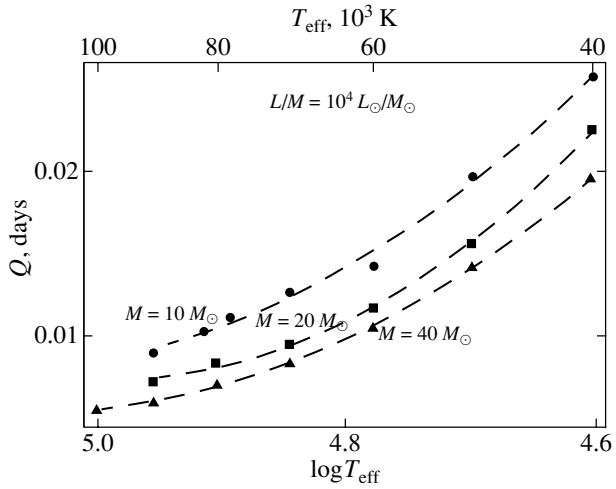

Fig. 8. Pulsation constant Q versus effective temperature for helium stars with masses of $M = 10M_\odot$ (circles), $M = 20M_\odot$ (squares), and $M = 40M_\odot$ (triangles); the dashed lines indicate the fits to Q.

with increasing luminosity-to-mass ratio and with decreasing effective temperature. In the range of effective temperatures 4×10^4 K $\lesssim T_{\rm eff} \lesssim 10^5$ K, the region of periodic oscillations (i.e., oscillations with period variations within two or three percent) is approximately determined by the condition $L/M \lesssim 1.5 \times 10^4 L_\odot/M_\odot$.

For $L/M > 10^4 L_\odot/M_\odot$, the increase in the luminosity-to-mass ratio is accompanied by the approach of the expansion velocity of the outer layers to the local escape velocity $v_{\rm esc}$. Figure 5 shows plots of the variations in the ratio $U_N/v_{\rm esc}$ during one pulsation cycle for several models of helium stars with a mass of $M = 30M_\odot$. For $L/M \approx 2.5 \times 10^4 L_\odot/M_\odot$, the maximum expansion velocity is approximately half of the local escape velocity, and the attempts to obtain solutions for models with higher luminosity-to-mass ratios proved to be unsuccessful. The reason is that due to the pulsation irregularity, the pulsation amplitude occasionally increases to an extent that the expansion velocity of the outer layers reaches the escape velocity, causing the outer Lagrangian layers of the model to be expanded indefinitely.

In Figs. 6 and 7, the amplitudes of the velocity of the model's outer boundary ΔU_N, the radial displacement Δr_N, in units of the equilibrium stellar radius R, and the brightness variations in the B band of the UBV photometric system Δm_B are plotted against the effective temperature $T_{\rm eff}$ for several models of helium stars with masses of $M = 20$ and $40M_\odot$. As we see from these plots, the velocity amplitude of the outer layers ΔU_N exhibits a distinct maximum at $T_{\rm eff} \approx 5 \times 10^4$ K, while the normalized radial displacement amplitude of the outer boundary $\Delta r_N/R$ monotonically decreases with increasing $T_{\rm eff}$. Such different variations in the velocity and radial displacement amplitudes of the model's outer boundary are attributable to an increase in the pulsation overtone order with increasing $T_{\rm eff}$ (Fadeyev and Novikova 2003).

Basic parameters for some of the hydrodynamic models are presented in the table. In this study, we used the approximation of radiative heat conduction to describe the radiative transfer and implicitly separated the shocks using artificial viscosity. Despite the overestimated radiative losses in shock waves (due to the approximation of radiative heat conduction, shock waves are considered in the isothermal approximation), our hydrodynamic calculations demonstrate the formation of an extended atmosphere with a slower decrease in the gas density than that in hydrostatic equilibrium. The last column of the table gives the mean radii of the outer boundary r_N, in units of the initial equilibrium stellar radius R. The appreciable increase in r_N/R with ratio L/M for $L/M > 10^4 L_\odot/M_\odot$ clearly illustrates the formation of an extended stellar atmosphere under the influence of periodic shock waves that accompany the nonlinear stellar pulsations.

Parameters of the hydrodynamic models for helium stars in the upper, high-temperature part of the pulsational instability region

$M/M_\odot$	$L/10^3 L_\odot$	$T_{\rm eff}/10^3$ K	Π, days	Q, days	$U_{\max}/v_{\rm esc}$	ΔU, km s^{-1}	$\Delta r/R$	Δm_B	$\bar{r}_N/R$
20	200	50	0.051	0.0155	0.12	330	0.05	0.10	1.03
20	200	70	0.011	0.0095	0.07	281	0.02	0.05	1.01
20	200	90	0.004	0.0072	0.05	263	0.01	0.03	1.00
20	300	50	0.155	0.0349	0.23	504	0.18	0.14	1.15
20	300	70	0.039	0.0242	0.11	395	0.07	0.21	1.05
20	300	90	0.015	0.0198	0.07	322	0.04	0.17	1.03
20	400	50	0.354	0.0644	0.40	648	0.49	0.43	1.37
20	400	70	0.137	0.0684	0.26	699	0.34	0.31	1.50
20	400	90	0.052	0.0553	0.17	632	0.19	0.35	1.27
40	400	50	0.055	0.0142	0.09	263	0.03	0.17	1.01
40	400	70	0.012	0.0084	0.07	301	0.01	0.05	1.01
40	400	90	0.004	0.0060	0.05	253	0.01	0.05	1.00
40	600	50	0.155	0.0294	0.18	499	0.12	0.09	1.07
40	600	70	0.040	0.0209	0.08	352	0.05	0.20	1.03
40	600	90	0.015	0.0166	0.06	324	0.02	0.14	1.02
40	800	50	0.431	0.0660	0.30	621	0.38	0.39	1.41
40	800	70	0.135	0.0568	0.24	830	0.29	0.28	1.34
40	800	90	0.058	0.0519	0.13	593	0.15	0.30	1.18

PULSATIONAL VARIABILITY TIME SCALES

Since the main and, in many cases, the only reliable observable of a pulsating star is the period of its brightness variations, the theoretically calculated pulsation periods are of primary interest for comparison with observations. Unfortunately, there are significant uncertainties in the observational estimates of the luminosities and effective temperatures for Wolf–Rayet stars, and instead of comparing theoretical models with specific stars, we can only determine the typical periods of the radial modes within a limited part of the HR diagram.

Theoretical models are compared with observations using the period–mean density relation

$$\Pi = Q\,(R/R_\odot)^{3/2}\,(M/M_\odot)^{-1/2}\,, \qquad (3)$$

where Q is the pulsation constant, a slowly changing function of the stellar mass, luminosity, and radius. The range of pulsation constants is narrow for a certain mode of radial standing-wave-type oscillations, while the transition of oscillations from one mode to another is accompanied by an abrupt change in Q. Because of the significant traveling component in the pulsation wave in helium stars, the change in the number of nodes along the radius is accompanied by a continuous change in Q. Therefore, the pulsation constant must be fitted for the entire range of effective temperatures under consideration.

In Fig. 8, Q is plotted against effective temperature for the models of helium stars with masses of $M = 10, 20$, and $40 M_\odot$ and $L/M = 10^4 L_\odot/M_\odot$. The pulsation constant in the range of effective temperatures 4×10^4 K $\le T_{\rm eff} \le 10^5$ K is fitted by a quadratic function of $\log T_{\rm eff}$ and a linear function of M. As

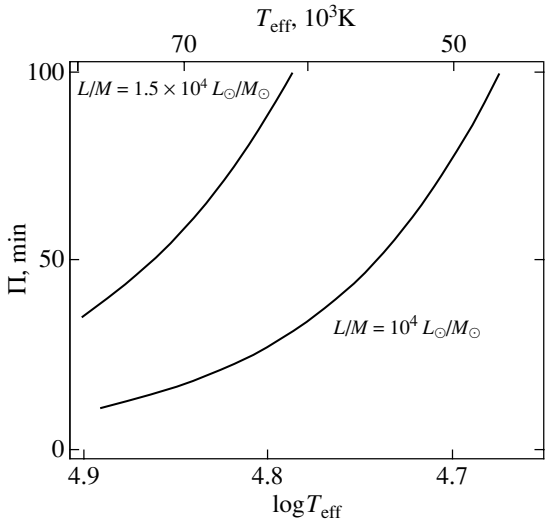

Fig. 9. Radial pulsation period for helium stars versus effective temperature for luminosity-to-mass ratios of $L/M = 10^4 L_\odot/M_\odot$ and $L/M = 1.5 \times 10^4 L_\odot/M_\odot$.

we see from Fig. 8, the fitting uncertainty is within the scatter of data points attributable to the absence of strict pulsation periodicity. Expressing the stellar radius R in terms of the luminosity and the effective temperature, we solved Eq. (3) for $T_{\rm eff}$ by iterations. The solution obtained is a relationship between the pulsation period Π and the effective temperature $T_{\rm eff}$ for helium stars with masses of $10M_\odot \le M \le 50M_\odot$ at a given luminosity-to-mass ratio L/M. The solutions shown in Fig. 9 were obtained for $L/M = 10^4 L_\odot/M_\odot$ and $L/M = 1.5 \times 10^4 L_\odot/M_\odot$.

CONCLUSIONS

It follows from the results of our hydrodynamic calculations presented above that, for a luminosity-to-mass ratio of $L/M \gtrsim 10^4 L_\odot/M_\odot$, the instability region of radially pulsating helium stars spans a wide range of effective temperatures: $T_{\rm eff} \lesssim 10^5$ K. Despite the relatively small radial displacement, the velocity amplitude of the outer layers ΔU_N on the surface is so large that the gas flow velocity accounts for a sizeable fraction of the local escape velocity at the expansion stage. The velocity amplitude ΔU_N changes nonmonotonically with increasing effective temperature and reaches its maximum at 4×10^4 K $\lesssim T_{\rm eff} \lesssim 5 \times 10^4$ K. For $L/M = 2 \times 10^4 L_\odot/M_\odot$, the maximum velocity amplitude corresponds to an expansion velocity that is approximately half of the local escape velocity. The result of nonlinear pulsations is an increase in the mean radii of optically thin layers, causing the gas density in the outer layers of the stellar atmosphere to increase significantly.

Despite the large velocity amplitude ΔU_N, the brightness variations of radially pulsating helium stars are small, from several hundredths to approximately half a magnitude in the B band of the broadband UBV system. Such a low amplitude of the brightness variations, together with the large optical depth of the stellar wind, are probably the main reason why the pulsational variability of Wolf–Rayet stars is difficult to detect.

At a constant luminosity-to-mass ratio, the radial pulsation period is determined by the effective stellar temperature alone. The period increases with decreasing effective temperature and with increasing ratio L/M. The shortest periods of the radial modes, $\Pi \approx 6$ min, were found for $L/M = 10^4 L_\odot/M_\odot$ and $T_{\rm eff} = 9 \times 10^4$ K. Thus, along with the hypothesis of nonradial oscillations (Vreux 1985; Conti 1986; Moffat and Shara 1986; Gosset and Vreux 1987; Veen *et al.* 2003c), the instability of radial modes cannot be ruled out when explaining the pulsational variability of certain Wolf–Rayet stars.

ACKNOWLEDGMENTS

This study was supported by the Federal Science and Technology Program "Astronomy" (section 1102).

REFERENCES

1. I. Antokhin, J. Bertrand, R. Lamontagne, *et al.*, Astron. J. **109**, 817 (1995).
2. L. A. Balona, J. Egan, and F. Marang, Mon. Not. R. Astron. Soc. **240**, 103 (1989).
3. A. Blecha, G. Schaller, and A. Maeder, Nature **360**, 320 (1992).
4. P. Bratschi and A. Blecha, Astron. Astrophys. **313**, 537 (1996).
5. P. Conti, Publ. Astron. Soc. Pac. **98**, 41 (1986).
6. J. P. Cox and R. T. Giuli, *Principles of Stellar Structure* (Gordon and Breach, 1968).
7. Yu. A. Fadeyev, Astrophys. Space Sci. **213**, 75 (1994).
8. Yu. A. Fadeyev and M. F. Novikova, Pis'ma Astron. Zh. **29**, 592 (2003) [Astron. Lett. **29**, 522 (2003)].
9. A. M. van Genderen, W. J. G. Steemers, and K. A. van der Hucht, Astron. Astrophys. **185**, 131 (1987).
10. W. Glatzel and H. O. Kaltschmidt, Mon. Not. R. Astron. Soc. **337**, 743 (2002).
11. W. Glatzel, M. Kiriakidis, and K. J. Fricke, Mon. Not. R. Astron. Soc. **262**, L7 (1993).
12. W. Glatzel, M. Kiriakidis, S. Chernigovskij, and K. J. Fricke, Mon. Not. R. Astron. Soc. **303**, 116 (1999).
13. E. Gosset and J. M. Vreux, Astron. Astrophys. **178**, 153 (1987).
14. E. Gosset, J. M. Vreux, J. Manfroid, *et al.*, Mon. Not. R. Astron. Soc. **238**, 97 (1989).
15. C. A. Iglesias and F. J. Rogers, Astrophys. J. **464**, 943 (1996).
16. M. Kiriakidis, W. Glatzel, and K. J. Fricke, Mon. Not. R. Astron. Soc. **281**, 406 (1996).
17. S. V. Marchenko, J. Arias, R. Barbá, *et al.*, Astron. J. **120**, 2101 (2000).
18. T. Morel, N. St-Louis, A. F. J. Moffat, *et al.*, Astrophys. J. **498**, 413 (1998).
19. A. F. J. Moffat and M. M. Shara, Astron. J. **92**, 952 (1986).
20. F. J. Rogers, F. J. Swenson, and C. A. Iglesias, Astrophys. J. **456**, 902 (1996).
21. P. M. Veen, A. M. van Genderen, K. A. van der Hucht, *et al.*, Astron. Astrophys. **385**, 585 (2002a).
22. P. M. Veen, A. M. van Genderen, P. A. Crowther, and K. A. van der Hucht, Astron. Astrophys. **385**, 600 (2002b).
23. P. M. Veen, A. M. van Genderen, and K. A. van der Hucht, Astron. Astrophys. **385**, 619 (2002c).
24. J. M. Vreux, Publ. Astron. Soc. Pac. **97**, 274 (1985).
25. J. M. Vreux, Y. Andrillat, and E. Gosset, Astron. Astrophys. **149**, 337 (1985).

Translated by N. Samus'

Astronomy Letters, Vol. 30, No. 10, 2004, pp. 715–727. Translated from Pis'ma v Astronomicheskiĭ Zhurnal, Vol. 30, No. 10, 2004, pp. 787–800.

Synchronous Microwave Brightenings of Solar Active Regions from RATAN-600 Spectral Observations

O. A. Golubchina[1*], S. Kh. Tokhchukova[2], V. M. Bogod[1], H. A. Garcia[3], and V. I. Garaimov[1]

[1] *Special Astrophysical Observatory, St. Petersburg Branch, Russian Academy of Sciences, St. Petersburg, 196140 Russia*

[2] *Pulkovo Astronomical Observatory, Russian Academy of Sciences, Pulkovskoe shosse 65, St. Petersburg, 196140 Russia*

[3] *NOAA/Space Environment Center, Boulder, Colorado, USA*

Received January 12, 2004

Abstract—The observations of the solar radio emission on September 11, 2001, with the RATAN-600 radio telescope (southern sector) at four centimeter wavelengths (1.92, 2.24, 2.74, and 3.21 cm) revealed synchronous brightenings in solar radio sources. These were identified on the solar photosphere with active regions that were spaced up to $\sim 10^6$ km apart (AR 9608 and AR 9616). We discuss manifestations of the possible mechanisms of synchronous brightenings in solar sources in a narrow microwave spectral band. The significant linear correlation ($\rho_c = 0.84$–0.92) between the relative fluxes of AR 9610 and AR 9608 at 1.92 and 2.24 cm and the significant linear correlation ($\rho_c = 0.65$–0.84) between the relative fluxes of AR 9606 and AR 9608 at 3.21 cm in a two-hour interval of observations are indicative of the interconnection between these active regions not only during flares and bursts, but also in the periods of their absence. This confirms the existence of a large-scale temporal component in the dynamics of the radio flux variations for these active regions. We found a difference between the temporal variations of the radio emission from the halo and the solar radio sources under consideration. The times of increase in the total solar soft X-ray (0.5–4.0 Å, 1.0–8.0 Å; GOES 8, GOES 10) flux are shown to coincide with the times of increase in the fluxes from the solar radio sources at short centimeter wavelengths. © *2004 MAIK "Nauka/Interperiodica"*.

Key words: *Sun, solar flares, radio emission from solar active regions.*

INTRODUCTION

Paired flares (bursts) that emerge almost simultaneously on the Sun at sites up to $>10^6$ km apart are generally called sympathetic flares (bursts). The latter are believed to result from the impact of the primary flare on an active region far from it, i.e., sympathetic flares (bursts) are secondary ones.

Sympathetic flares and bursts have been studied with all large telescopes in the optical, radio, and X-ray ranges (see the reviews by Golubchina (2001, 2002)). Such bursts have been investigated in the radio range since the 1960s. In general, single cases of sympathetic bursts were considered in papers devoted to this issue. On the one hand, this is probably because the sensitivity of the radio telescopes was not high enough. On the other hand, the investigators seek to study the most intense events that occur not so frequently. Therefore, sympathetic flares and bursts seemed rare and exotic events. Such bursts have been investigated with the RATAN-600 radio telescope since 1980 (Golubchina 1995, 1999). The temporal resolution of the RATAN-600 is now several minutes (Tokhchukova 2002); therefore, we use the term "synchronous brightenings" instead of sympathetic bursts. This term is indicative of almost simultaneous increases in the fluxes from several solar radio sources at a certain time of observation. The brightenings of sources are deemed to be synchronous if these were recorded in a time interval of 2.0–2.5 min, i.e., the time of passage of the Sun through the antenna beam.

The high flux sensitivity of the radio telescope–radiometer system, 0.005 sfu (solar flux units), in multiazimuthal observations of the Sun allows even insignificant (down to a few fractions of a sfu) flux variations of solar sources to be reliably recorded, which is of crucial importance in investigating the synchronous brightenings.

Another important property of the RATAN-600 is that it covers a wide frequency range (18–0.95 GHz) (Bogod *et al.* 1999). The possibility of investigating the synchronous flux variations of solar radio sources at the RATAN-600 with a high sensitivity over a wide wavelength range provides a clearer insight into

*E-mail: oag@OG4466.spb.edu

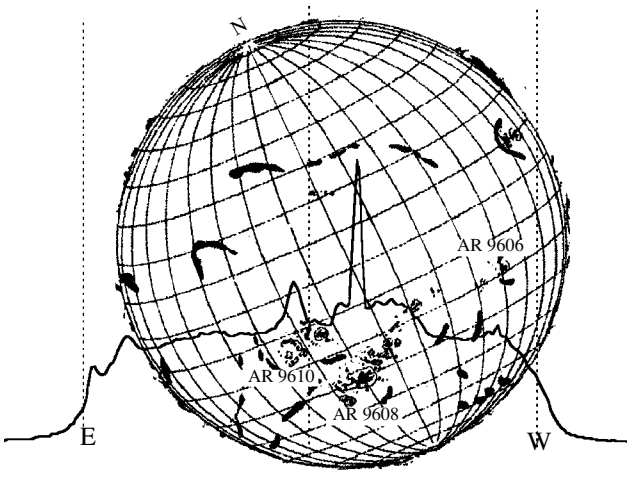

Fig. 1. Record of solar radio emission at $\lambda = 2.24$ cm (RATAN-600) and a photoheliogram of the Sun (Pulkovo Astronomical Observatory, Russian Academy of Sciences) on September 11, 2001.

the physical nature of the formation mechanism of sympathetic bursts on the basis of observational data for different levels in the solar atmosphere.

OBSERVATIONS

The observations of the solar radio emission were performed on September 11, 2001 (8:30–10:30 UT), at the southern sector of the RATAN-600 radio telescope with a periscope in multiazimuthal mode (Tokhchukova 2002) at wavelengths of 1.92, 2.24, 2.74, and 3.21 cm. The time interval between successive solar scans was 8 min. Sixteen records of solar radio emission were taken at each wavelength. The working surface of the primary mirror of the antenna was formed by sequentially pointing and diverting the groups of reflecting elements in accordance with the change in the azimuth of the center of the optical solar disk. At the same time, the secondary reflector moved along arc-shaped rails in accordance with the change in the azimuth of the observation. The antenna during the observations at the southern sector of the RATAN-600 with a periscope has a knife-edge beam. The spatial resolution of the antenna at half maximum ($\theta_{0.5}$) is: $\lambda = 1.92$ cm, $\theta_{0.5} = 17.3$ (arcsec) $\times$ 14 (arcmin); $\lambda = 2.24$ cm, $\theta_{0.5} = 21$ (arcsec) $\times$ 16 (arcmin); $\lambda = 2.74$ cm, $\theta_{0.5} = 23$ (arcsec) $\times$ 18.8 (arcmin); $\lambda = 3.21$ cm, $\theta_{0.5} = 26.7$ (arcsec) $\times$ 23 (arcmin).

The position angle of the solar observation changed only slightly during the entire two-hour observing session: $\Delta q = \pm 1^\circ$. The sensitivity of the radio telescope–radiometer system during the solar observation was $\Delta T_A \approx 1$ K in antenna temperature and $\Delta F \approx 0.005$ sfu in flux.

The solar radio sources under study were identified with the bipolar active regions AR 9610, AR 9608, AR 9606 (Fig. 1) and the rising active regions AR 9616, AR 9617 (Solar Geophysical Data, SGD) on the solar photosphere.

The Carrington longitudes of the active regions under consideration (AR 9608, AR 9610, AR 9616, AR 9617, and AR 9606) are 108°, 95°, 20.5°, 19.5°, and 153°, respectively.

The separations (L) between the active regions on the optical solar disk are L(AR 9610, AR 9608) = 1.6×10^5 km, L(AR 9606, AR 9608) = 5.5×10^5 km, L(AR 9610, AR 9616) = 9.1×10^5 km, L(AR 9616, AR 9608) = 0.7×10^6 km, L(AR 9610, AR 9606) = 7.1×10^5 km; L(AR 9606, AR 9616) = 16×10^5 km.

The dynamics of the variations in the relative radio fluxes of the listed sources was correlated, according to Solar Geophysical Data, with Hα flares in the solar chromosphere, with microwave bursts at a frequency of 9100 MHz, and with X-ray bursts as detected from GOES 8 and GOES 10 satellites in two channels: 0.5–4.0 and 1.0–8.0 Å.

PECULIARITIES OF THE OBSERVATIONAL DATA PROCESSING

We use the following notation of the physical parameters for the solar radio emission: F_0 is the radio flux from the quiet Sun; F is the absolute flux; (F/F_0) is the relative flux; T_B(K) is the brightness temperature; r is the angular size of the solar radio sources; $\delta(F/F_0)$ is the absolute measurement error of the relative flux from the source or the absolute error in the difference between the relative fluxes from the source at the time of synchronous brightenings; $\varepsilon(F)$ is the relative error in the flux from the source; $\varepsilon(F_0)$ is the relative error in the flux from the quiet Sun; ΔF and $\Delta(F/F_0)$ are the increments in the absolute and relative fluxes from the solar radio source, respectively; and n is the significance of the change in the relative flux ($n = \Delta(F/F_0)/\delta(F/F_0)$; $\Delta(F/F_0) = (F/F_0)_{N+1} - (F/F_0)_N$, N is the observation
number).

To detect synchronous increases in the radio fluxes from the sources, we analyzed the time dependence of the variations in their relative fluxes (F/F_0).

The lower envelope of the solar radio sources that was drawn over solar areas free from active structures was taken as the level of the quiet Sun (Golubchina 1999). The level and shape of the lower envelope were determined by averaging all of the records reduced to a single scale and by drawing the lower envelope of the averaged record using a spline. The

Table 1. Mean physical parameters of the sources under study observed at radio wavelengths of 1.92, 2.24, 2.74, and 3.21 cm

λ, cm	F, sfu	F/F_0, %	r, arcmin	T_B, K	F, sfu	F/F_0, %	r, arcmin	T_B, K
AR 9617					AR 9616			
1.92	1.14	0.38	0.60	4.5×10^4	1.17	0.7	1.14	2.3×10^4
2.24	–	–	–	–	2.65	0.94	1.07	4.6×10^4
2.74	1.9	0.64	0.66	1.2×10^5	3.45	1.15	1.39	5.1×10^4
3.21	2.98	1.46	0.91	1.4×10^5	3.18	1.57	1.15	10^5
AR 9610					AR 9608			
1.92	6.02	2.02	1.5	3.7×10^4	8.1	2.72	0.6	3.1×10^5
2.24	4.35	1.66	1.37	4.6×10^4	7.79	3.02	0.57	4.7×10^5
2.74	4.52	1.51	1.45	8.4×10^4	11.84	3.97	0.77	5.7×10^5
3.21	4.73	2.34	≈ 2.5	$\approx 4.5 \times 10^4$	14.65	7.15	1.08	4.9×10^5
AR 9606								
2.74	7.43	2.49	2.13	4.0×10^4				
3.21	9.82	4.85	≈ 3.86	$\approx 2.9 \times 10^4$				
AR 9608 (after halo separation)								
2.24	6.08	2.3	0.48	5.1×10^5				
3.21	9.31	4.61	0.86	4.9×10^5				

slowly varying (S) component of the solar radio emission was separated by subtracting the quiet Sun from each solar record. A software package developed at the RATAN-600 (Bogod 1999; Garaimov 1997) was used in the data processing.

The physical parameters of the solar radio sources (their absolute fluxes, angular sizes, and brightness temperatures) were calculated using a Gauss analysis by fitting the shape of the source under study by a Gaussian with appropriate parameters. Gaussians were fitted from the level of the lower envelope of the sources. If the source has a complex shape, then the data processing software allows a different method of determining the radio flux to be used. In this case, the observer specifies the boundaries of this source without fitting it by a Gaussian. This data processing method was used to investigate the dynamics of the radio emission from AR 9610 (except $\lambda = 2.24$ cm), AR 9616, and AR 9606. The calculated mean physical parameters of the sources are given in Table 1. As we see from the table, the derived fluxes are typical of medium- and low-intensity sources, while the brightness temperatures of the sources, $T_B \approx 10^4$–10^5 K, correspond to the temperature of the upper chromosphere and the lower corona.

INVESTIGATION OF THE SYNCHRONOUS BRIGHTENINGS OF SOLAR ACTIVE REGIONS AT 2.24 AND 1.92 cm

The time dependence of the relative flux from a source reflects the dynamics of the radio emission from an active region. The corresponding variations in the relative fluxes from the sources identified with AR 9610 and AR 9608 are shown in Fig. 2. The values of $\varepsilon(F)$, $\varepsilon(F_0)$, and F/F_0 were determined when the observations were processed. The absolute errors $\delta(F/F_0)$ can be calculated using the formula (Taylor 1985)

$$\delta(F/F_0) = (F/F_0)[\varepsilon^2(F) + \varepsilon^2(F_0)]^{1/2}.$$

The mean relative measurement errors of F_0 and F and the absolute measurement errors of the relative fluxes from the sources at $\lambda = 2.24$ cm are

$\varepsilon(F_0) = 1.55\%$ (as derived from 16 solar records in the entire interval of observations),

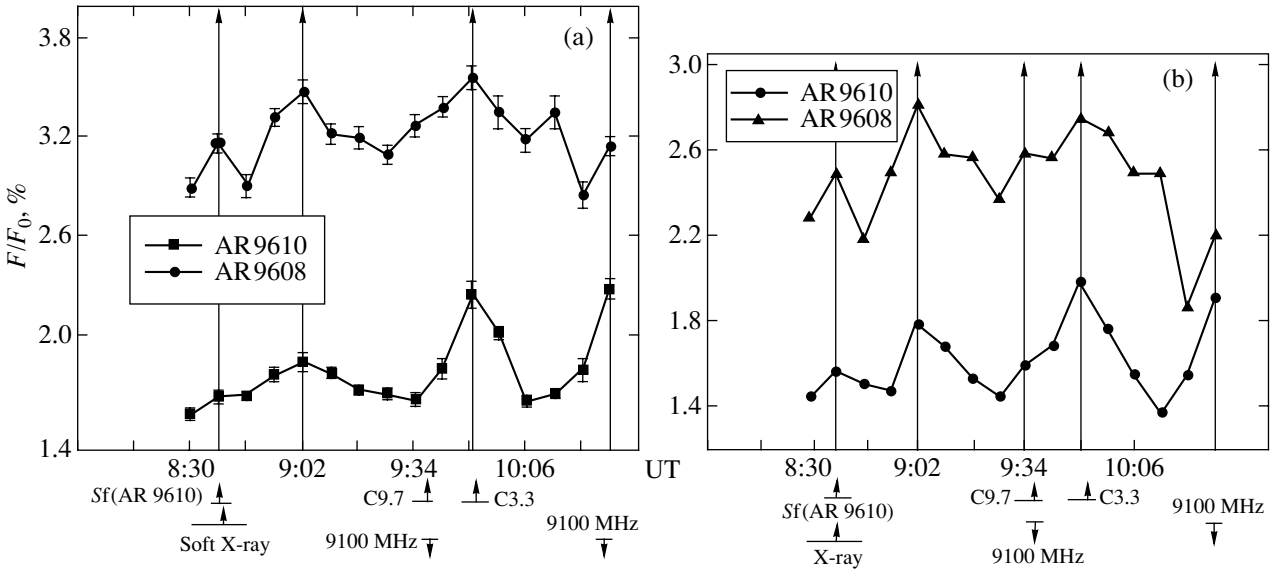

Fig. 2. Temporal variations in the relative fluxes from the sources identified with AR 9610 and AR 9608 on the solar photosphere at $\lambda = 2.24$ cm and their connection with active events observed in other wavelength ranges: (a) before and (b) after the separation of the halo of AR 9608. The following is shown below: the up arrows indicate the interval and the times of maximum of the Hα flare and flux increase in soft X rays; the down arrow indicates the same at a frequency of 9100 MHz. The vertical straight lines with arrows were drawn at the times of synchronous brightenings.

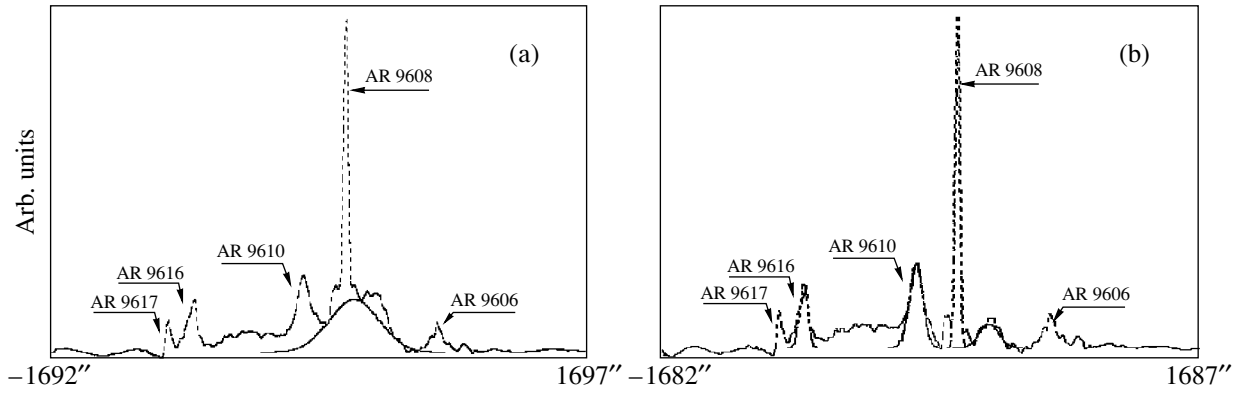

Fig. 3. (a) Halo separation from the S component at $\lambda = 2.24$ cm by Gaussian fitting; (b) Gaussian fitting of the solar radio sources after the halo separation.

$\varepsilon(F) = 1.77\%$; $\delta(F/F_0) = 0.05\%$ (as derived from the measurements of AR 9610 and AR 9608),

$\varepsilon(F) = 1\%$ (as derived from the measurements of AR 9616). The absolute error $\delta(F/F_0)$ of the relative flux (F/F_0) is given in percent, because the relative radio flux is given in percent.

Taking into account the model of a solar radio source considered by Alissandrakis *et al.* (1993), we separated the halo (an extended, moderate-intensity and low-polarization component of the local source) (Fig. 3a) under AR 9608. After halo subtraction, the source AR 9608 was identified with the largest sunspot in AR 9608 (Fig. 1). The mean angular size of the source AR 9608 is 29 arcsec. The size of this sunspot without a penumbra measured on the SGD (Hawaii) white-light solar image is 31.5 arcsec. To determine the physical parameters of the sources of the S component after the halo subtraction, we also used a Gauss analysis of the sources identified with AR 9608 and AR 9610 (Fig. 3b).

Note that the dynamics of the radio fluxes from AR 9608 and AR 9610 and their physical parameters changed only slightly (Fig. 2) after halo separation. However, at the times of synchronous brightenings 8:38, 9:02, and 9:50 UT, the increases in relative fluxes were more pronounced, while at 9:34 UT, i.e., at the time of the solar X-ray (C9.7) burst, synchronous brightenings also showed up in AR 9608

Table 2. Parameters of the solar radio sources under study at the times of synchronous brightenings at 2.24 cm

UT	F, sfu	F/F_0, %	ΔF, sfu	T_B, K	r, arcsec	$\Delta(F/F_0)$, %	$\delta(F/F_0)$, %	Significance
AR 9608 (without halo)								
08:38	6.65	2.49	0.72	4.7×10^5	31	0.20	0.06	3.3
09:02	7.42	2.49	0.88	5.7×10^5	30	0.32	0.09	3.6
09:34	6.73	2.59	0.41	6.0×10^5	27	0.22	0.09	2.4
09:50	7.08	2.74	0.24	6.1×10^5	28	0.18	0.09	2.0
10:30	5.69	2.20	0.71	5.3×10^5	27	0.33	0.10	3.3
AR 9610								
08:38	4.21	1.58	0.45	8.4×10^4	58	0.13	0.05	2.6
09:02	4.74	1.79	0.84	6.2×10^4	72	0.31	0.08	3.9
09:34	4.14	1.60	0.27	4.3×10^4	81	0.15	0.06	2.5
09:50	5.16	1.99	0.64	3.7×10^4	98	0.30	0.10	3.0
10:30	4.98	1.92	0.84	3.1×10^4	104	0.37	0.09	4.1

and AR 9610 (see Fig. 2b). Synchronous brightenings were recorded in the sources identified with AR 9610 and AR 9608 at the times the center of the optical solar disk passed through the center of the antenna beam: 8:38, 9:02, 9:34, 9:50, 10:30 UT. The quantities that characterize the increases in the relative fluxes from the sources at the times of synchronous brightenings are given in Table 2. The variations in the relative fluxes from AR 9610 and AR 9608 between the neighboring observations at the times of synchronous brightenings were recorded at a level of $\approx 3\delta(F/F_0)$. This confirms that the synchronous brightenings of AR 9610 and AR 9608 are statistically significant.

Estimates of the data processing errors confirm that the variations in the radio fluxes from the sources at the times of synchronous brightenings are real. The active processes (see Fig. 2) in soft X rays (GOES 8, GOES 10), Hα flares (SGD), and radio bursts at a frequency of 9100 MHz (SGD), which is closest to the frequencies of our observations, found in Solar Geophysical Data provide circumstantial evidence that the synchronous brightenings are real.

The derived synchronous increases in the relative fluxes from AR 9610 and AR 9608 for two neighboring observations at 2.24 cm are $\Delta(F/F_0) = 0.13$–0.37% (Table 2). This corresponds to the change in their absolute fluxes by several or several tens of percent, $\Delta F/F = 3.5$–18%, or $\Delta(F) = 0.24$–0.88 sfu in absolute flux units.

According to the Solar Geophysical Data, moderate flaring activity was observed in AR 9610 and AR 9608 (Bogod and Tokhchukova 2003). The synchronous brightenings at 08:38 UT fell within the time interval of the Hα flare (Sf) in AR 9610. The onset, maximum, and end of this flare occurred at 08:36, 08:38, and 08:43 UT (SGD), respectively. The original data reveal weak soft X-ray burst (Fig. 4a) in the interval (8:30–8:39–8:47) UT. Both sources, AR 9608 and AR 9610, were observed with the RATAN-600 near the maximum of the Hα flare in AR 9610 with the only difference that AR 9610 (08:38:01.2 UT) and AR 9608 (08:38:19.3 UT) passed through the center of the antenna beam, respectively, 1.2 and 19.3 s later than the time of maximum of the Hα flare (08:38 UT). If the onset of the brightening in AR 9608 at $\lambda = 2.24$ cm is assumed to coincide with the time of maximum of the Hα flare in AR 9610, then the velocity of the perturbing agent is $V = 10^4$ km s^{-1}. If the brightenings in these sources are associated with the onset of the Hα flare in AR 9610, then the velocity of the perturbing agent is $V = 1.6 \times 10^3$ km s^{-1}.

Let us consider another case: the onset, maximum, and end of the soft X-ray (C9.7; Figs. 2 and 4)

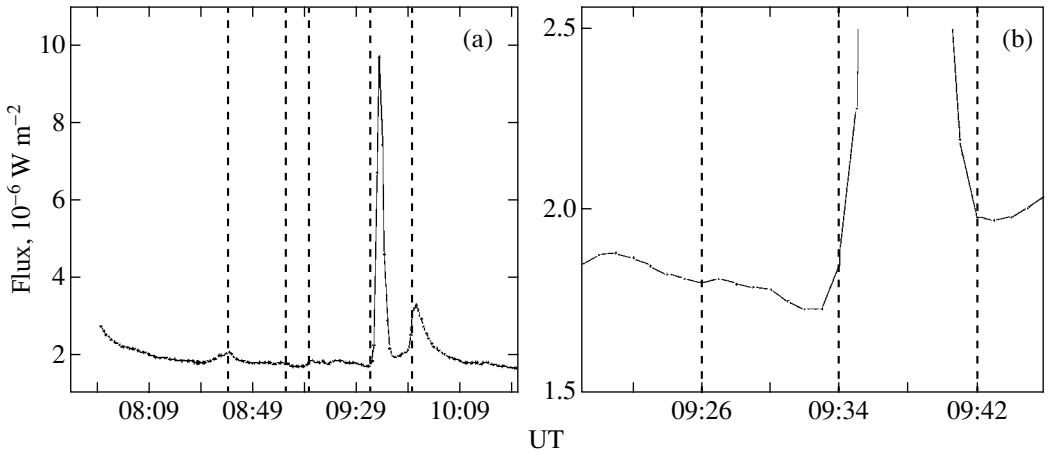

Fig. 4. Temporal variations in the total soft X-ray flux from the Sun as inferred from GOES-8 and GOES-10 data in the channel (0.5–4.0 Å): (a) in the entire interval of RATAN-600 observations; (b) in the interval 9:20–9:46 UT. The dashed lines mark the times of the brightenings recorded by RATAN-600 under discussion.

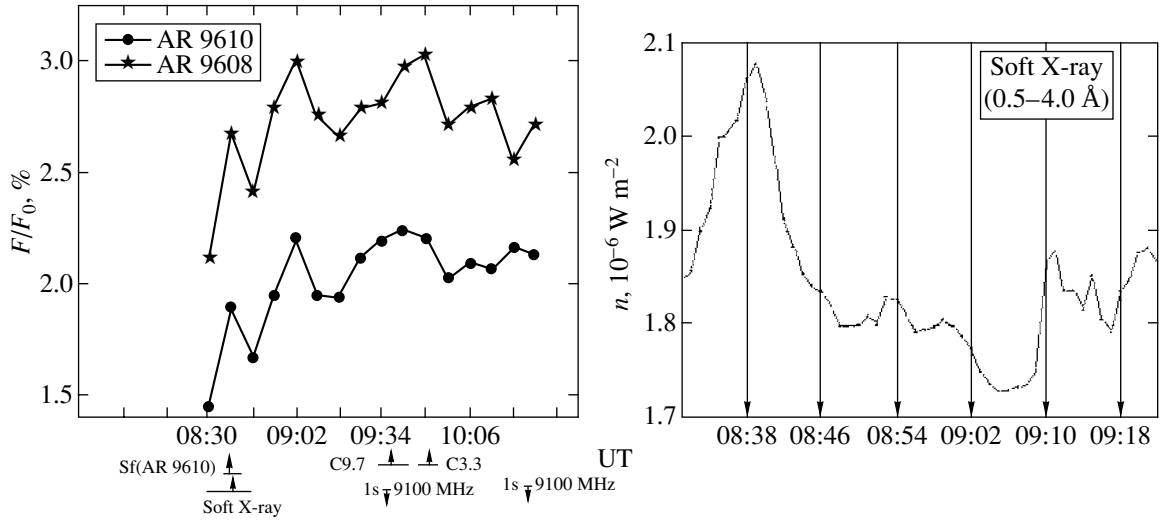

Fig. 5. (a) Temporal variations in the relative radio fluxes from the sources AR 9610 and AR 9608 at 1.92 cm; (b) a portion of the soft X-ray burst on September 11, 2001 (soft X-rays, GOES 8, GOES 10, 0.5–4.0 Å). The positions of the down arrows coincide with the times of RATAN-600 observations.

burst were recorded at 09:33, 09:37, and 09:39 UT, respectively. The RATAN-600 observations fall sequentially at 09:34 and 09:42 UT (Fig. 4b), i.e., at the onset and end of this burst, the most intense one in the period of our observations. As was noted above, the RATAN-600 revealed synchronous brightenings in the sources AR 9608 and AR 9610 at 09:34 UT (Fig. 2b).

Table 3. Mean physical parameters of the source AR 9608 and the halo at $\lambda = 3.2$ cm

Source	AR 9608 with halo	AR 9608 without halo	Halo
F, sfu	14.65	9.31	16.47
F/F_0, %	7.15	4.61	8.14
T_B, K	4.9×10^5	4.9×10^5	2.3×10^5
r, arcmin	1.08	0.86	5.34

The next time (09:50 UT) of passage of the center of the optical solar disk through the center of the RATAN-600 antenna beam falls within the time interval of the C3.3 soft X-ray burst (Fig. 2) (09:47–09:51–09:55 UT). The RATAN-600 recorded synchronous brightenings of the radio sources
AR 9610 and AR 9608 at $\lambda = 2.24$ cm at the time of observations 09:50 UT (Figs. 2a and 2b).

Table 4. Physical parameters of the solar radio sources under study at the times of synchronous brightenings at 3.21 cm

UT	F, sfu	F/F_0, %	ΔF, sfu	T_B, K	r, arcsec	$\Delta(F/F_0)$ %	$\delta(F/F_0)$ %	Significance
AR 9608 (with halo)								
08:38	15.76	7.77	0.84	4.6×10^5	69.31	0.42	0.13	3.2
AR 9608 (without halo)								
09:10	9.85	4.88	0.21	5.1×10^5	51.73	0.13	0.09	1.4
09:34	9.58	4.66	0.35	5.9×10^5	47.17	0.12	0.11	1
09:42	10.06	4.96	0.48	5.5×10^5	50.60	0.30	0.10	3
AR 9610								
08:38	4.96	2.46	0.94	–	–	0.47	0.04	11
09:10	5.67	2.81	0.79	–	–	0.41	0.08	5
09:34	4.87	2.37	0.55	4.5×10^4	≈ 122.5	0.21	0.05	4
09:50	4.89	2.42	0.38	–	–	0.18	0.06	3
AR 9606								
09:10	10.79	5.35	0.49	2.6×10^4	≈ 240.0	0.28	0.10	2.8
09:34	10.57	5.14	0.27	–	–	0.08	0.10	2.7
09:50	10.48	5.19	0.63	–	–	0.32	0.09	3.5
AR 9616								
08:38	4.50	2.23	0.52	6.8×10^4	95.79	0.26	0.04	6.5

The RATAN-600 observations at 10:30 UT fall at the end of the type-1s microwave burst at a frequency of 9100 MHz (10:27.5–10:28.3–10:29.9 UT). Synchronous brightenings were also detected in the sources AR 9608 and AR 9610 at 10:30 UT (Figs. 2a, 2b, and Table 2).

As regards the dynamics of the radio emission from AR 9616, it should be noted that there are no distinct synchronous brightenings at a 3δ level. However, as we show below, we cannot completely deny the correlation between the dynamics of the emission from AR 9616 and the dynamics of the sources AR 9608 and AR 9610 under consideration.

The dynamics of the radio emission from the sources AR 9608 and AR 9610 at 1.92 cm (Fig. 5a) is similar to that at 2.24 cm. A peculiarity of the emission from these sources at 1.92 and 2.24 cm is the synchronism of the emission at 09:02 UT (Figs. 2 and 5a). The Solar Geophysical Data reveal no events neither during the synchronous brightening that we recorded at 9:02 UT nor at the next time of observations 9:10 UT. However, a distinct increase in the soft X-ray flux was recorded in both channels at 09:10 UT (Fig. 5b).

Low-intensity synchronous brightenings $\Delta F \approx 0.24$–0.88 sfu were observed at 2.24 cm on September 11, 2001. As was noted above, such insignificant variations in the radio fluxes from the sources could be recorded with RATAN-600, because the radio telescope–radiometer system is highly sensitive in flux ($\Delta F \approx 0.005$ sfu).

SYNCHRONOUS BRIGHTENINGS OF THE SOLAR RADIO SOURCES AT 3.21 AND 2.74 cm

Using the technique described above, we also investigated the sources at $\lambda = 2.74$ and 3.21 cm. The estimated physical parameters of the sources under study are given in Tables 1 and 3.

Table 5. Mean absolute and relative measurement errors of the fluxes from the sources under study at 3.21 cm

Source	F/F_0, %	$\delta(F/F_0)$, %	$\varepsilon(F)$, %
AR 9610	2.34	0.07	2.64
AR 9608 (with halo)	7.35	0.15	1
AR 9608 (without halo)	4.61	0.08	1.45
AR 9616	1.57	0.05	2.68

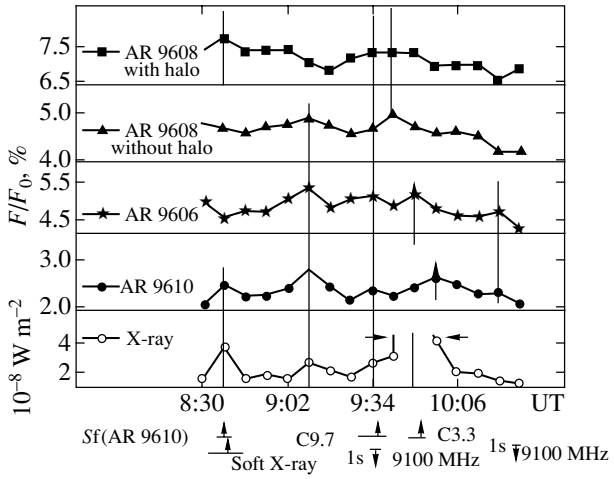

Fig. 6. Temporal variations in the relative fluxes from the sources AR 9608, AR 9610, and AR 9606 at 3.21 cm and in the intensity of the soft X-ray emission (GOES 8 and GOES 10, 0.5–4.0 Å) at the times of solar the RATAN-600 observations.

At a wavelength of 3.21 cm, we recorded several synchronous brightenings in various combinations of the sources AR 9608 (with halo), AR 9608 (without halo), AR 9610, AR 9616, and AR 9606 (Table 4, Fig. 6).

The mean relative measurement error of F_0 as determined from 16 solar records over the entire period of observations is 1%. The mean relative measurement errors of F and the absolute measurement errors of the relative fluxes (F/F_0) from the sources at $\lambda =$ 3.21 cm are given in Table 5.

Table 6. Times of onset and maximum of the increases in the relative fluxes from AR 9608 and AR 9610 recorded at 1.92, 2.24, 2.74, and 3.21 cm

Wavelength, cm	Brightening onset time, UT		Time of brightening maximum, UT	
	AR 9608	AR 9610	AR 9608	AR 9610
1.92	9:26	9:26	9:50	9:42, 9:50
2.24	9:34	9:42	9:50	9:50
2.24 (without halo)	9:34	9:34	9:34, 9:50	9:34, 9:50
2.74	9:34	9:42	9:42	9:58
3.21	9:26	9:34, 9:50	9:42	9:34, 9:58
3.21 (without halo)	9:34	9:34	9:42	9:42

The variations in the relative fluxes from the solar radio sources between neighboring observations and their significance (Table 4) confirm that the synchronous brightenings of these sources at certain times of observations at 3.21 cm are real.

As the data processing results show, the manifestation of synchronism in the brightenings of the solar radio sources at 2.74 and 3.21 cm has a more complex pattern than that at 1.92 and 2.24 cm: the synchronism in the maxima of the emission from the sources is occasionally violated, although we recorded an increase in their fluxes. Of greatest interest in demonstrating this fact is to analyze the dynamics of the radio emission from AR 9610 and AR 9608 in the interval 09:42–10:30 UT. The emission maximum for AR 9610 is delayed by about 8 min from the maximum of the soft X-ray burst ($\sim$ 09:50 UT), and, in contrast, the maximum of the radio emission from AR 9608 (without halo) is reached 8 min earlier than the maximum of the soft X-ray burst and occurs at 09:42 UT (Fig. 6).

Roughly the same situation is observed at $\lambda =$ 2.74 cm. The times of synchronous brightenings coincide with the C9.7 and C3.3 soft X-ray bursts ($\approx$ 9:34 UT, $\approx$ 9:50 UT). Unfortunately, the coordinates of these soft X-ray bursts are unknown. A comparison of the times of brightening onset or maximum at different wavelengths (Fig. 7 and Table. 6) for the sources AR 9608 и AR 9610 suggests that the primary burst occurred in AR 9608 at $\lambda \geq 3.21$ cm. Therefore, the following scenario for the interaction between AR 9608 and AR 9610 seems possible. The burst begins at about 9:26 UT in AR 9608 at $\lambda \geq$ 3.21 cm. The high-energy ($E > 10$ keV) electrons accelerated during the burst in the flaring active region AR 9608 move into AR 9610 along the magnetic loops connecting the two active regions (Fig. 8) and cause the radio flux from AR 9610 at $\lambda = 1.92$ cm to increase.

The following two mechanisms appear to be working at 2.24 cm: the action of the high-energy electrons that move along the magnetic loops connecting the two active regions and the influence of the wave fronts that also emerge at the site of the primary burst. It is probable that the action of the high-energy electrons dominates at the short wavelength of 1.92 cm. At the longer wavelengths of 2.74 and 3.21 cm, at which the dissipation of the wave fronts is weaker, the secondary brightening that was initially triggered by the action of the high-energy electrons is significantly enhanced by the wave fronts. Since the velocity of the wave fronts is lower than the velocity of the high-energy electrons, the maximum of the secondary brightenings in AR 9610 at the longer wavelengths of 2.74 and

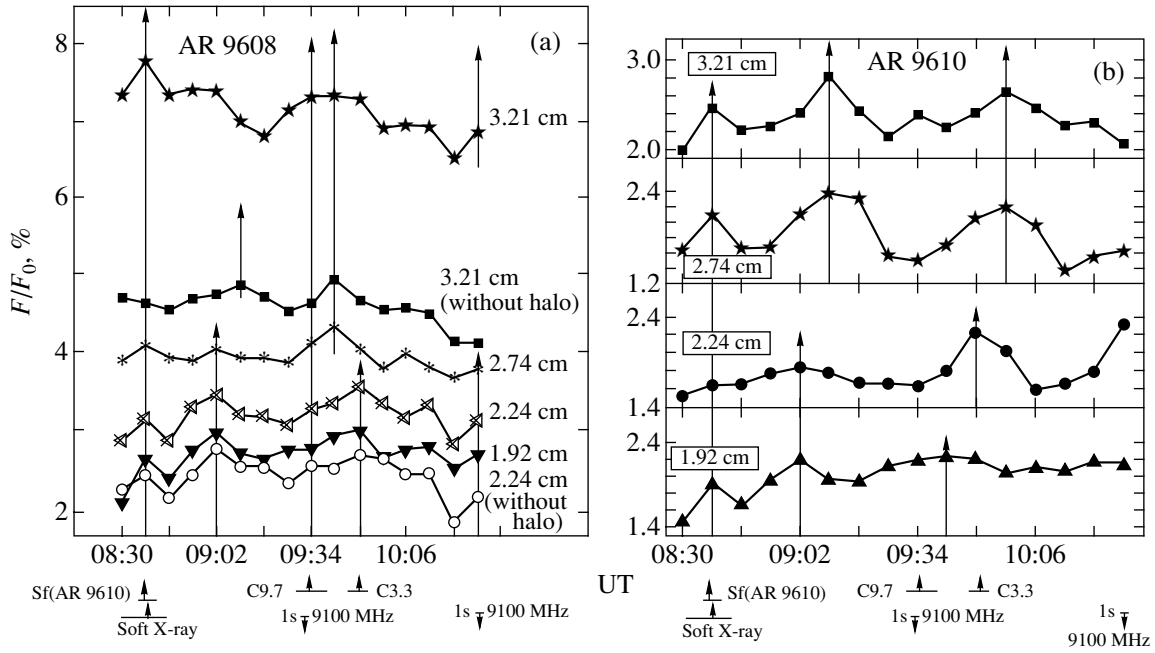

Fig. 7. (a) Temporal variations in the relative radio fluxes from AR 9608 at 1.92, 2.24, 2.74, and 3.21 cm; (b) the same for AR 9610.

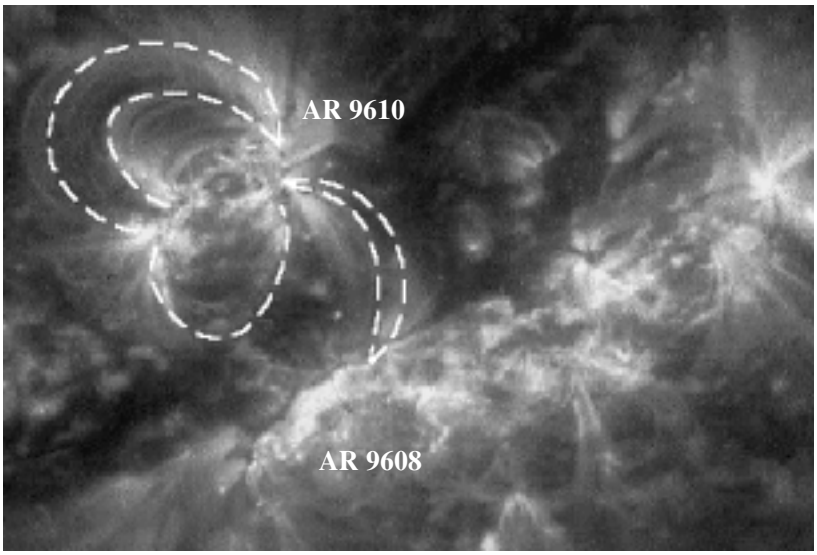

Fig. 8. Part of the image of AR 9610 and AR 9608 in the Fe IX line (September 11, 2001, SOHO).

3.21 cm occurs later than that at 1.92 cm (Fig. 7b and Table 6).

A similar shift in the maxima of the synchronous brightenings was observed from 9:02 UT ($\lambda = 1.92$, 2.24 cm) until 9:10 UT ($\lambda = 2.74$, 3.21 cm) in the sources AR 9608 (with and without halo), AR 9610, and AR 9616. Unfortunately, in this case, we cannot determine the site of the primary burst, but this shift is probably also attributable to an enhancement of the brightenings by the wave fronts that propagate after the accelerated electrons.

PECULIARITIES OF THE DYNAMICS OF THE RELATIVE RADIO FLUX FROM THE HALO OF AR 9608 AT 1.92, 2.24, 2.74, 3.21 cm

The separated halo source, the magnetosphere of the active region, (Fig. 3a) was identified with the entire extended region AR 9608, except for the

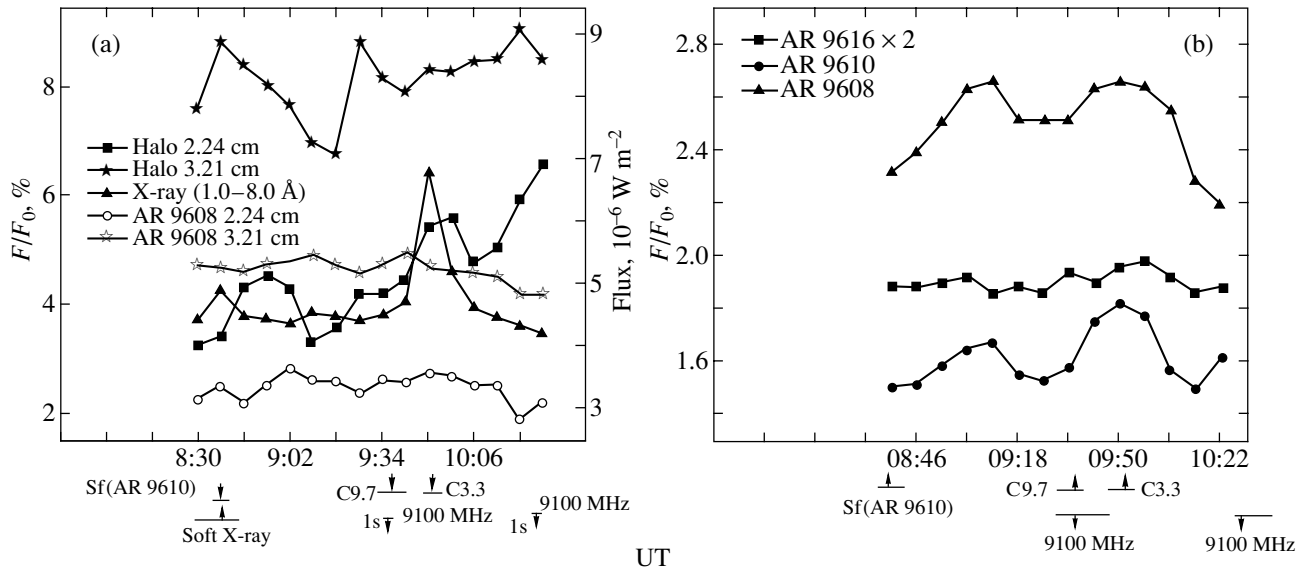

Fig. 9. (a) Temporal variations in the relative fluxes from the halo, AR 9608, and AR 9610 (after the halo separation) at 3.21 and 2.24 cm and the X-ray flux (GOES 8, GOES 10, 1.0–8.0 Å) at the times of RATAN-600 observations. (b) Temporal variations in the relative fluxes from the sources under study at $\lambda = 2.24$ cm after the smoothing by a sliding mean over three points.

main, most intense source of radio emission from this active region. In our measurements, the angular size of the halo was close to that of AR 9608 ($\approx$5.7 arcmin). The brightness temperatures in the wavelength range 1.92–3.21 cm were found to be 6.3×10^3–2.2×10^4 K. The spectrum of the halo flux is almost flat (5.4–8.2 sfu). Thus, the separated source has parameters typical of the halo.

The dynamics of the relative fluxes from the halo at 1.92 cm is similar to that at 2.24 cm, while the dynamics at 2.74 cm is similar to that at 3.21 cm. However, there is no such similarity in the halo emission at 3.21 and 2.24 cm (Fig. 9a).

During the Hα flare in AR 9610 (08:38 UT), the time of maximum of the halo emission at 2.74 and 3.21 cm coincides with the time of maximum of the synchronous brightening in the sources AR 9608 and AR 9610. For the radio and X-ray (1s, C9.7, C3.3) bursts in the interval 09:33–09:55 UT, the time of maximum of the halo emission at 2.74 and 3.21 cm leads the times of maximum of the radio emissions from AR 9608, AR 9610, and AR 9606 (Fig. 9a). The latter indicates that AR 9608 is probably the site of the primary bursts in the interval 09:33–09:55 UT. The opposite is observed at the shorter wavelengths of 1.92 and 2.24 cm, at which the maximum of the emission from the halo of AR 9608 occurs later than the synchronous brightening of AR 9608 (Figs. 7a and 9a). The delay of the maximum of the halo emission at shorter wavelengths also confirms our assumption that the process causing the brightening begins at $\lambda > 3.21$ cm.

Roughly the same situation is also observed during the next type-1s (9100 MHz) burst in the interval 10:27.5–10:28.3–10:29.5 UT. The latter indicates that AR 9608 is also the site of the primary burst at $\lambda \geq 3.21$ cm.

It should be noted that, according to our measurements, the dynamics of the halo emission (in contrast to the dynamics of the emission from the above solar radio sources) generally differs from the dynamics of the solar soft X-ray emission (Fig. 9a).

THE LARGE-SCALE TEMPORAL COMPONENT IN THE DYNAMICS OF THE RADIO FLUXES FROM THE SOURCES

To reveal the large-scale component in the dynamics of the radio emission from AR 9608, AR 9610, AR 9606, and AR 9616, we analyzed the linear correlation between their relative fluxes in the entire period of observations (8:30–10:30 UT) (Golubchina 1995). To properly reveal the large-scale (in time) variations in the radio fluxes from the sources, we performed the linear smoothing by a sliding mean over three points (Fig. 9b). The correlation coefficients calculated from N/m independent points (N is the total number of points in the series before the smoothing, and m is the number of points over which the smoothing by a sliding mean was performed) and the corresponding significance levels estimated using the statistics of small Fisher samples (Romanovskii 1998) are indicative of a significant linear correlation between the radio emissions from AR 9610 and AR 9608, AR 9616

and AR 9610, AR 9608 and AR 9616 at 2.24 cm (Table 7). The latter suggests that the active processes in these sources are interconnected in the entire period of observations at 2.24 cm. We also found a significant linear correlation between the radio emissions from AR 9610 and AR 9608 at 1.92 cm (Table 8). The interaction between the active regions not only during flares and bursts, but also in the periods of their absence confirms the existence of a large-scale temporal component in the dynamics of the radio fluxes from solar sources (Golubchina 1995, 1999).

The situation is different when analyzing the linear correlation between the large-scale temporal variations in the fluxes from the solar radio sources at 2.74 and 3.21 cm. At 2.74 cm, there is no linear correlation between the radio flux variations of AR 9608, AR 9610, and AR 9606 both before and after applying the smoothing procedure. At 3.21 cm, the linear correlation between the large-scale temporal flux variations of the solar radio sources is significant only for the sources identified with AR 9608 (without halo) and AR 9606 (Table 8).

Thus, the dynamics of the radio fluxes from the sources in a two-hour interval of observations at 2.24 and 1.92 cm differs significantly from that of the radio fluxes from the sources at 2.74 and 3.21 cm.

On the one hand, the low linear correlation between the large-scale temporal flux variations of the sources could result from the absence of appreciable interactions between the sources in intervals free from flares and bursts. On the other hand, the possible time shifts in the activity of one source relative to the other could obscure the linear correlation between the large-scale temporal variations in the radio fluxes from the sources at these wavelengths. Therefore, the detected shifts in the brightening maxima of AR 9608 and AR 9610 at 2.74 and 3.21 cm decrease the correlation coefficient between the relative fluxes from these sources.

Table 7. Correlation coefficients (ρ_0) between the relative fluxes from the solar radio sources and their significance levels (P) as calculated from the 2.24-cm observations

Coefficient	Before halo separation		After halo separation	
	ρ_0	P	ρ_0	P
ρ_{34}	0.42	0.05	0.36	0.09
ρ_{c34}	0.90	0.02	0.84	0.04
ρ_{32}	0.49	0.05	0.54	0.02
ρ_{c32}	0.93	0.01	0.97	<0.01
ρ_{c42}	0.80	0.06	0.79	0.06

Note: Here and in Table 8, ρ_0 is the calculated correlation coefficient, P is the significance of the calculated correlation coefficient, ρ and ρ_c are the correlation coefficients between the radio fluxes from the sources before and after performing the smoothing by a sliding mean, respectively; the subscripts of the correlation coefficients ρ correspond to the following AR numbers on the solar photosphere: (2) AR 9616; (3) AR 9610; (4) AR 9608; (6) AR 9606.

Table 8. Correlation coefficients (ρ_0) between the relative radio fluxes from the sources and their significance levels (P) as calculated from the observations at 1.92 and 3.21 cm before and after performing the smoothing by a sliding mean over three points

Coefficient	Before smoothing		After smoothing	
	ρ_0	P	ρ_0	P
	$\lambda = 1.92$ cm			
ρ_{34}	0.62	<0.01	0.92	0.01
	$\lambda = 3.21$ cm			
ρ_{64} (without halo)	0.65	<0.01	0.84	0.04

DISCUSSION

The recorded synchronous radio brightenings of AR 9608 and AR 9610 at wavelengths of 1.92 and 2.24 cm are indicative of a close connection between these sources, which are spaced $\sim 2 \times 10^5$ km apart. The derived correlation coefficients $\rho_c = 0.84$–0.92 at 2.24 and 1.92 cm confirm the significant linear correlation between the radio fluxes from AR 9608 and AR 9610. Thus, the reality of the interconnection between these active regions is borne out not only during flares and bursts, but also over the entire period of observations. The significant linear correlation ($\rho_c = 0.65$–0.84) between the radio flux variations of AR 9606 and AR 9608 that are spaced 3.9×10^5 km apart also suggests that these active regions are interconnected at 3.21 cm not only during flares and bursts, but also in the period of their absence.

Thus, we have found a correlation between the large-scale temporal components of the dynamics of the variations in the radio fluxes from AR 9608 and AR 9610 at 1.92 and 2.24 cm as well as from AR 9606 and AR 9608 at 3.21 cm. The results obtained are consistent with our previous conclusions (Golubchina 1995, 1999). Based on X-ray observations, Poletto *et al.* (1993) also pointed out the

mutual influence of the two active regions not only during flares, but also in the period of their absence.

Wild *et al.* (1968), Erokhin *et al.* (1974), Kundu *et al.* (1984), Nakajima *et al.* (1985), Simnett *et al.* (1989), Poletto *et al.* (1993), and Hanaoka (1997) considered the possible trigger mechanisms of sympathetic flares and bursts: corpuscular fluxes, Moreton waves, shock waves, slow shock modes, Alfvén waves, conductive fronts with thermal velocities of hot plasma, EIT (Extreme ultraviolet Imaging Telescope) waves, high-energy particles (accelerated electrons with nonthermal velocities), and a plasma echo effect. The delay between the onset of the secondary burst and the onset of the primary burst far away from it is known to be one of the criteria for choosing the mechanism of sympathetic bursts. Clearly, a high (of the order of several seconds) temporal resolution of the radio telescope is required for such estimations. We can estimate only the velocity limits for the perturbing agent that causes a secondary brightening in the local source far away from the site of primary flares or bursts.

As was said above, if the synchronous radio brightenings of AR 9608 and AR 9616 are related to the times of onset or maximum of the Hα flare (Sf) in AR 9610, then the velocities of the perturbing agent are $V = 1.6 \times 10^3$ km s^{-1} and $V \geq 10^4$ km s^{-1}, respectively. Such velocities indicate that both shock waves and high-energy electrons that are released during the flare in AR 9610 and move along the magnetic field lines connecting these active regions could be the perturbing agent.

A comparison of the times of brightening onset for the interacting regions AR 9608 and AR 9610 in the interval 9:26–9:58 UT suggests that AR 9608 is the leading group in the manifestation of active processes in this interval. In addition, the detected lead of the sharp increase in the halo flux at 2.74 and 3.21 cm relative to the same event at 1.92 and 2.24 cm indicates that in the interval ~09:26–09:58 UT, the active processes that cause the brightenings of the solar radio sources begin in AR 9608 at wavelengths of $\geq$3.21 cm.

According to the data processing results, the synchronism of the variations in the relative radio fluxes from AR 9608 and AR 9610 in the interval 09:26–09:58 UT at 2.74 and 3.21 cm is violated. This is probably because the maximum of the radio emission from AR 9610 is delayed by 7–11 min from the corresponding maximum of the emission from AR 9608 at 2.74 and 3.21 cm.

In this case, due to the low temporal resolution of the RATAN-600 (8 min), we can estimate only a lower limit for the velocity of the perturbing agent, $V = (3–7) \times 10^2$ km s^{-1}. It is probable that in the case under consideration, the wave front propagating away from the site of the primary burst in AR 9608 at 2.74 and 3.21 cm enhances the synchronous brightening of AR 9610 that previously arose under the action of the high-energy electrons that escaped during the primary burst in AR 9608 and moved into AR 9610 along the magnetic loops connecting these active regions.

The type-III and type-V bursts detected in the Solar Geophysical Data in the interval 8:59–9:38 UT indirectly confirm the action of high-energy electrons as the trigger mechanism of the secondary brightenings under consideration. In addition, the solar image in the iron (Fe IX) line clearly shows the loops that connect AR 9610 and AR 9608 at the location of the largest sunspot in AR 9608 (Fig. 8).

CONCLUSIONS

We found synchronous increases in the relative fluxes from solar radio sources that are spaced up to 10^6 km apart.

We estimated the velocity of the perturbing agent from $V = 0.3 \times 10^3$ km s^{-1} to $V \geq 10^4$ km s^{-1}. Such velocities indicate that both wave fronts and high-energy electrons released during the primary flare could be the trigger mechanism of the synchronous brightenings in solar radio sources.

Our study of the solar radio emission with the RATAN-600 at four centimeter wavelengths (1.92, 2.24, 2.74, 3.21 cm) in the interval 09:26–09:58 UT showed that the action of the high-energy electrons escaped from the site of the primary bursts and moved to the site of the secondary brightening along the magnetic loops connecting these active regions dominates as the trigger mechanism at shorter wavelengths (1.92 and 2.24 cm). At longer wavelengths (2.74 and 3.21 cm), the accelerated electrons are followed by the wave fronts whose lower velocity limit is $V = (3–7) \times 10^2$ km s^{-1}. These enhance the synchronous brightening that arose previously under the action of high-energy electrons.

Thus, our observations of the solar radio emission on September 11, 2001, with the RATAN-600 at four centimeter wavelengths (1.92, 2.24, 2.74, 3.21 cm) confirmed our previous conclusion that the synchronous brightening of solar radio sources and, hence, sympathetic flares and bursts are not exotic events (Golubchina 1999). These observations also revealed the manifestation of two different mechanisms of the synchronous brightenings of solar sources in a narrow microwave spectral range.

ACKNOWLEDGMENTS

This work was supported by the Russian Foundation for Basic Research (project nos. 02-02-16430 and 03-02-06714).

REFERENCES

1. C. E. Alissandrakis, G. B. Gelfreikh, V. N. Borovik, *et al.*, Astron. Astrophys. **270**, 509 (1993).
2. V. M. Bogod and S. Kh. Tokhchukova, Pis'ma Astron. Zh. **29**, 305 (2003) [Astron. Lett. **29**, 263 (2003)].
3. V. M. Bogod, V. I. Garaimov, N. P. Komar, and A. N. Korzhavin, *Proceedings of the 9th European Meeting on Solar Physics, Magnetic Fields, and Solar Processes, Florence, Italy, 1999* (ESA SP-448, 1999).
4. V. L. Garaimov, Preprint No. 127, SAO RAN (Spec. Astrophys. Obs., Russ. Acad. Sci., 1997).
5. O. A. Golubchina, Solar Phys. **160**, 199 (1995).
6. O. A. Golubchina, Kinemat. Fiz. Neb. Tel **15**, 59 (1999).
7. O. A. Golubchina, Tr. GAISh **71**, 16 (2001).
8. O. A. Golubchina, *Proceedings of the 11th SOHO Symposium, From Solar Min to Max: Half a Solar Cycle with SOHO, Davos, Swizerland, 2002* (ESA SP-508, 2002).
9. N. S. Erokhin, S. A. Kaplan, and S. S. Moiseev, Astron. Zh. **51**, 890 (1974) [Sov. Astron. **18**, 524 (1974)].
10. M. R. Kundu, M. E. Machado, F. T. Erskine, *et al.*, Astron. Astrophys. **132**, 241 (1984).
11. N. Nakajima, B. R. Dennis, P. Hoyng, *et al.*, Astrophys. J. **288**, 806 (1985).
12. G. Poletto, G. A. Gary, and M. E. Machado, Solar Phys. **144**, 113 (1993).
13. V. I. Romanovskiĭ, *Elementary Course on Mathematical Statistics* (Gosplanizdat, Moscow, 1939) [in Russian].
14. G. M. Simnett, Z. Mouradian, M.-J. Martres, and I. Soru-Escant, Astron. Astrophys. **224**, 267 (1989).
15. J. R. Taylor, *An Introduction to Error Analysis. The Study of Uncertainties of Physical Measurement* (Univ. Sci. Books, California, 1982; Mir, Moscow, 1985).
16. S. Kh. Tokhchukova, Preprint No. 174, SAO RAN (Spec. Astrophys. Obs., Russ. Acad. Sci., 2002).
17. J. P. Wild, K. V. Sheridan, and K. Kai, Nature **218**, 536 (1968).
18. Y. Hanaoka, Solar Phys. **173**, 319 (1997).

Translated by V. Astakhov